Big slopes, little data: data-driven nowcasting of deep-seated landslide deformation

van Natijne, A.L.

DOI
10.4233/uuid:98afe3ba-fa0d-4834-b802-60c29196ac35

Publication date
2023

Document Version
Final published version

Citation (APA)
van Natijne, A. L. (2023). *Big slopes, little data: data-driven nowcasting of deep-seated landslide deformation*. [Dissertation (TU Delft), Delft University of Technology]. https://doi.org/10.4233/uuid:98afe3ba-fa0d-4834-b802-60c29196ac35

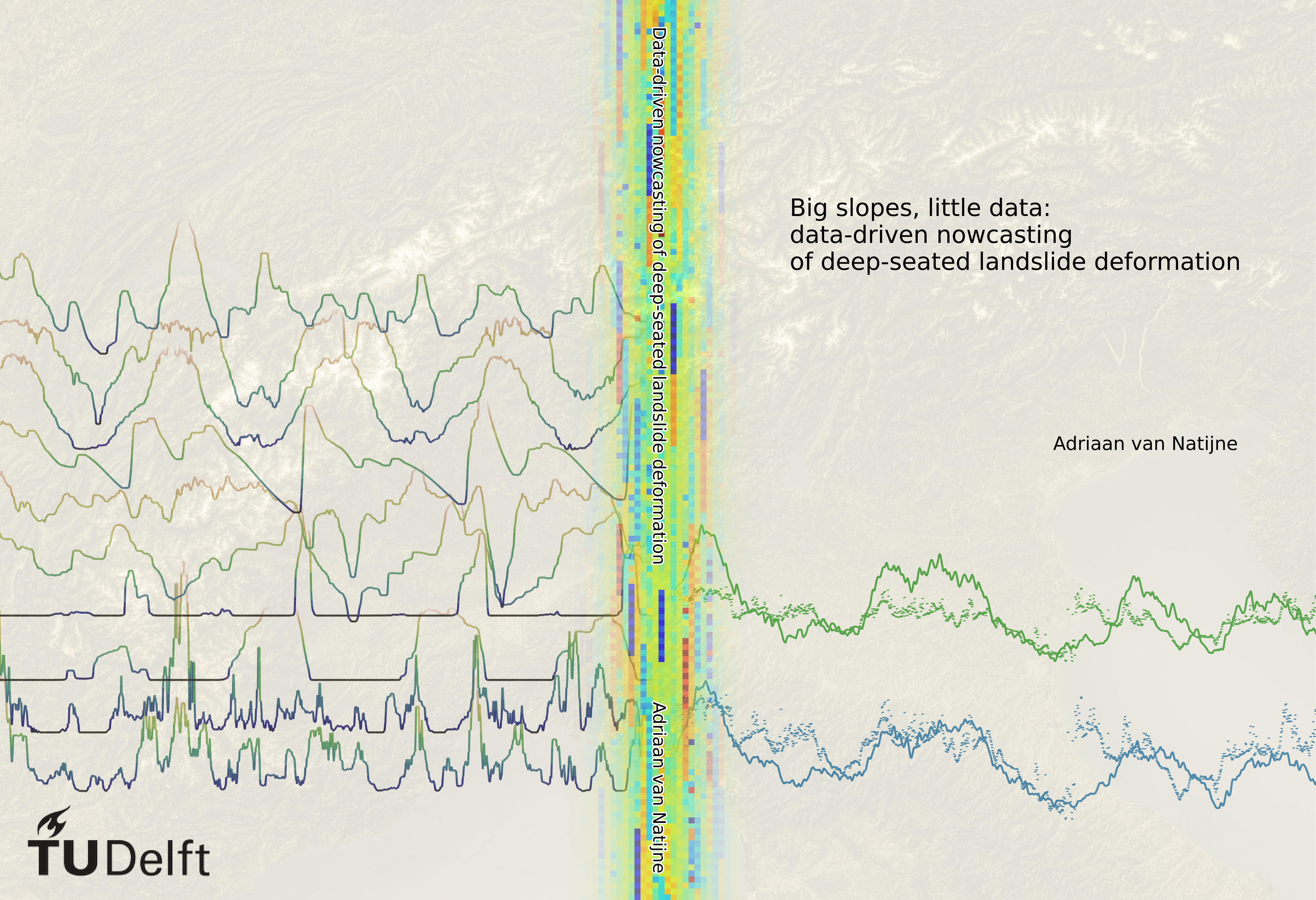

Data-driven nowcasting of deep-seated landslide deformation

Adriaan van Natijne

Big slopes, little data: data-driven nowcasting of deep-seated landslide deformation

Adriaan van Natijne

BIG SLOPES, LITTLE DATA: DATA-DRIVEN NOWCASTING OF DEEP-SEATED LANDSLIDE DEFORMATION

Dissertation

for the purpose of obtaining the degree of doctor
at Delft University of Technology
by the authority of the Rector Magnificus Prof. dr. ir. T.H.J.J. van der Hagen,
Chair of the Board for Doctorates,
to be defended publicly on Wednesday, 21 June 2023 at 15:00 o'clock

by

Adriaan Leendert VAN NATIJNE

Master of Science in Applied Earth Sciences,
Delft University of Technology, the Netherlands
born in Rotterdam, the Nederlands.

This dissertation has been approved by the promotors.

Composition of the doctoral committee:

Rector Magnificus	chairman
Dr. R.C. Lindenbergh	Delft University of Technology, promotor
Dr. T.A. Bogaard	Delft University of Technology, promotor
Independent members:	
Prof.dr.rer.nat.habil. M. Körner	Technical University of Munich, Germany
Prof.dr. N. Kerle	University of Twente
Prof.dr.ir. G.J.M. De Lannoy	KU Leuven, Belgium
Prof.dr.ir. A.W. Heemink	Technische Universiteit Delft
Prof.dr.ir. B.J.H. van de Wiel	Technische Universiteit Delft, reserve member
Other members:	
Dr. T. Zieher	Austrian Research Centre for Forests, Austria

Keywords: deep-seated landslide; machine learning; remote sensing; early warning systems; InSAR

Front & Back: Background images: EOX IT Services GmbH Cloudless Sentinel-2 mosaic, Copernicus DEM hillshade.

ISBN 978-94-6384-442-0

The doctoral research has been carried out in the context of the OPERANDUM (OPEn-air laboRAtories for Nature baseD solUtions to Manage hydro-meteo risks) project, which was funded by European Union's Horizon 2020 Framework Programme for research and innovation under grant agreement 776848.

Contents

Summary

Landslides are a major geohazard in hilly and mountainous environments. We focus on slow-moving, deep-seated landslides that are characterized by gradual, non-catastrophic deformations of millimeters to decimeters per year and cause extensive economic damage. To assess their potential impact and for the design of mitigation solutions, a detailed understanding of the slope processes is desired. Moreover, where landslide hazard mitigation is impossible, early warning systems are a valuable alternative to reduce landslide risk.

Recent studies have demonstrated the effective application of machine learning for deformation forecasting to specific cases of slow-moving, non-catastrophic, deep-seated landslides. Machine learning, combined with satellite remote sensing products offers new opportunities for both local and regional monitoring of areas with unstable slopes and associated processes without costly and logistically challenging inspection of the landslide. To test to what extent data-driven machine learning techniques and remote sensing observations can be used for landslide deformation forecasting, we developed a machine learning based nowcasting model on the multi-sensor monitored, deep-seated Vögelsberg landslide, near Innsbruck, Tyrol, Austria. Our goal was to link the landslide deformation pattern to the conditions on the slope, and to produce a four-day, short-term forecast, a nowcast, of deformation accelerations.

Changes in hillslope hydrology shift the balance between the shear strength of the soil and the shear (sliding) force applied by the gravitational forces acting on the landmass. Therefore, precipitation, snowmelt, soil moisture, evaporation, and air temperature were identified as hydro-meteorological variables with high potential for forecasting deformation dynamics. Time series of those variables were obtained from remote sensing sources where possible, and otherwise from reanalysis sources as surrogate for data that is likely to be available in the near future. Deformation, the result of slope instability, was monitored daily by a local, automated total station.

Interferometric Synthetic Aperture Radar (InSAR) has shown to be a valuable resource of deformation information from space. However, due to the complex interac-

---

An abbreviated version of this summary has previously been published as: van Natijne, A., Lindenbergh, R., and Bogaard, T. (2023). Challenges for satellite-based deep-seated landslide nowcasting. EGU General Assembly 2023, Vienna, 23–28 Apr 2023, EGU23-14398.

tion with topography in mountainous environments, its potential is often questioned. We showed that 91% of the world's slopes are observable by Sentinel-1 and that given the presence of a coherent scatterer, i.e. a natural or man-made object that exhibits consistent radar reflection over time, they could be monitored by InSAR. A global map is provided to indicate the sensitivity of InSAR to assess downslope deformation on any particular slope. To quickly assess the presence of coherent scatterers, before further investigation, we developed an application in Google Earth Engine to estimate the presence and location of coherent scatterers on a slope. However, the current accuracy and temporal resolution of Sentinel-1 SAR acquisitions proved insufficient to identify the acceleration phases at Vögelsberg.

The five years of daily deformation and hydro-meteorological observations at the Vögelsberg landslide is quite limited for a machine learning model. Therefore, a nowcasting model of low complexity was required. To limit the number of parameters to be optimized, the model was designed to mimic a bucket model, a simple hydrological model. A shallow neural network based on long short-term memory, was implemented in TensorFlow, as custom sequence of existing building blocks. Furthermore, a traditional neural network and recurrent neural network were tested for comparison. Thanks to the limited complexity of the model, the major contributors could be determined by trial-and-error of nearly 150 000 model variations.

Models including soil moisture information are more likely to generate high quality nowcasts, followed by models based solely on precipitation or snowmelt. Although none of the shallow neural network configurations produced a convincing nowcast deformation, they provide important context for future attempts. The machine learning model was poorly constrained as only five years of observations were available in combination with the four acceleration events that occurred in these five years. Furthermore, standard error metrics, like mean squared error, are unsuitable for model optimization for landslide nowcasting.

We showed that landslide deformation nowcasting is not a straightforward application of machine learning. The complexity of the machine learning model formulation at the Vögelsberg illustrates the necessity of expert judgement in the design and evaluation of a data-driven nowcast of slowly deforming slopes. Furthermore, to prepare for unexpected modelling developments, a high level of project level data organisation is recommended. There is a long road ahead for the large scale implementation of machine learning in landslide nowcasting and Early Warning Systems. However, a future, successful nowcasting system will require a simple, robust model and frequent, high quality and event-rich data to train upon.

Samenvatting

Aardverschuivingen vormen een niet te verwaarlozen gevaar in heuvel- en bergachtig gebied. Dit proefschrift richt zich op langzame, diepe aardverschuivingen die worden gekenmerkt door continue, niet catastrofale deformatie van de helling met snelheden van millimeters tot decimeters per jaar. Dit type aardverschuiving is wereldwijd verantwoordelijk voor grote economische schade. Risico-inschatting en mitigatiemaatregelen vereisen gedegen kennis van de processen die aan de hellinginstabiliteit ten grondslag liggen. Voor hellingen waar mitigatiemaatregelen onmogelijk zijn, is een waarschuwingssysteem op basis van voorspelling van het deformatiegedrag een alternatief.

Recent lieten verschillende studies casestudy's de toepassing zien van zelflerende algoritmen voor deformatievoorspellingen op langzame, reactiverende aardverschuivingen. Een combinatie van satelliet-aardobservaties en zelflerende algoritmen zou het mogelijk maken om grootschalig, zonder tijdrovend en kostbaar veldwerk, deformatievoorspellingen voor reactiverende aardverschuivingen te doen. Om de mogelijkheden voor een dergelijk systeem te onderzoeken ontwikkelden wij een zelflerend computermodel voor de Vögelsberg aardverschuiving nabij Innsbruck, Oostenrijk. Het doel van deze studie was deformatie voor de volgende vier dagen te voorspellen.

Veranderingen in de waterbalans van een helling beïnvloeden de balans tussen de schuifsterkte en de zwaartekracht. De aan de waterbalans gerelateerde variabelen neerslag, smeltwater, bodemvocht en verdamping zijn belangrijke indicatoren zijn voor veranderingen in de deformatiesnelheid van een aardverschuiving. Voor dit onderzoek gebruikten wij waar mogelijk tijdreeksen van de omstandigheden op de helling, verkregen met satellietaardobservatie. Zover geen satellietobservaties beschikbaar waren, is gebruikgemaakt van andere bronnen om zulke observaties te simuleren. Een tachymeter aan de overzijde van de vallei mat dagelijks de deformatie van Vögelsberg, het resultaat van hellinginstabiliteit.

Satelliet-radar-interferometrie (InSAR) is een beproefde bron van satelliet deformatiemetingen. Vanwege de complexe interactie met de topografie in bergachtig terrein is het succes van een InSAR deformatieanalyse vooraf moeilijk in te schatten. Voor

---

Een verkorte versie van deze samenvatting is eerder gepubliceerd als: van Natijne, A., Lindenbergh, R., and Bogaard, T. (2023). Challenges for satellite-based deep-seated landslide nowcasting. EGU General Assembly 2023, Vienna, 23–28 Apr 2023, EGU23-14398.

elke helling op aarde berekenden wij de sensitiviteit van de InSAR techniek voor aardverschuivingsdeformatie. Hiermee toonden wij aan dat op 91% van de hellingen wereldwijd topografie niet de belemmerende factor zal zijn voor InSAR deformatiemetingen. Voor succesvolle toepassing van InSAR zijn natuurlijke of kunstmatige objecten nodig met een duurzame, coherente radar reflectie. Een op Google Earth Engine gebaseerde applicatie helpt gebruikers zulke objecten vooraf te identificeren. De nauwkeurigheid en opnamefrequentie van de Sentinel-1 radar satellieten bleken onvoldoende om de bewegingen van Vögelsberg te analyseren.

Van Vögelsberg is een vijf jarige tijdreeks van deformatiemetingen en omgevingscondities beschikbaar. Voor zelflerende modellen is dit een korte referentietijdreeks. Daarom is een eenvoudig model met een beperkt aantal parameters nodig. Wij kozen voor een model dat sterke gelijkenissen vertoont met een eenvoudige waterbalans. Het ondiepe neurale netwerk model van long short-term memory neuronen functioneert als een empirische waterbalans en is opgebouwd uit standaardelementen van de TensorFlow programmabibliotheek. Ter vergelijking zijn ook een traditioneel neuraal netwerk en een recurrent neuraal netwerk getest. 150 000 model variaties leidden proefondervindelijk tot de belangrijkste modelparameters.

Modellen die gebruikmaakten van bodemvocht voorspelden de deformatiesnelheid het best, gevolgd door modellen uitsluitend gebaseerd op neerslag of smeltwater. Hoewel geen van de modellen een overtuigende voorspelling van de deformatiesnelheid produceerde, vormen zij toch een belangrijke basis voor toekomstige studies naar voorspelling van het gedrag van aardverschuivingen op basis van zelflerende algoritmen. De beschikbaarheid van een tijdreeks van slechts vijf jaar aan observaties waarin de aardverschuiving vier maal versnelde, blijkt onvoldoende voor een zelflerend model. Daarnaast is de veelgebruikte kwadratische gemiddelde fout (mean squared error) van het modelresultaat ongeschikt voor het beoordelen van voorspellingen van deformatiesnelheid.

Deze studie toont aan dat het voorspellen van de deformatiesnelheid van aardverschuivingen met zelflerende algoritmen niet eenvoudig is. Hydrologische expertise bleek onmisbaar bij het opstellen van het model voor Vögelsberg en bij de beoordeling van de kwaliteit van het model. Daarnaast verdient het de aanbeveling te investeren in opslag en toegankelijkheid van de voor een dergelijk model vereiste gegevens. Er is nog een weg te gaan voor zelflerende modellen van aardverschuivingen een bijdrage zullen kunnen leveren aan de ontwikkeling van deformatiewaarschuwingssystemen. Een succesvol systeem bestaat uit een robuust, eenvoudig model en is gebaseerd op uitgebreide, rijke, en accurate tijdreeksen van historisch deformatiegedrag en omstandigheden van de betreffende aardverschuiving.

Chapter 1

Introduction

Landslides are a major geohazard in hilly and mountainous environments. To the broader public, landslides are best known for their videos of large, catastrophic collapsing slopes, that make it into news broadcasts multiple times per year. Not as well known as their collapsing counterparts, are slow-moving, deep-seated landslides, which are expected to make up for 50% of all landslides globally (Herrera et al., 2018; Novellino et al., 2021), and are abundant in the European Alps (Crosta et al., 2013). Deep-seated landslides are typically not deadly, but their continuous, slow deformation causes extensive, costly damage to settlements and infrastructure on the slope (Mansour et al., 2011).

A slope may be susceptible to instability, due to pre-disposing factors such as unfavourable lithology. Landslide hazard is triggered by non-standard conditions that cause instability, such as prolonged or extreme precipitation. The people or assets vulnerable to the hazard, are at risk. Interference with either the hazard or vulnerability, will mitigate the landslide risk. Hazard mitigation is accomplished by various structures, intended to reduce susceptibility, divert the triggering factors, or protection of the elements at risk due to the landslide process. Traditionally these structures were built using local materials, over time many of these structures have been replaced by ‘gray’, concrete solutions.

1.1 OPERANDUM project

Recently, renewed attention has been given to so-called Nature-Based Solutions (NBS): working with nature, instead of against, to mitigate natural hazards (Nesshöver et al., 2017). The OPERANDUM project, that this work was part of, aims to provide a “solid basis for the formulation, implementation and monitoring of NBS related EU policies” regarding various hydro-meteorological hazards, including landslides (OPERANDUM, 2017).

Figure 1.1: Overview of the Vögelsberg landslide from the automated total station (Figure 1.2), located in Wattenberg, opposite to Vögelsberg. (October 2018)

The OPERANDUM project covers aspects of NBS across the relevant disciplines necessary for successful deployment of NBS, from socio-economic impact to engineering (Anderson et al., 2022). To implement any solution, gray or green, a thorough understanding of the hazard is necessary for an effective application. To assess the effectiveness of the solution, monitoring is required before and after implementation. Furthermore, to simplify future applications, it is required to advance our understanding of the system and to design efficient monitoring solutions.

Within the OPERANDUM project there are ten Open Air Laboratories (OALs) covering different hydro-meteorological hazards. There are two OALs concerning landslides: Catterline Bay, near Aberdeen, United Kingdom and the Vögelsberg landslide, near Innsbruck, Austria. These sites had already been closely monitored before the start of the project in 2018. During the project an NBS was designed and implemented at each of the OALs.

This thesis notably focuses on the Vögelsberg deep-seated landslide (Figure 1.1), located in the Wattens basin, near Innsbruck, Austria. Parallel to our work, the Austrian Academy of Sciences (ÖAW) analysed the hydrology and deformation behaviour of the Vögelsberg landslide in the field. They planned and implemented an NBS experiment, and provided us with local knowledge of Vögelsberg and its surroundings.

The active part of the landslide is only about $0.2\,\mathrm{km}^2$ and is covered by pasture fields, sparse forests and few houses and farm buildings. In 2016 an Automated Total Station (ATS) for slope displacement monitoring was installed in Wattenberg,

Figure 1.2: Left: the automated total station for geodetic monitoring and its protective housing in Wattenberg, opposite to Vögelsberg (see Figure 1.1), with the author for scale. Right: campaign based laser scanning of the deformation at the Vögelsberg landslide. A technique also applied elsewhere by the Austrian team (Pfeiffer et al., 2018, 2019). Not shown are the unmanned aerial laser scanning campaigns (Zieher et al., 2019). (Images courtesy of Roderik Lindenbergh, October 2018.)

Figure 1.3: Landslide deformation rate at one of the benchmarks, as observed by the automated total station.

Figure 1.4: Damage to a house (left) and infrastructure (right) in Vögelsberg due to slope movement. (left: image courtesy of Thomas Zieher, right: image by the author, October 2018)

opposite to Vögelsberg (Figure 1.2), that surveyed a total of fifty-three benchmarks in and around Vögelsberg every hour. The total station measured displacement rates up to 10 cm/year during periods of accelerated deformation, with continuous, gradual deformation, of around 3 cm/year the rest of the time (Figure 1.3). The deformation causes extensive damage to the houses and infrastructure on the slope, as shown in Figure 1.4.

Studies on the hydrology and geomechanical processes were conducted by Pfeiffer et al. (2021, 2022). The deformation of the Vögelsberg landslide is a complex response to the hydro-meteorological conditions in the catchment, in particular precipitation and (delayed) infiltration from snowmelt. A nearby weather station reports an average yearly precipitation of 896 mm, of which 13% is in the form of snow. The shear zone, i.e. the transition between stable and deforming soil, was identified via inclinometer measurements to be at 43–51 m below the surface, although strongly disintegrated soil up to 52–70 m deep indicates a long history of activity (Pfeiffer et al., 2021). A delay of 20–60 days between rainfall and landslide acceleration and a 0–8 day time lag between snowmelt and acceleration was found by Pfeiffer et al. (2021).

1.2 Landslide early warning systems

Using susceptibility analysis, experts have successfully identified areas prone to landslide hazard (Chacón et al., 2006; Reichenbach et al., 2018). However, most work is dedicated to catastrophic, shallow landslides triggered by excessive rainfall or seismic activity. Furthermore, to assess the hazard and potential of mitigation solutions, details on the type and frequency of the trigger should be included. Monitoring is the key to such understanding and enables us to assess the interaction between the landslide and its surroundings.

Where landslide hazard mitigation is impossible, monitoring and early warning systems are a valuable alternative to reduce landslide risk. An early warning system leaves the underlying hazard unchanged (OPERANDUM, 2017), but reduces the landslide risk by increased awareness. Regional landslide early warning systems are commonly based on binary precipitation thresholds, and are mainly applicable to shallow landslides. In contrast, local early warning systems, are typically based on extrapolation of ongoing deformation measured by in-situ sensors to trigger a warning for a single slope (Intrieri et al., 2019). Current regional and local early warning systems do not provide the information required for the planning of mitigation measures.

The effective application of an early warning system, however, carries implicit understanding of the factors of influence to slope instability. Therefore, the implementation of an early warning system is a first step towards mitigation measures. Planning of mitigation solutions requires a detailed model, that links the conditions on the slope to the deformation pattern. Such systems are often difficult to implement at regional scale or in remote areas due to dependency on fieldwork as well as local sensors.

Traditional, physics based landslide models require laborious fieldwork, local monitoring and case study specific modelling work. These manual methods are case study specific, and are limited by availability of experts. Recent advances in data integration (i.e., machine-learning), have shown success in predicting a variety of processes from underlying conditions. Furthermore, satellite remote sensing may provide information on the conditions at the slope, without local presence.

Various, recent, studies have demonstrated the effective application of machine learning for deformation forecasting of slow-moving, non-catastrophic, deep-seated landslides. Early warning systems based on short-term forecasting, also known as nowcasting, estimate the deformation pattern from the conditions on the slope. Therefore, we believe a combination of these techniques may be used to link conditions on the slope to the deformation of a deep-seated landslide, as illustrated in Figure 1.5.

Our goal is to demonstrate this link between conditions on the slope and the deformation pattern, by short-term forecasting the deformation multiple days ahead of time. The continuous deformation of a deep-seated landslide may be used in a cycle of prediction, monitoring and optimisation of a machine learning based model. The well monitored Vögelsberg landslide enables us to test various model configurations based on combinations of local, remote sensing and modelled data sources. The landslide specific knowledge present within the project enables us to explore a range of models from completely ‘naive’ to ‘physics inspired’.

1.3 Research objective

Recent developments, both in satellite remote sensing and machine learning, have opened up possibilities for detailed landslide nowcasting: linking the conditions on the slope to landslide deformation. Therefore, the objective of this project is:

To create a system for nowcasting of
landslide deformation at Vögelsberg
based on readily available remote sensing data
using machine learning techniques.

The **nowcasting system** will continuously estimate the current state of the system and associated **deformation** rate in the near future. The system is based on **machine learning** with none or limited physical modelling of the landslide process. The dynamics of the system are inferred from the deformation observations and the system is trained and validated on the progressive, gradual deformation of the landslide. **Readily available data** from satellite remote sensing sources will be used. The **Vögelsberg** landslide will be the primary testing location for the implementation of the nowcasting technique.

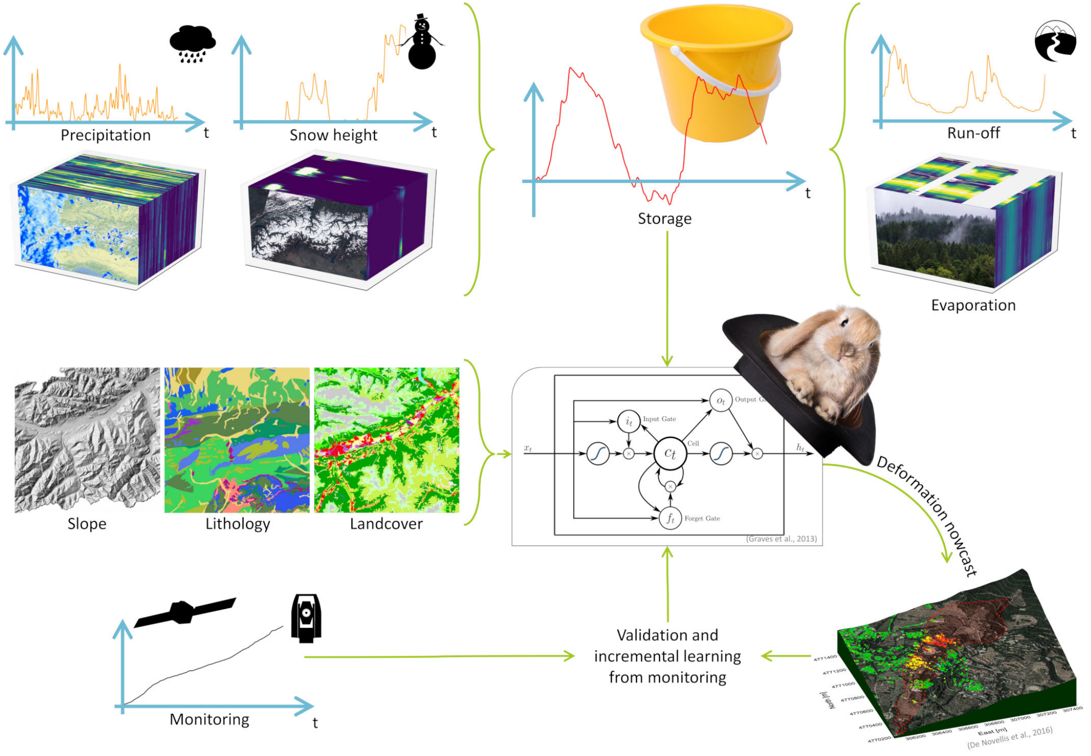

Figure 1.5: Sketch of the modelling concept. From top to bottom: the hydro-meteorological conditions on the slope; the pre-disposing factors and model; and the deformation predictions and observations. The hydro-meteorological conditions, shown on the top, as point observations and gridded data products, may be combined into a storage model or directly fed to the machine learning model. A magicians hat (center), the machine learning algorithm, integrates the various data sources to a deformation nowcast. The nowcast is validated against the measured deformation.

1.4 Research questions

The goal forms both an engineering and scientific challenge. Data integration of long, high-resolution time series is a 'big-data' engineering-challenge, while the scientific challenge is in the nowcasting algorithm design. This leads to the main research question:

To what extent can
data-driven machine learning techniques
be used for landslide deformation nowcasting
at deep-seated landslides?

Guiding in the process will be the following sub-questions:

1. **What are the requirements for a deep-seated landslide deformation nowcasting system?**

   Deep-seated landslides, unlike shallow landslides, typically exhibit continuous deformation, with intermittent accelerations that rarely lead to collapse. Therefore, their monitoring requirements are different from those for shallow landslides. Furthermore, accelerated deformation is expected to be a delayed rather than immediate response to hydro-meteorological conditions.

   Landslide deformation nowcasting carries the potential for the integration into a landslide early warning system. Depending on the intended use and target audience, different requirements may apply to the deformation nowcasting system. What are the necessities for an operational system, of which the design could extend to an early warning system?

2. **What data and model(s) may drive such a nowcasting system?**

   Monitoring systems, based on the interpretation of current and recent deformation (e.g. Carlà et al., 2017), may only be used to detect already ongoing acceleration. To predict acceleration in advance, acceleration should be predicted from the conditions of the slope. However, the deformation behaviour of slow, deep-seated landslides is considered extremely difficult to model (Van Asch et al., 2007).

   Machine learning techniques are known be able to unravel the complexities of natural processes. Neural networks, for example, are universal approximators (Hornik et al., 1989), i.e. they may be used to approximate any signal from another, related signal. This broad category of models offers many model variations to link conditions on the slope to deformation.

   A major challenge is to map the high frequency changes in the hydro-meteorological conditions to the slow acceleration/stabilisation due to the inertia of the slope. To minimize the model's complexity, we explore methods with some resemblance to the hydrological processes within the landslide.

   - What conditions influence the landslide deformation, and are they observable from the surface?

  - What are the properties of the models used in the state-of-the-art?

3. **What satellite based landslide deformation observations are available?**

   Deformation is the primary indicator of mass movement, and the quantity to be predicted. Therefore, deformation measurements are necessary for the training and validation of the model. Local, in-situ monitoring systems have proven to be effective to model a variety of (local) deformation patterns. However, such measurements are sparse, costly and can only be acquired after installation of the measurement device. Satellite deformation measurements could provide an alternative to in-situ observations with their regional coverage.

4. **What remote sensing data sources are available?**

   Satellite observations provide global, repeat observations of the conditions and triggers of accelerated deformation. What data is available or anticipated, and with what quality and frequency? In the last decades satellite observations have increased in quantity, shortening the time between subsequent acquisitions, as well as increasing the number of variables observed (Belward and Skøien, 2015). Therefore, satellite observations carry the potential to power universal landslide deformation nowcasting systems.

5. **How to implement a machine learning based deep-seated landslide model?**

   The final model should be computationally efficient enough to allow for many model configurations to be tested. This is an implicit limit on the complexity of the model, although many performance optimizations are provided by popular machine learning software toolboxes. To verify the effectiveness of the nowcast, the performance of the resulting nowcast should be quantified, and a performance metric has to be chosen. This metric may also be used to quantify the performance of the model in the absence or presence of specific observations.

   - How to quantify the quality of the nowcasting solution?
   - How to quantify the relative importance of the data sources to the result of the nowcasting system?
   - What are the major contributing variables to a landslide deformation nowcast?
   - How many observations/events are necessary to develop the nowcasting system?

6. **What do the insights obtained at the Vögelsberg tell us on the general applicability of machine learning based landslide deformation nowcasting models?**

   Although well monitored, the Vögelsberg landslide is a complex system, and therefore not a straightforward test case. What is the ideal slope to further develop a machine learning based nowcasting method, working from the challenges faced during application at Vögelsberg? Deformation nowcasting will be a necessity for regional or even continental landslide monitoring and early warning systems. What are the necessities for scaling the methodology to a regional solution? Finally, what new possibilities will the continued development of the (satellite) data products offer?

1.5 Scope and limitations

Our algorithm design and experiments are focused on deformation nowcasting at the Vögelsberg landslide. The work by Pfeiffer et al. (2021, 2022) provided guidance in particularities of this specific landslide. However, where possible, we have attempted to extend our conclusions and recommendations to deep-seated landslide nowcasting of other slopes. No physics based modelling is applied, although the machine learning algorithms show resemblance to well-known modelling methods.

The triggering factors considered in this research are limited to hydro-meteorological conditions and will be broader applicable. Where possible remote sensing data sources were used, next to existing monitoring infrastructure in the field (i.e. an automated total station) and re-analysis data sets. The remote sensing data acquisition is out of scope, and available data products are treated 'as-is' with little modification. Their acquisition, processing and data dissemination strategy are not part of this research.

For research purposes an operational setting is simulated, and re-live data integration is considered to be equal to nowcasting. This retrospective approach enabled us to assess the system performance in the absence of operational remote sensing products.

Seismic activity, that may trigger instability, is not considered.

1.6 Outline

This introduction briefly described the motivation, background and objective of this research. The questions outlined in §1.4 find their answers in Chapters 2, and 3 and iterate towards a machine learning based nowcasting system for deep-seated landslides for the Vögelsberg deep-seated landslide, as covered in Chapter 4.

Chapter 2 elaborates on the basic system design shown in Figure 1.5. It provides a literature review on the state-of-the-art, and promising machine learning techniques for landslide deformation nowcasting. Furthermore, it provides a comprehensive overview of available remote sensing sources.

Chapter 3 focuses on Interferometric Synthetic Aperture Radar (InSAR), that has the potential to provide frequent, (near) global deformation estimates. However, mountainous topography is known to complicate acquisition and extraction of deformation time series. The method developed and presented in Chapter 3 provides a worldwide a-priori estimate on the sensitivity of InSAR deformation estimates to downslope deformation. Furthermore, we explore the possibility to a-priori estimate the availability of InSAR deformation time series.

Chapter 4 describes the landslide deformation nowcasting models developed for the Vögelsberg landslide. The selected machine learning models are tested for their performance as deformation nowcasting system, and the best model settings are identified by extensive testing. Moreover, this chapter contains recommendations for the future implementation of similar models.

Chapter 5 combines the lessons learned and road ahead for data-driven modelling of landslides and slope processes as a whole. Special attention is paid to the challenges regarding data ingestion and processing, challenges that are shared by many projects around remote sensing data.

Chapter 6 provides concluding remarks and recommendations for future studies into landslide deformation nowcasting systems.

An integrated bibliography of all chapters is provided at the end of this thesis.

Chapter 2

Machine learning: new potential for deep-seated landslide nowcasting

Published previously as: van Natijne, A. L., Lindenbergh, R. C., Bogaard, T. A., 2020. Machine Learning: new potential for local and regional deep-seated landslide nowcasting. *Sensors*, 20(5), 1425. `https://doi.org/10.3390/s20051425`.

Abstract

Nowcasting and early warning systems for landslide hazards have been implemented mostly at the slope or catchment scale. These systems are often difficult to implement at regional scale or in remote areas. Machine Learning and satellite remote sensing products offer new opportunities for both local and regional monitoring of deep-seated landslide deformation and associated processes. Here, we list the key variables of the landslide process and the associated satellite remote sensing products, as well as the available machine learning algorithms and their current use in the field. Furthermore, we discuss both the challenges for the integration in an early warning system, and the risks and opportunities arising from the limited physical constraints in machine learning. This review shows that data products and algorithms are available, and that the technology is ready to be tested for regional applications.

2.1 Introduction

Landslides are a major hazard to human life and society, killing over 55,000 people over the period of 2004–2016 (Froude and Petley, 2018), and causing an estimated average economic loss of €4.7 billion per year in Europe alone (Haque et al., 2016). To protect the public, landslides have been a major research topic for the last few decades, strengthened by recent commitments such as the Sendai agreement for disaster risk reduction and the 'Kyoto 2020 commitment' to reduce landslide disaster risk (International Consortium on Landslides, 2019; Sassa, 2019).

New data and data integration methods offer new possibilities for landslide forecasting, especially for slow-moving, deep-seated landslides. Here, we provide a perspective on the possibilities, applications, and challenges of both local and regional deformation nowcasting and its inclusion in early warning systems. A nowcast describes the current, estimated system state, and provides an outlook on the coming days.

We focus on slow moving, deep-seated landslides on natural slopes, for which deformation is controlled by hydro-meteorological conditions. These landslides are characterized by gradual, non-catastrophic deformations of millimeters to decimeters per year and can be monitored and modeled over at least multiple years. They are considered to be in a state of so-called limit-equilibrium undergoing continuous deformation, but may accelerate or stabilize when conditions change (Intrieri et al., 2018).

Landslide geologists have compiled local, spatial landslide susceptibility maps since the 1970s (Brabb et al., 1972; Dobrovolny, 1971; Radbruch and Crowther, 1970). Such maps delineate landslide-prone areas based on historic landslides and expert analysis of landscape properties. However, susceptibility maps only indicate where a landslide may occur without a specific time frame (Fell et al., 2008). Advances in geospatial data acquisition and processing in the last 50 years have greatly influenced the field. Current, quantitative, regional (Wilde et al., 2018; Günther et al., 2014) and global (Stanley and Kirschbaum, 2017; Nadim et al., 2006) susceptibility maps are based on statistics rather than expert judgement alone and use historical landslide events for calibration/training.

Extensive reviews have been written on the state-of-the-art in susceptibility mapping, either summarising the methods available or making quantitative analyses of the classification process (Intrieri et al., 2019; Reichenbach et al., 2018; Chae et al., 2017; Budimir et al., 2015; Kanungo et al., 2009; Delacourt et al., 2007; Chacón et al., 2006; Brenning, 2005; Huabin et al., 2005). However, whereas static susceptibility maps have proven their value for spatial planning, when monitoring landslide stability, both for single landslides as well as on a regional scale, time dependency cannot be neglected (van Westen et al., 2008).

In practice, most shallow landslides are triggered by extreme precipitation events (Kirschbaum et al., 2015), or by a combination of hydro-meteorological events. However, failure modes for fast-moving landslides are not applicable to deep-seated landslides and statistical relationships —for example, the intensity-duration thresholds for precipitation do not offer sufficient predictive power (Bogaard and Greco, 2018). Although seismic events can not be neglected as a trigger, earthquakes are a different triggering mechanism that is explicitly not considered here. Moreover, earthquakes with a magnitude lower than 4.0–5.5 are less likely to trigger a landslide (Rodríguez et al., 1999; Keefer, 1984).

Sliding behaviour is governed by the balance of forces within the landslide, that is, the relation of the shear strength of the soil to the shear (sliding) force applied by the gravitational forces acting on the landmass. Changes in hydrology change the balance between these forces (Bogaard and Greco, 2015). Therefore, infiltration of rain, or delayed infiltration from snow melt, and the subsequent rise of the pore water pressure shift the balance of forces as the increased pore pressure weakens the soil.

As a major result of the landslide process, displacement is a key parameter to capture the interaction between landslide deformation and hydro-meteorological conditions—the relation between soil moisture and increased deformation has been observed in the field (Benoit et al., 2015; Tofani et al., 2013a). Studies focused on the progressive deformation of individual landslides have appeared in recent years, connecting deformation to the conditions on the slope (e.g., Du et al., 2013, Table 4). These studies claim good results in predicting landslide deformation based on hydro-meteorological conditions using machine learning algorithms and limited geomechanical modelling.

Machine learning offers new possibilities to bypass the microscale physics of the landslide, estimating the behaviour based on large data sets of previous responses to hydro-meteorological conditions as an intermediate step between passive monitoring and extensive (numerical) modelling of the landslide. This is done either by incorporating physics, such as the groundwater level, in the statistical model (Wei et al., 2019; Krkač et al., 2017) or by estimating the deformation rate of the landslide directly based on the hydro-meteorological time series. Although there is no strict link between data availability and predictive capacity (Corominas et al., 2013), such an approach has been proven to work at the landslide scale, such as by the examples discussed in Section 2.3.

At the advent of both local and regional landslide nowcasting, data availability is more important than ever, especially data that can be used for training of new machine learning algorithms. Their spatial properties and significance in the landslide process, as well as their temporal availability and suitability for automated data integration should be taken into account.

In this paper, we highlight the opportunities of machine learning using static and dynamic remotely sensed data sources for monitoring and nowcasting of deep-seated landslides. The overarching aim is to arrive at a near real-time, machine learning-based, local and regional early warning system for precipitation-initiated acceleration of slowly deforming slopes. Hereto, we will discuss conditional data sources, and dynamic causal and triggering factors. Then, we will discuss various machine learning algorithms from landslide literature. The paper finally discusses the current limitations and challenges, as well as the potential of combining local near real-time ground sensed data with the remotely sensed data.

Table 2.1: Key variables in the landslide process that can be acquired from satellite observations.

Variable	**Role**	
Slope	Pre-disposing	Static
Geology	Pre-disposing	Static
Soil moisture	Causal	Dynamic
Precipitation	Trigger	Dynamic
Snow (melt)	Trigger	Dynamic
Land use	Causal	Dynamic
Deformation	Result	Dynamic

2.2 Monitoring opportunities for slow-moving deep-seated landslides

Landslides are "the movement of a mass of rock, debris, or earth (soil) down a slope" (Cruden, 1991; Fell et al., 2008). Pre-disposing factors are essential for a landslide to form and have been integrated in susceptibility maps in the past. However, the landscape is stable most of the time. Leading up to a landslide are causal and triggering factors—these first allow the landslide to happen, making it sensitive to triggering factors that initiate the movement.

The deformation of the landslide is an indicator of stress at the sliding plane, which is often impossible to measure directly. For landslides in limit-equilibrium, the balance of forces can be approximated by the Mohr–Coulomb failure criterion (Terzaghi, 1943) under the assumption of a single sliding plane. Moreover, past landslide events are indicative of future behaviour, and similar landslides will exert similar behaviour in similar situations (Fell et al., 2008; Guzzetti et al., 1999). Furthermore, the behaviour of continuous, slow-moving, non-catastrophic landslides can be followed over longer periods of time (Intrieri et al., 2019).

Working from the various reviews of susceptibility maps (Reichenbach et al., 2018; Budimir et al., 2015), a list of key variables that can be acquired from satellite observations is shown in Table 2.1. Slope, and related properties of aspect and curvature, are typically identified as primary conditioning factors for landslides: no slope, no landslide. In most susceptibility analyses, dynamic triggering factors like precipitation or snow melt are not included, but should be included in a landslide nowcasting solution. Toe erosion—either gradual by water or sudden by building activity—is often captured in land use. However, local situations may require extra variables to be added, such as reservoir water level (Li et al., 2018), or ground temperature for freeze–thaw effects.

The systematic, often global, availability of satellite remote sensing data sources is a valuable addition to local (field) surveys and monitoring, where data availability is dependent on commissioning by local authorities. Furthermore, it allows for measurements in harsh environments that are not easily accessible. Here, we list potential information sources for each variable identified in Table 2.1.

2.2.1 Regional topography

As gravity is the driving force behind any landslide, a slope is a requirement for landslide deformation. Local slope, aspect, and curvature are derived from globally available satellite digital elevation models, such as SRTM (Farr et al., 2007); ALOS (Japan Aerospace Exploration Agency, Earth Observation Research Center, 2019; Tadono et al., 2014); TanDEM-X DEM (Rizzoli et al., 2017) or ASTER-GDEM (Tachikawa et al., 2011). Typically, the resolution of such products is 30–90 meters. Regional products, mostly acquired from airborne platforms, often have a resolution of 0.5–10 meters. A coarse resolution may hide small terrain features and will typically attenuate slope estimates (Grohmann, 2015; Erskine et al., 2007; Zhou and Liu, 2004), where on the contrary, a coarse elevation discretization may introduce false, sharp gradients (Thompson et al., 2001).

The best elevation model for landslide characterisation is not necessarily the most accurate in the traditional sense. Errors in referenced specification documents are often listed as absolute errors, while the local error, relative to the direct vicinity, is much more relevant for the calculation of derivatives, such as slope. The quality of elevation models is debated in literature, often by intercomparison of different products (Grohmann, 2018; Nascetti et al., 2017; Frey and Paul, 2012; Hirt et al., 2010; Hayakawa et al., 2008; Bolch et al., 2005) or comparison to a different measurement, such as GPS (Suwandana et al., 2012) or levelling (Hirt et al., 2010). Slopes, which are dominant in mountainous terrains, particularly have an effect on the accuracy of the elevation model (Szabó et al., 2015). Although acquisition dates vary, if topography is assumed to be stable, different sources can be combined. For example, MERIT (Yamazaki et al., 2017), NASADEM (Crippen et al., 2016), EarthEnv-DEM90 (Robinson et al., 2014), and VFP (de Ferranti, 2014) elevation models are fusion products, combining data from multiple elevation data products.

2.2.2 Regional geology and lithology

In the context of deep-seated landslide nowcasting, the geology can be considered static. However, not all lithologic types are equally susceptible to landslides. The OneGeology project serves as an integrator between various local maps and provides interfaces for public use to access these maps at a global scale. Global maps, such as the FAO-UNESCO “Digital Soil Map of the World” (Sanchez et al., 2009) or “ISLSCP II Global Gridded Soil Characteristics” (Scholes et al., 2011), or dedicated maps, such as the lithological layer of the “International Hydrogeological Map of Europe” (IHME) (Duscher et al., 2015), provide information on the uppermost water-bearing layer and matches the hydrological focus of landslide research. Resolutions are up to 100 m, which therefore covers mainly large-scale geologic features.

2.2.3 Hydro-meteorology

Complete reviews of satellite precipitation data sets were given by Satgé et al. (2020) and Beck et al. (2017, 2019), each reviewing over 20 precipitation data sets of which half publish data within days. Both reviews conclude the best-performing data product is MSWEP, followed by IMERG. In the context of landslide nowcasting, only products with short availability are interesting: the product has to be available hours, or at maximum, a few days after the measurement, and should be open for integration. Products reported to have these properties are listed in Table 2.2. The average spatial resolution is approximately 12 km.

Antecedent water content, soil saturation, and pore pressure play key roles in landslide instability (Bogaard and Greco, 2018, 2015; van Asch et al., 1999), and local soil moisture content can be a precursor of landslide instability (Thomas et al., 2019; Mirus et al., 2018). Even though soil moisture measurements from space are still limited in resolution and depth, satellite soil moisture information may help constrain the nowcast (Marino et al., 2020).

A bucket or tank model can be used to estimate the ground water level from indirect measurements, such as precipitation, transpiration estimates, and run-off measurements (Nie et al., 2017; Ponziani et al., 2012; Godt et al., 2006; Glade, 2000). Run-off of small streams cannot be measured by satellites, and requires in situ or close-range measurements, while the other parameters can be estimated (Novák, 2012). This approximation is never perfect, but allows for an indirect estimate of groundwater from surface processes. The groundwater level is then used to estimate the pore pressure, which is related to the stability of the landslide (Nie et al., 2017; Malet et al., 2005). Furthermore, it filters the high-frequency precipitation signal to low-frequency changes in groundwater.

2.2.4 Land use

Land use has an influence on the infiltration of precipitation and the evapotranspiration loss of water, and therefore, is of influence to the hydrological cycle. Furthermore, artificial slopes are an alteration of the natural balance and are more susceptible to landslides (Le and Kawagoe, 2018). Therefore, a combination of vegetation and topographic maps is required to assess the influence on the hydrological cycle.

OpenStreetMap provides a global coverage of the human presence in a unified way in large parts of the world on the scale of individual roads (Barrington-Leigh and Millard-Ball, 2017). The large-scale CORINE Land Cover (CLC) map provides information on both anthropogenic settlements as well as crude vegetation information at 100 m resolution (Bossard et al., 2000). The JAXA ALOS forest map (Shimada et al., 2014), as well as the 'Global Forest Change' product by Hansen et al. (2013) focuses on forest cover only. Even larger-scale information on unmapped human settlements can be obtained from satellite observations of night light (Elvidge et al., 1999, 1997).

Unfortunately, land use information extracted from maps is limited by the update

Table 2.2: Overview of precipitation data products. Adapted from Satgé et al. (2020) and Beck et al. (2017, 2019), showing only data sources with at least Near Real Time (NRT) coverage. A spatial resolution of 0.1° is approximately equal to 11 × 11 km at the equator, or 8 × 11 km at 45° N/S (e.g., Alps). Lag is the relative age of the latest available product.

Name	**Spatial Resolution**	**Coverage**	**Temporal Resolution**	**Coverage**	**Lag**	**Note**
CMORPH v1.0	0.07°	<60°	30 min	1998-NRT	1 day	
GDAS	∼0.25°	global	3 hourly	2015-NRT	6 days	
GSMaP-MVK	0.1°	<60°	hourly	2000-NRT	3 days	
GSMaP-NRT	0.1°	<60°	hourly	2008-NRT	4 h	
GSMaP-NOW	0.1°	<60°	30 min	2019-NRT	30 min	
GSMaP-RNC	0.1°	<60°	hourly	NRT only	−6 h	
IMERG v5/6	0.1°	<60°	30 min	2014-NRT	4 h	
MSWEP v2.2	0.1°	global	3 hourly	1979-NRT		Request only
PERSIANN	0.25°	<60°	hourly	2000-NRT	2 days	
PERSIANN-CCS	0.04°	<60°	hourly	2003-NRT	1 h	
TMPA 3B42RT v7	0.25°	<50°	3 hourly	2000-NRT	8 h	Obsolete
CPC Unified	0.5°	land	daily	1979-NRT	2 days	
ERA5T	0.25°	global	hourly	1979-NRT	5 days	

frequency. CORINE, for example, is updated every six years. Information extracted directly from satellite imagery is less prone to such delay, and enables the detection of land use changes and associated changes in the water balance. Satellite imagery can be used directly to monitor for extreme changes, such as forest fires or building activity, on a more frequent basis.

2.2.5 Displacement

Sources of deformation measurements are numerous, but often local. Inclinometers, total station measurements, and GNSS surveys provide on-site information on the progressive deformation of the landslide. The aforementioned solutions require access to the landslide to mount the sensors or benchmarks. Alternative solutions include ground-based InSAR (GB-InSAR) (Zhou et al., 2019; Corsini et al., 2006; Leva et al., 2003) and LiDAR surveys (Prokop and Panholzer, 2009; Huang et al., 2019; Zieher et al., 2019, reviewed by Jaboyedoff et al. (2012)), that require no access to the landslide itself, but can be operated from anywhere with direct visibility on the landslide. Therefore, the system can be used as emergency intervention too (Antonello et al., 2004). However, especially continuous surveys require installation on-site. Measurements can only begin after installation, after sliding behaviour has been detected. Campaign-based measurements provide a limited temporal resolution, but may be operated without a fixed set-up on site (Zieher et al., 2019).

Satellites are the ideal means for regional repeat surveys without access to the landslide or its vicinity. The importance of satellite-based Interferometric Synthetic Aperature Radar (InSAR) for both local and regional landslide deformation assessments is widely recognized (Colesanti and Wasowski, 2006; Hilley et al., 2004), and Intrieri et al. (2018) claim: “if InSAR monitoring had been active over this region, an early warning of imminent failure could have been given”. Especially for slow-moving landslides, the accurate tracking of ‘persistent scatterers’ (PS-InSAR), and often buildings or rock faces, provides opportunities for long-term deformation monitoring. Furthermore, the power of retrospective studies on previously acquired data is a big advantage over local monitoring solutions. However, constant features, such as clear rock faces or buildings should be present on the landslide. Moreover, the direction of sliding should not be parallel to the direction of flight of the satellite, typically north–south. Deformation in this direction will not be visible in the line of sight of the radar sensor, perpendicular to the direction of flight. Nevertheless, even with limited presence of such features, a combination with campaign-based surveys will still densify the deformation time-series (Carlà et al., 2019b; Schlögel et al., 2017; Ciampalini et al., 2016).

2.3 Machine learning and data assimilation

The integration methods discussed here combine different quantities from different measurements into a single, different quantity: the deformation rate. A clear distinction can be made between either physical or statistical algorithms and qual-

Table 2.3: The methods of landslide susceptibility or hazard assessment discussed, and their properties in time and type of analysis. (Map icon derived from Wilde et al. (2018).)

Method	**Time Dependency**	**Outcome**	
Susceptibility mapping	None, static	Qualitative	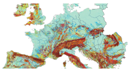
Hazard nowcasting	Dynamic	Qualitative	🔴🟡🟢
Deformation nowcasting	Dynamic	Quantitative	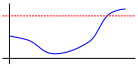

itative or quantitative assessments. Physical modelling relies on expert knowledge of the processes in the landslide and is built on the evaluation of predefined sets of rules (Kanungo et al., 2009). Statistical methods are based on the assumption that landslides are more likely to occur in circumstances that led to landslides earlier (Guzzetti et al., 1999).

The assessment is either qualitative—such as low, moderate, or high hazard—or a quantitative output, such as deformation rate. The different assessment methods have been highlighted and illustrated in Table 2.3. The desired output for our approach is a deformation rate nowcast, estimated based on conditioning and triggering factors, as mentioned in Table 2.1. However, the existing, successful implementation of qualitative hazard nowcasting is a starting point for quantitative analysis. From there, we explore the possibilities of various quantitative algorithms with increasing computational complexity.

2.3.1 Hazard nowcasting

Kirschbaum and Stanley (2018) set an example for large-scale hazard nowcasting, and showed that simple rules can provide a qualitative landslide hazard nowcast. Their nowcast has global coverage and is updated every 30 minutes at a kilometer resolution based on satellite data. Their approach is to estimate susceptibility first, signaling a landslide hazard when thresholds on antecedent precipitation are exceeded in areas of high susceptibility. A similar method is used by Posner and Georgakakos (2016), based on soil moisture instead of precipitation. These systems do not estimate the system state, and there is no nowcasting of deformation, as they are a nowcast of susceptibility instead.

Landslide hazard nowcasting and early warning systems are typically trained and tested on inventories of the time and place of historic, catastrophic landslides. These landslide inventories are often event inventories, listing collapse events rather than landslides experiencing continuous and slow deformation. Examples of inventories are the ‘Global Landslide Catalog’ (Kirschbaum et al., 2010), ‘ELS-DAT’ (Haque et al., 2016), and the ‘Global Fatal Landslide Database’ (Froude and Petley, 2018; Petley et al., 2005). A system focused on continuous deformation patterns cannot be trained on the events in such inventories. Although shallow landslides are the primary focus of most large-scale inventories, some local inventories of deep-seated landslides exist (Riedmann et al., 2014; Damen et al., 2014), or can be deduced from deformation patterns (Rosi et al., 2018; Cascini et al., 2013; Righini et al., 2012). Local inventories are still valuable to selectively activate nowcasting systems in areas with active landslides. While historic information could provide insight in the conditions leading up to the event, a catastrophic event will change the dynamics of the slope and previous dynamics may no longer be valid (Guzzetti et al., 1999).

2.3.2 Deformation nowcasting

A more complex approach is to estimate the system state, including the deformation rate, either by geomechanical modelling or based on statistics of historical deformation. This last approach of estimating the system state will be the focus of the methods mentioned here. Typically, solutions strive for the simplest model with the smallest possible error in the prediction of cumulative deformation or deformation rate. While more complex models are more likely to fit the data, they introduce the risk of overfitting the model to the data, thereby reducing the predictive power.

After model selection, as discussed in the following subsections, the process is typically subdivided into three steps: data preprocessing; training or optimisation, and application. During preprocessing, all variables are brought to the same reference frame. Furthermore, preprocessing of the input variables can be used to enhance the information content of the input, such as by dissecting the signal into various sub-signals first (Lian et al., 2013). The training or optimisation phase is a computationally intensive phase, where the model parameters are optimised such that the model approaches the deformation process best. Many combinations of model and preprocessing and training methods are possible, and final selection may require multiple models to be tested (Miao et al., 2018). Finally, during application, the tuned model is run over incoming data to predict the deformation of the landslide.

Intrieri et al. (2019) reviewed a large number of data integration methods, and concluded that no ‘best’ model could be identified due to the lack of comparable case studies between models. The Baishuihe landslide, at the shores of the Three Georges Reservoir, China, offers some possibilities for comparison, as multiple methods have been tested on this landslide by various authors (see Table 2.4). However, the influence of the reservoir water level on the landslide stability, not commonly present elsewhere, cannot be neglected and conclusions are therefore not easily transferable to other landslides.

Direct relation precipitation–deformation

Traditional models, summarised by Bernardie et al. (2015), rely on a direct relation between precipitation and deformation. Various models exist for this relation,

Table 2.4: Examples of different integration methods, linking hydro-meteorological conditions to deformation time series, and associated case studies. Where applicable, the reference methods used in the paper are listed in brackets. Relevant abbreviations are expanded in the text.

	Case Study	**Observed Driving Forces**	**Deform. meas.**	**Method (Reference Methods)**
Xie et al. (2019)	Laowuji, China	Rainfall, toe excavation	Total Station	LSTM
Bossi and Marcato (2019)	Passo della Morte, Italy	Rainfall, groundwater	Inclinometer	Linear regression
Yang et al. (2019)	Baishuihe & Bazimen, China	Rainfall, reservoir level	GNSS	LSTM
Miao et al. (2018)	Baishuihe, China	Rainfall, reservoir level	GNSS, inclinometer	GA-SVR, GS-SVR, PSO-SVR
Li et al. (2018)	Baishuihe, China	Rainfall, reservoir level	GNSS	LASSO-ELM, Copula (ELM, SVM, RF, kNN)
Logar et al. (2017)	Ventor, United Kingdom	Rainfall	Crackmeter	ANN
Krkač et al. (2017)	Kostanjek, Croatia	Groundwater (change), season	GNSS	RF
Zhou et al. (2016)	Bazimen, China	Rainfall, reservoir level	GNSS	PSO-SVM (GA-SVM, GS-SVM, BPNN)
Cao et al. (2016)	Baijiabao, China	Rainfall, groundwater, reservoir level	GNSS	ELM (SVM)
Lian et al. (2015)	Baishuihe & Bazimen, China	Rainfall, reservoir level	GNSS	LSSVM, ELM, combination
Chen and Zeng (2013)	Baishuihe, China	None	GNSS	BPNN
Du et al. (2013)	Baishuihe & Bazimen, China	Rainfall, reservoir level	GNSS, inclinometer	BPNN
Lian et al. (2013)	Buishuihe, China	None	GNSS	EEMD-ELM, M-EEMD-ELM (ANN, BPNN, RBFNN, SVR, ELM)
Corominas et al. (2005)	Vallcebre, Spain	Groundwater	Extensometers	Physics
Neaupane and Achet (2004)	Okharpauwa, Nepal	Rainfall, groundwater	Autoextensometer	BPNN

where the parameters such as time lag are determined by optimisation on historical records. However, separate modelling of the hydro-meteorological conditions is required, as only effective precipitation can be used in the model. Support Vector Regression (SVR) is a data-driven equivalent of a direct relation, while Bossi and Marcato (2019) found a direct relation with river discharge. However, a model with a direct relation between precipitation and displacement does not account for changing soil conditions and associated infiltration dynamics.

Division of the variable space

Models such as Support Vector Machines (SVM), either with linear or non-linear models, subdivide the variable space in different combinations of conditioning factors. To find the optimal parameters for the model, an optimisation method is applied, such as Particle Swarm Optimization (PSO), Grid Search (GS) or Genetic Algorithm (GA), all applied by Miao et al. (2018). All optimisation parameters strive to use the change in output of each consecutive model state to further reduce the errors in the least possible iterations. Decision trees and Random Forest (RF) classifiers provide a similar (non-linear) subdivision of the input variables. All these models are insensitive to time series, although additional copies of input variables with a time lag may be added.

With slow-moving landslides, the deformation signal is small. Therefore, the absolute error of any deformation rate nowcast is likely to be small as well, and consequently difficult to compare to deformation rates modelled using physically-based models. Furthermore, when training (optimising) such models on a regional scale, there is a risk of introducing a bias towards the abundant stable, non-landslide cases. Thus, one has to provide both a balanced training sample, as well as an error metric (loss function) suitable for such small differences.

Artificial neural networks

Powerful alternatives are Neural Networks and related technologies, which are not applied to classify the deformation behaviour, but to transform the input variables to a deformation estimate using a non-linear transformation. Such systems can be made aware of time and the spatial relationship between neighbouring areas and are capable of detecting relations unnoticed by experts. In addition, such systems may estimate other variables in the process, such as a groundwater change (Krkač et al., 2017).

As the optimisation is based on statistics only, most machine learning algorithms are ‘unaware’ of the relations between system variables in space and time and are therefore unable to accurately asses the prediction error (Jia et al., 2018). Additional rules may be implemented in the training processes, to validate the solution against physics or other rules. An example is the solution proposed by Karpatne et al. (2017), the Physics Guided Neural Network (PGNN) that includes a physics-based model, integrating it into the error function. With the help of this model, state estimates with larger deviations from a realistic scenario are marked as less favourable.

A time-aware class of the Neural Networks are Recurrent Neural Networks (RNN), which operate on time series of variables and have some memory of previous states. Thanks to the 'memory' of those systems, previous conditions can be weighted, and when applicable, incorporated into the current state. An advanced implementation of this is Long Short-Term Memory (LSTM), a network capable of deciding whether a previous event is still applicable to the current state, retaining the memory — and if otherwise, clearing it (Hochreiter and Schmidhuber, 1997).

2.4 Discussion

The limited roots in physics of many machine learning algorithms provide new potential for the nowcasting of deep-seated landslides. With its origin in computer sciences, an understanding of real-world physics is not the primary focus of most machine learning algorithms and methods. This poses a challenge for the integration in early warning systems, that are traditionally an extension of expert judgement rather than an 'expert' in itself. Furthermore, future experts will combine the roles of landslide geologist and data scientist, combining information sources and bridging gaps in data availability.

2.4.1 Data unification

Most machine learning techniques require all data to be in a consistent, monotonically increasing, spatio-temporal reference frame. Therefore, the resolution selection of the reference frame chosen has an influence on the outcome. Arnone et al. (2016) concluded a 20 m spatial resolution was optimal, while Shirzadi et al. (2019) concluded that a 10 m resolution was optimal. Both cases were higher than the resolution of the aforementioned satellite data products. Furthermore, re-projection between coordinate systems, as well as temporal interpolation, may introduce scaling of the original variable and a false perception of increased resolution.

Unified sampling is often required, with missing measurements blocking the process. Variables may need interpolation for features with lower spatial or temporal resolution, respecting the properties of the process underlying the variable, although higher resolutions in space and time may hide large-scale effects if analysis methods are not scaled appropriately with the increase in resolution. Moreover, in landslide nowcasting, the algorithm has to cope with missing data and the addition/update of historical data at a later stage.

Data cubes provide such unification of variables. The desired variables are preprocessed and spatiotemporally aggregated to a unified reference frame in space and time to facilitate data processing (Giuliani et al., 2019b; Sudmanns et al., 2019). For such cubes, a multidimensional array of variable, time, x and y can be sliced in any direction (variable, time, or location) to disclose relations in time, space, or between variables. The cube can be generated on a project basis, with only the necessary variables (Giuliani et al., 2020; Lewis et al., 2016), or be provided as 'analysis-ready data' by others (Brockmann Consult, 2018; Killough, 2018). However, for a time-critical application as nowcasting, these will have to be operational, 'live' data cubes.

2.4.2 Addition of local sensors

Local sensors may aid the interpretation of satellite products, and are a source of both calibration and validation for the satellite data products. For example, they can compensate for underestimated peak precipitation by satellite precipitation products due to spatial averaging (Brunetti et al., 2018) or validation of InSAR deformation analysis by GNSS sensors on the landslide (e.g., Dong et al., 2018). Local sensor data can be integrated in the process as well, especially when converted to the same reference frame as the satellite data products. Integration can be achieved either by mixing with the existing variables to increase local spatial or temporal resolution, or by rasterisation, creating a new variable from spatially interpolated sensor data. Furthermore, local observations allow for monitoring in geometries that are difficult to describe or observe from air or space, such as vertical walls (Castagnetti et al., 2014; Corsini et al., 2013).

Regional application of local sensors is not only feasible in the case of mass deployment of low-cost and low-maintenance sensors. Thomas et al. (2019) showed that even a single soil moisture sensor may be representative of a larger region and better represent the soil moisture conditions than a satellite soil moisture product.

2.4.3 Addition of physics

Physical constraints can be added at multiple stages of the process and bring the solution closer to the physical process. Simple physics, such as the tank model (Nie et al., 2017), may be used during variable pre-processing to amplify the information content of the variables. This integrates expert knowledge into the empirical system, unintentionally constraining the system to an assumed correlation. Including the same variable twice, once in a compound variable as well as independently, may over-represent the variable in the process.

During training of the algorithm, physics may be used to constrain the solutions to what is physically possible (e.g., landslides moving up-slope). This is implemented by the PGNN by penalizing solutions that are in conflict with such predefined rules (Karpatne et al., 2017). A major drawback is that both solutions cannot compensate for errors in either the composite variables or constraints. Wrong assumptions will lead to sub-optimal training and predictive power.

2.4.4 Early warning systems

The slow deformation behaviour of deep-seated landslides will not often prompt situations of immediate collapse or those that are life-threatening. However, warnings for strong acceleration, and associated risk for building and infrastructure damage, could be raised from a monitoring system. Early warning systems, solely based on (local) deformation measurements, have to detect precursory acceleration before a warning can be raised. Meanwhile, infrastructure and buildings on the slope are already undergoing increased stresses.

With satellite deformation tracking only, multiple acquisitions are necessary to trigger an alarm (Raspini et al., 2018; Intrieri et al., 2018). Current algorithms require at least 4–5 radar observations indicating acceleration to come to an early warning with a reasonably low false alarm rate (Intrieri et al., 2018). For example, given the 6-day revisiting time of the ESA Sentinel 1 satellite mission, this is a lead time of 24 days. Therefore, integration with other, more frequent measurements is necessary to come to an early warning and accelerate the detection of deformation anomalies. Moreover, a nowcasting system, including both driving and resulting factors, is less sensitive to the timeliness of the inputs and more suited for incorporation in an early warning system. However, special attention should be given to verify the performance for early warning of catastrophic accelerations of deep-seated landslides due to the rarity of such events.

Integration of the different data sources is an ongoing challenge faced by many remote sensing projects. The methods can be subdivided into traditional, statistical, or signal processing methods and artificial intelligence. The traditional methods have a mathematically defined behaviour, where the latter have proven to be very effective in recent applications, but are considered *blackboxes*.

The nowcasting system has to value known, historical information with respect to the current state. Traditional methods have limited flexibility in this respect. Possible pitfalls of the flexibility of machine learning methods are overfitting on previous deformation and unrealistic predictions due to the lack of physical constraints.

Unfortunately, it is practically impossible to guarantee that the more complex machine learning algorithms will always yield the desired warning, as it is impossible to simulate all time series and the non-linear behaviour does not allow for interpolation of the results. Such behaviour is undesirable in early warning systems, where there is a delicate balance in the perception of false alarms and missed detections (Intrieri et al., 2013). Furthermore, it poses the question of how to present the new, uncertain results to the public—an early warning system is only complete with a communication framework to distribute the warnings raised (Open-ended intergovernmental expert working group on indicators and terminology relating to disaster risk reduction, 2016).

By integrating the nowcast in the early warning system, alarms are now based on the interplay of variables, contrary to established single-variable intensity-duration thresholds. Furthermore, ensemble predictions, showing agreement or disagreement between ensemble members, can be used to warn against uncertain predictions. To increase predictive power, weather forecasts can be used to detect such problems beforehand (Alfieri et al., 2012). Together, these provide opportunities for the implementation of an unconventional but trustworthy warning system.

The application of continuous learning—the continuous optimization of the model to the newly recorded data—allows for the adaption to changing conditions, integrating new situations not encountered in the initial training phase and learning from previously missed stabilization or acceleration. However, continuous learning may mask slow changes, falsely updating the ground state.

2.4.5 Risk assessment and reduction

The quantitative hazard estimate from the nowcasting system can be projected onto objects of socio-economic importance, such as infrastructure and housing. The initial hazard estimate is hereby upgraded to a risk estimate—listing the potential damage incurred by the nowcasted, accelerated deformation. Moreover, the processing priority can be guided by the objects at risk, processing areas of high importance first or more frequently, thus maintaining regional coverage at the reduced computational cost. Furthermore, the empirical relations derived from the training of the machine learning algorithm are a valuable resource for the planning of mitigation measures.

2.5 Conclusions

Instead of describing the exact dynamics of each landslide, machine learning may serve a similar purpose in local and regional nowcasting and early warning systems. The continuous, wide-area time series from satellite remote sensing offer a unique opportunity to monitor deformation and hydro-meteorological conditions of landslides on a local and regional scale. In this paper, we showed that there are satellite remote sensing products available that capture the major contributors to the landslide process as well as the continuous, slow deformation of deep-seated landslides themselves.

The limited frequency of deformation updates necessitates the integration of data from other, more frequent, sources to continuously estimating the current system state. Simple physics and proxy indicators may compensate for variables that cannot be observed directly from space. The different machine learning algorithms we listed have been demonstrated to be capable of processing the large data streams available to a nowcast of deformation on a local scale.

A satellite remote sensing landslide nowcasting system can be applied on demand, and has the potential to be applied globally, independent of terrain accessibility or local budget, and provides additional protection to those affected. However, integration in early warning systems on both a local and regional scale will require further refinement of the algorithms and a new approach to 'live', unified data integration.

Chapter 3

World-wide InSAR sensitivity index

Published previously as: van Natijne, A., Bogaard, T., van Leijen, F., Hanssen, R., Lindenbergh, R., 2022a. World-wide InSAR sensitivity index for landslide deformation tracking. *International Journal of Applied Earth Observation and Geoinformation*, 111, 102829. `https://doi.org/10.1016/j.jag.2022.102829`.

Abstract

Landslides are a major geohazard in hilly and mountainous environments. In-situ inspection of downslope motion is costly, sometimes dangerous and, requires prior knowledge of the existence of a landslide. Remote sensing from space is a way to detect and characterize landslides systematically at large scale. Interferometric Synthetic Aperture Radar (InSAR) has shown to be a valuable resource of deformation information, but it requires expert knowledge and considerable computational efforts. Moreover, the successful application of InSAR for landslides requires a favorable acquisition geometry relative to the landslide deformation pattern. Consequently, there is a need for a widely applicable tool to assess the potential of InSAR at a particular location a priori. Here we present a novel, generic approach to assess the potential of InSAR-based deformation tracking, providing a standardised and automated method applicable on any slope. We define the detection potential as the sensitivity of InSAR to detect downslope displacement combined with the presence of coherently scattering surfaces. We show that deformation can be detected on at least 91% of the global landslide-prone slopes, and provide an open source Google Earth Engine tool for the quick assessment of the availability of potential coherent scatterers. This tool enables any person interested in applying InSAR to routinely assess the potential for monitoring landslide deformation in their region of interest.

3.1 Introduction

With an estimated average economic loss of € 4.7 billion per year in Europe alone, landslides are a major hazard (Haque et al., 2016). Knowledge of the landslide deformation behaviour provides insight in its characteristics and potential societal impact (Intrieri et al., 2019; van Natijne et al., 2020). Recent case studies show that satellite measurements of landslide deformation allow for the early detection of accelerated deformation preceding a catastrophic event (Intrieri et al., 2018; Carlà et al., 2019a).

Several methods are available to obtain deformation measurements, each with different characteristics, temporal sampling, and spatial coverage. Local techniques include crackmeters, extensometers and inclinometers, that quantify in-situ deformation at the specific location at the landslide or building they are applied to (Logar et al., 2017; Segalini et al., 2019). Slope scale techniques, used to quantify differential deformation within a landslide, include total station measurements, and Global Navigation Satellite System (GNSS) measurement campaigns (Benoit et al., 2015). However, those techniques require access to the landslide for installation, maintenance and/or operation of sensors, reflectors or benchmarks.

Terrestrial laser scanning, photogrammetry and ground based radar are slope scale alternatives that can be deployed elsewhere, without access to the landslide, given free visibility of the landslide features (Jaboyedoff et al., 2012; Dewitte et al., 2008; Antonello et al., 2004). Aerial laser scanning and photogrammetric campaigns provide regional coverage, where especially laser scanning is able to penetrate vegetation on slopes. Deformation measurements can be based on feature tracking, as well as on a volumetric comparison of surface models (Zieher et al., 2019; Corsini et al., 2013). However, unless automated, all these measurements provide sparse, infrequent deformation measurements, that mask short-term variations in a long-term trend (Mansour et al., 2011).

Satellites provide an ideal platform for systematically repeating surveys over larger areas. Archives of wide scale acquisitions make it possible to detect previously unknown landslides and analyze historic landslide behaviour. Image-based correlation techniques are used for deformation tracking in both optical and radar amplitude imagery, tracking features in an image sequence over time (Mondini et al., 2019; Singleton et al., 2014; Lacroix et al., 2018; Stumpf et al., 2017). However, their efficacy is limited to fast-moving landslides (Bickel et al., 2018). Furthermore, optical imagery is ineffective in case of cloud coverage.

These limitations are not applicable to deformation measurements obtained by satellite-borne Synthetic Aperture Radar Interferometry, InSAR (Hanssen, 2001). In less than two decades, InSAR has become an important information source for landslide deformation studies (Colesanti et al., 2003; Berardino et al., 2003; Hilley et al., 2004; Colesanti and Wasowski, 2006; Tofani et al., 2013b), especially for slow to very slow landslides (0 − 1.6 m/year) (Hungr et al., 2014). These landslides can be tracked with coherent scatterers, natural or man-made reflectors that show phase-consistent scattering behaviour over time (Ferretti et al., 2001; Hanssen, 2001; Berardino et al., 2003; Komac et al., 2015).

InSAR studies consider a large variation in landslide types, processing techniques and objectives. Different deformation types include large scale block deformation (Czikhardt et al., 2017), rock slides (Lauknes et al., 2010; Delgado et al., 2011) and mud slides (Sun et al., 2015). Often, studies are local, and some studies validated InSAR results using field GPS measurements (Peyret et al., 2008; Yin et al., 2010; Komac et al., 2015). Regional studies, such as Aslan et al. (2020), are still rare, although continental scale InSAR products are under development (Crosetto et al., 2020). Others estimate landslide parameters based on InSAR time series in in-depth case studies (Intrieri et al., 2020; Schlögel et al., 2015).

Due to the numerous potential error sources, expert knowledge is required for the successful application of InSAR (van Leijen, 2014). In mountainous environments there is an additional effect on InSAR processing of the complex interaction with topography and the atmosphere (Hanssen, 2001). Furthermore, due to the data heavy character of time series analysis, significant computational efforts are required. Therefore, it would be beneficial to be able to assess the applicability of InSAR before engaging in an in-depth study.

For this purpose, Cascini et al. (2009, 2010) introduced the concept of an InSAR 'visibility map' for landslides. However, it did not account for geometric distortion due to the effect of topography on the radar signal. An alternative 'feasibility index' was proposed by Notti et al. (2010). They proposed a surface geometry based method to estimate the likelihood of extracting deformation time series using InSAR, where feasibility was defined as the chance of the availability of a persistent scatterer in a series of SAR images. Their concept is implemented and extended in a range of later studies by Notti et al. (2011, 2014); Plank et al. (2010, 2012); Herrera et al. (2013); Cigna et al. (2013); Bianchini et al. (2013); Ciampalini et al. (2015); Novellino et al. (2017); Bonì et al. (2020) and Del Soldato et al. (2021). However, the landslide deformation pattern was not incorporated.

Here we present a novel, comprehensive method to a priori assess the applicability of InSAR in landslide deformation detection at global scale. To be able to quantify the minimal detectable deformation (Teunissen, 2006; Baarda, 1968), we have adapted the sensitivity index (Chang et al., 2018) to the landslide process. The sensitivity index is available without prior knowledge of the deformation pattern or radar imagery, and is aimed at desk studies of the applicability of later InSAR landslide deformation analysis. Thanks to the sensitivity index, we could, for the first time, globally quantify the possibilities for InSAR slope monitoring.

Furthermore, we qualify the ability to extract deformation time series from the InSAR signal in a detection potential indicator. Finally, we provide a public detection potential tool in Google Earth Engine, that allows for an in-depth analysis of individual slopes. Together, these tools provide landslide experts, before engaging in an in-depth study, with a semi-automated assessment of the potential of landslide deformation tracking with InSAR.

In Section 3.2, we outline the principles of our method, followed by a detailed description of the calculation of the sensitivity index and detection potential indicator in Section 3.3. The tools accompanying this manuscript are demonstrated on a real world example in Section 3.4. Section 3.5 includes statistics on the global sensitivity index. Finally, we discuss the underlying assumptions in Section 3.6.

3.2 Defining InSAR measurement geometry

Surface geometry Landslides are gravity induced and move downwards along the slope direction (Singleton et al., 2014). At a given time, the displacement of the landslide in the along-slope direction can be described by the instantaneous downslope or true velocity. The slope, β, is defined as the steepest downward direction, described by the aspect, α, in clockwise degrees from north ($0°– 360°$). The slope steepness, β, is defined as the vertical angle from the horizontal.

A digital elevation model can be used to estimate the surface topography parameters, slope and aspect. Here we used the Copernicus DEM (Fahrland, 2020). The 30 m resolution at the equator is one of the highest for elevation models with (near) global coverage. The resolution impacts the representation accuracy of steep slopes, while the estimation of the aspect is less affected (Grohmann, 2015). For calculation convenience, flat slopes, i.e. $\beta \leq 5°$, are ignored in this study as the presence of a landslide system is expected to be extremely unlikely.

Radar geometry The geometry of the InSAR acquisitions for a particular location is defined by the orientation of the line-of-sight (LOS) unit vector towards the satellite at the moment of imaging (Hanssen, 2001). Projected onto the horizontal plane, its angle from the north is referred to as the azimuth look direction (ALD), which is typically east-southeast for the descending (southbound) satellite orbit, and west-southwest for the ascending (northbound) orbit. The angle between the LOS unit vector and the zenith direction is referred to as the incidence angle, θ, see Fig. 3.1, which is typically a value between $\theta_{\min} = 29°$and $\theta_{\max} = 46°$for Sentinel-1. Exact calculations are discussed in Section 3.3.1.

Measurement geometry Key concept is the interaction between the radar geometry, surface geometry and landslide deformation. Two geometries inhibit proper interpretation of the radar signal: shadow and layover. In the case of shadow, the radar signal is blocked by topography. With layover, scatterers can no longer be unambiguously attributed to a single point on the Earth surface, as the radar signal scattered on multiple locations, at the same distance to the satellite, simultaneously and the signals are superimposed on each other. Fig. 3.1 illustrates how these effects affect the radar acquisition in mountainous terrain.

To detect these effects in a 3D world, the apparent slope is a helpful variable. The apparent slope β', is the slope as seen in the line-of-sight of the Sentinel-1 satellite:

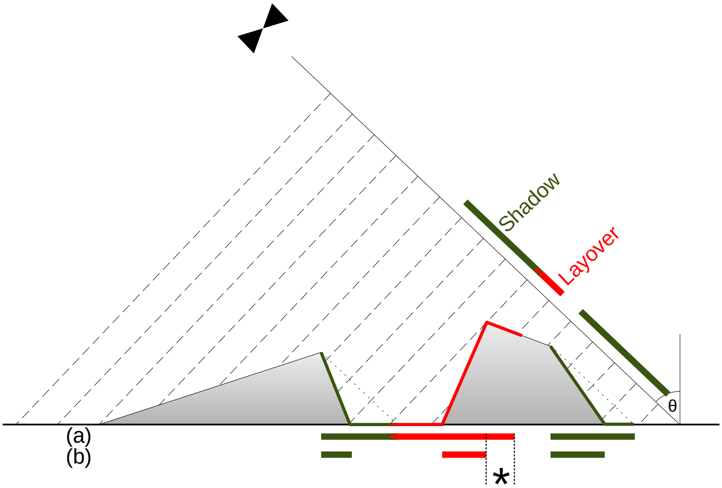

Figure 3.1: Effects of surface topography on the radar image, shown in both the radar line-of-sight as the horizontal plane. The mapping from topography to line-of-sight is illustrated by the dashed lines, where the radar signal is simplified to a parallel wave front with incidence angle θ. Under (a), the effects of surface topography on the radar image are shown mapped onto a DEM. Except for the area indicated by the asterisk, standard shadow algorithms in GIS are capable of modelling the destructive effects of topography on the radar signal. In comparison, (b) shows the effects that are locally detectable, without considering the surrounding surface topography, see Fig. 3.4. Image inspired by Pinel et al. (2014).

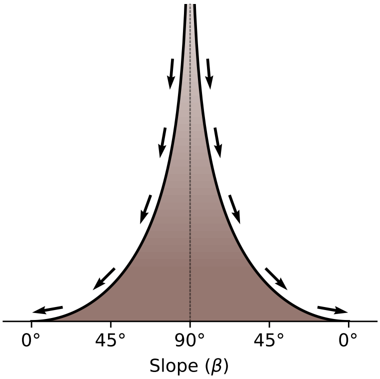

Figure 3.2: Profile of a synthetic, radially symmetric mountain. The arrows indicate the expected sliding direction of a landslide.

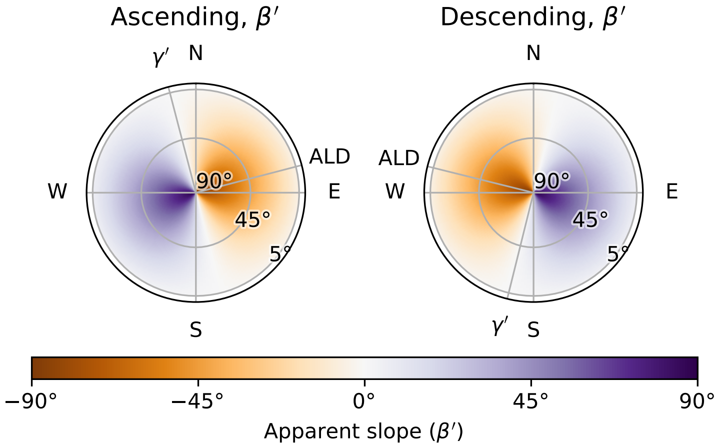

Figure 3.3: Analysis of the apparent slope of an artificial, radially symmetric mountain, as illustrated in Fig. 3.2, at latitude $\phi \approx \pm 46°$. Fig. 3.4 shows a 2D schematization of the potential effects of surface geometry on the radar signal.

$$\beta' = \beta \sin(\gamma' - \alpha), \tag{3.1}$$

with the terrain slope, β, aspect, α, and satellite heading, γ', corrected for meridian convergence. Fig. 3.3 illustrates the apparent slope in both ascending and descending orbits, for an artificial, radially symmetric mountain (Fig. 3.2).

Given the incidence angle, θ, the geometric effects are found by simple relations: shadow occurs if $\beta' \leq -\theta$, layover occurs when $\beta' \geq 90° - \theta$. These effects are illustrated in Fig. 3.4, for both the minimum and maximum incidence angle of Sentinel-1. However, on slope scale, as shown in Fig. 3.1, the effect of shadow and layover by neighbouring topography requires further modelling of the line-of-sight for an accurate representation.

3.3 Sensitivity index and detection potential

The application of InSAR deformation measurements is feasible when the following conditions are met: (i) the presence of coherent scatterers; and (ii) the availability of sufficient radar acquisitions with (iii) a geometry sensitive to deformation. Our work consists of two methods to assess these requirements (see Fig. 3.5). First we derive the sensitivity index, a static analysis of the lower bound of the sensitivity of Sentinel-1 to downslope deformation of the landslide. Second we define the detection potential indicator, which is a Google Earth Engine based tool to analyze the availability of imagery and scatterers from the Sentinel-1 time series contained in the Google Earth Engine archives.

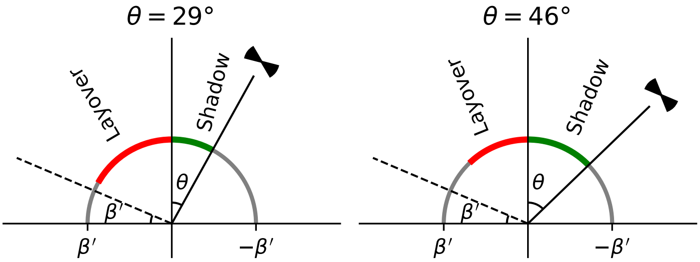

Figure 3.4: 2D schematization of the effects of the surface geometry on the radar geometry. Illustrated are the minimum and maximum incidence angles θ of Sentinel-1 for a variable, apparent slope β' $[-90°, 90°]$. Only the local effects, induced by the DEM-pixel itself, are described by these relations. Shadow or layover, induced by nearby topography, cf. Fig. 3.1 (b), cannot be captured this way.

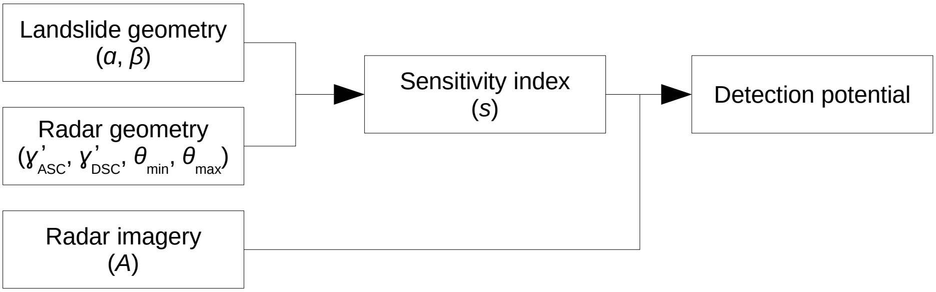

Figure 3.5: An overview of the workflow and variables. Geometric analysis of the landslide and radar geometries (§ 3.2) leads to the sensitivity index for landslide deformation detection (§ 3.3.1). The detection potential (§ 3.3.2) is estimated by exploratory data analysis of archived radar imagery using Google Earth Engine.

Definition of the sensitivity index Radar observations are only sensitive to deformation components in the propagation direction of the radar signal, the line-of-sight. Given the direction of downslope deformation, the sensitivity index, $s \in [0, 1]$, is calculated by the orthogonal projection of the downslope unit vector onto the line-of-sight of the radar satellite (Chang et al., 2018). The most conservative incidence angle is used for the radar parameters, i.e. the incidence angle that yields the lowest sensitivity.

The sensitivity index is based on radar and surface geometry only, and the lower-bound is known without knowledge of the radar acquisitions. As such, the sensitivity index is a geometric property, that can be computed without the computational burden of downloading and processing large quantities of radar data. This index can be implemented in most Geographic Information Systems and is provided by us as a Google Earth Engine tool, and is a valuable assessment tool in the early planning phase.

Definition of the detection potential The detection potential is quantified here by the estimated availability of presumedly coherent scatterers via the so-called method of normalized amplitude dispersion (Ferretti et al., 2001). Hereby, the amount of variability of the amplitude per radar-pixel in time is used as a proxy for the level of phase stability. Normalized amplitude dispersion is used by various InSAR packages as a convenient a priori selection technique for the selection of potential coherent scatterers (van Leijen, 2014). Although this method was originally aimed at coherent point scatterers, our application on multilooked and calibrated amplitude (GRD) instead of complex (SLC) data yields a proxy indication of coherent distributed scatterers as well. Only when a radar-pixel shows coherent scattering during a significant part of the full temporal extent, a displacement time series can be estimated. When the scatterer is disturbed or temporally obstructed, for example by snow, the scatterer (temporarily) loses coherence.

3.3.1 Sensitivity index algorithm

Starting point is the digital elevation model, from which the surface geometry is derived using standard functions available in most GIS packages (see Fig. 3.6). The surface geometry is derived from the DEM and combined with the radar geometry. On potential landslide slopes, the destructive geometric effects, shadow and layover, on the radar signal are estimated.

The system is operated on a tile basis, following the original 1°by 1°($\sim 100 \times 100$ km) tiling of the Copernicus DEM data. The tiles can be merged into a regional or world map upon completion, as desired. Here we provide a detailed, step-by-step overview of the processing steps. Finally, we provide an analysis of the computational efficiency of the algorithm.

Local Cartesian reference frame To ease calculations, a local Cartesian coordinate system is constructed for each DEM-pixel. Locally, the Earth is assumed

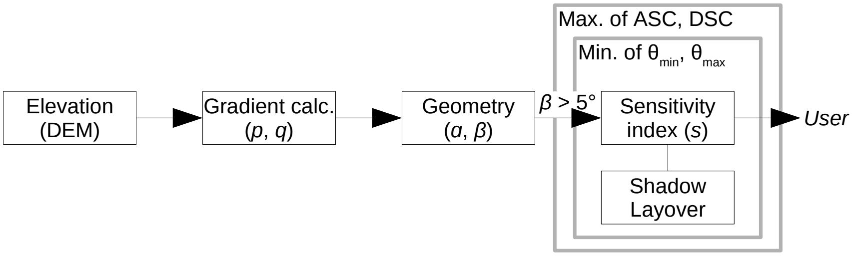

Figure 3.6: Workflow for the calculation of the sensitivity index. The process is repeated for the two orbital directions, ascending and descending, and the extremes of the incidence angle ($\theta_{\min}$, $\theta_{\max}$). Result is a single value, the sensitivity index, the lower bound of the detectability of displacement in the radar signal. No radar imagery is required, only a digital elevation model and four orbit parameters.

to be spherical, with an apparent radius, $\rho(\phi)$, dependent on latitude ϕ, estimated from the WGS84 ellipsoid underlying the Copernicus DEM. At pixel level, the Earth is assumed to be flat, and the curvature of the Earth with respect to its neighbours ignored. The apparent radius at latitude ϕ $[-90°, 90°]$ is given by (Husár et al., 2017):

$$\rho(\phi) = \frac{a\sqrt{1 - \frac{a^2-b^2}{a^2}}}{\sqrt{1 - \frac{a^2-b^2}{a^2}\cos^2(\phi)}} \tag{3.2}$$

with equatorial radius $a = 6378137$ meters and polar radius $b = 6356752$ meters. The resolution in x and y, in meters, at latitude ϕ is then estimated as:

$$\begin{gathered} r_x(\phi) \approx \rho(\phi) \cdot r_\lambda \cdot \cos(\phi), \\ r_y(\phi) \approx \rho(\phi) \cdot r_\phi, \end{gathered} \tag{3.3}$$

with r_ϕ and r_λ the latitudinal and longitudinal resolution in radians.

Surface geometry The estimation of slope and aspect are based on the gradient calculation methods described by Horn (1981). These methods are the de-facto standard for fast slope and aspect calculations in GIS (GDAL, 2020). The method is based on a weighted average of nearby pixels.

The neighbouring pixels in a 3×3 neighbourhood of elevations around $z_{0,0}$ are referenced to as follows:

$$\begin{array}{c|c|c} z_{-1,-1} & z_{-1,0} & z_{-1,1} \\ \hline z_{0,-1} & z_{0,0} & z_{0,1} \\ \hline z_{1,-1} & z_{1,0} & z_{1,1} \end{array}. \tag{3.4}$$

The indices on the y-axis are inverted to match the convention on image coordinates, where the y-axis points down.

The weighted gradients in x-direction (p) and y-direction (q) are estimated as

$$\begin{aligned} p &= \tfrac{(z_{-1,1}+2z_{0,1}+z_{1,1})-(z_{-1,-1}+2z_{0,-1}+z_{1,-1})}{8r_x(\phi)}, \\ q &= \tfrac{(z_{-1,1}+2z_{-1,0}+z_{-1,-1})-(z_{1,1}+2z_{1,0}+z_{1,-1})}{8r_y(\phi)}. \end{aligned} \tag{3.5}$$

The gradients p and q yield a tangent, downslope vector, $\mathbf{t}$,

$$\mathbf{t} = \frac{-1}{\sqrt{(1+p^2+q^2)(p^2+q^2)}} \begin{pmatrix} p \\ q \\ p^2+q^2 \end{pmatrix}. \tag{3.6}$$

If slope and aspect are already available, as in Google Earth Engine, the downslope vector may be constructed from them. With aspect α and slope β, the downslope vector is calculated as,

$$\mathbf{t} = \begin{bmatrix} \sin\alpha\cos\beta \\ \cos\alpha\cos\beta \\ -\sin\beta \end{bmatrix}. \tag{3.7}$$

Radar geometry First, the effective heading of the satellite is estimated. The heading of the ascending orbit is approximated for latitude ϕ by Capderou (2005) as

$$\gamma'(\phi) \approx \arctan \frac{\cos i - \frac{\cos^2\phi}{\kappa}}{\sqrt{\cos^2\phi - \cos^2 i}}, \tag{3.8}$$

with i the satellite inclination and κ the mean motion, the number of revolutions per day. The effect of meridian convergence within the radar image is neglected. The heading of the descending orbit is $180° - \gamma'(\phi)$.

Similar to the downslope vector $\mathbf{t}$, the vector for the satellite line-of-sight is constructed. The vector, $\mathbf{r}$, points upward, from the Earth surface to the satellite. With satellite heading γ', positive clockwise from the north, and θ, the incidence angle from the vertical,

$$\mathbf{r} = \begin{bmatrix} -\cos\gamma'(\phi)\sin\theta \\ \sin\gamma'(\phi)\sin\theta \\ \cos\theta \end{bmatrix}. \tag{3.9}$$

Shadow and layover The shadow and layover as derived from the apparent slope, shown in Figs. 3.4 and 3.3, represent only local effects, generated by the slope itself. However, as shown in Fig. 3.1, steep mountain slopes may affect larger regions on and at the foot of the slope. Following Cigna et al. (2013); Plank et al. (2012) and Cigna et al. (2012), we used a GIS-based shadow algorithm.

For the shadow estimation, the sun parameters are replaced with the satellite viewing geometry, $\gamma' + 90°$ from north and the maximum incidence angle ($\theta_{\max}$). For the layover estimate, the satellite is placed in opposite direction of $\gamma' - 90°$, at the minimum incidence angle ($\theta_{\min}$) from the horizontal. However, layover does not only affect the layover-inducing slope, but also areas above and below the slope, as shown in Fig. 3.1. This requires an extension to the shadow algorithm, where both the layover-inducing DEM-pixel as well as the DEM-pixel affected by the layover are marked.

For each DEM-pixel the line-of-sight to the radar is probed, until either obstructing topography is encountered, or the maximum elevation in the tile is exceeded. If no obstructing topography is found, there is an unobstructed line-of-sight to the satellite.

Sensitivity index The sensitivity index is, by definition, the projection of downslope deformation direction on the line-of-sight of the radar system (Chang et al., 2018):

$$s \doteq |\mathbf{t} \cdot \mathbf{r}|, \tag{3.10}$$

with downslope unit vector ($\mathbf{t}$) from Eq. (3.6) or (3.7), and the line-of-sight unit vector ($\mathbf{r}$) from Eq. (3.9). Where shadow or layover prevent radar measurements, the sensitivity index is set to zero.

Algebraic expressions exist for the two descriptions of the surface geometry. For the gradient method by Horn (1981), the sensitivity index is a combination of Eqs. (3.6), (3.9), and (3.10),

$$s(p,q,\theta,\phi) = \frac{\left| \begin{matrix} \left(p^2+q^2\right)\cos(\theta) + \\ \begin{pmatrix} -p\cos(\gamma'(\phi)) + \\ q\sin(\gamma'(\phi)) \end{pmatrix} \sin(\theta) \end{matrix} \right|}{\sqrt{p^2+q^2}\sqrt{p^2+q^2+1}}, \tag{3.11}$$

with satellite effective heading $\gamma'(\theta)$ and incidence angle θ. Likewise, if the slope (β) and aspect (α) are known instead of the gradients, a combination of Eqs. (3.7), (3.9) and (3.10) leads to:

$$s(\alpha,\beta,\theta,\phi) = |\sin(\beta)\cos(\theta) + \sin(\theta)\sin(\alpha - \gamma'(\phi))\cos(\beta)|. \tag{3.12}$$

The results are shown in Fig. 3.7 (a, b, d, e).

Orbit aggregation The sensitivity index requires the exact incidence angle, see Eq. (3.9), that follows from actual InSAR data processing which is not available in the planning phase. Therefore, to include the unknown incidence angle in the planning, we conservatively use the minimum sensitivity from the two extremes of the incidence angle ($\theta_{\min}$, $\theta_{\max}$). The lowest sensitivity index found is a lower bound of the index for that slope, and can be quantified without knowledge of the exact orbits. This procedure is shown in Fig. 3.7 (a, f, g), and the final result is illustrated in 3D in Fig. 3.8.

For both the ascending and descending orbit, the minimum sensitivity index is taken, i.e.,

$$s_{\text{ASC}} = \min(s_{\theta_{\min}}, s_{\theta_{\max}}). \tag{3.13}$$

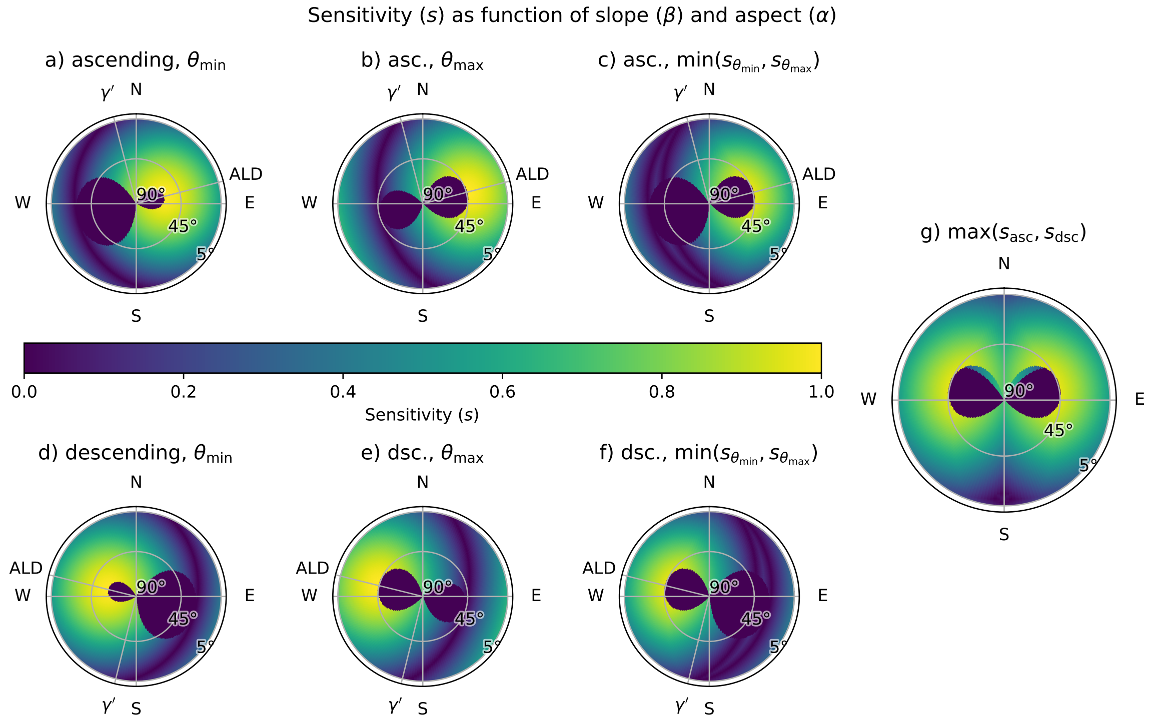

Figure 3.7: The line-of-sight range sensitivity is expressed as a function of satellite and terrain parameters for latitude $\phi \approx \pm 46°$. The sensitivity is taken as the minimum sensitivity for the minimum and maximum incidence angle in order to provide conservative estimates. The effects of shadow and layover, as shown in Fig. 3.4, are resolved at DEM-pixel scale, therefore only the effects listed under (b) of Fig. 3.1 are resolved. Note that graph is based on an artificial, radial slope, as illustrated in Figs. 3.2 and 3.8, and does not represent a natural slope distribution. In practice, very steep slopes ($\geq 45°$) are rare, and comprise less than 1% of the slopes $> 5°$ in the Copernicus DEM.

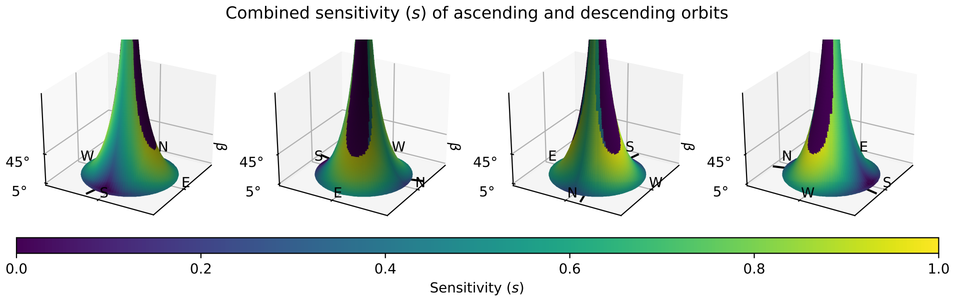

Figure 3.8: A 3D interpretation of the results from Fig. 3.7. This image shows more clearly how shadow and layover affect only very steep slopes. Displacements along these slopes, as well as south facing, low relief slopes are less likely to be detectable. The ascending and descending orbit directions are shown in black at the bottom.

Likewise, s_{DSC} is calculated. The highest sensitivity index (s) of either ascending or descending orbit is the principal reporting parameter in the planning stage, when data from both ascending and descending orbit is expected to be available:

$$s \geq \max(s_{\mathrm{ASC}}, s_{\mathrm{DSC}}). \tag{3.14}$$

Landslide velocity The sensitivity index is defined as the projection of the downslope displacement unit vector onto the line-of-sight, and is a scale factor for the downslope displacement to the change in the line-of-sight range as observed by InSAR. For example, under the assumption of only downslope deformation, the downslope average velocity, $v_{\mathrm{downslope}}$, is the line-of-sight average velocity, v_{LOS}, scaled by the sensitivity index, s,

$$v_{\mathrm{downslope}} = \left| \frac{v_{\mathrm{LOS}}}{s} \right|. \tag{3.15}$$

Likewise, via standard error propagation, the upper bound of the standard deviation may be found. In the case of a linear, average line-of-sight velocity:

$$\sigma_{v_{\mathrm{downslope}}} = \frac{\sigma_{v_{\mathrm{LOS}}}}{s} \ \mathrm{mm/yr}, \tag{3.16}$$

with s and the expected standard deviation of the linear line-of-sight velocity $\sigma_{v_{\mathrm{LOS}}}$. When the lower bound of the sensitivity index, as follows from Eq. (3.13), is used, Eqs. (3.15) and (3.16) provide estimates for their maximum values.

Computational efficiency Computation of the sensitivity index for all 26 223 Copernicus DEM tiles required 13 hours on an Intel Xeon W-2123 (4 cores, 8 threads, 3.6 GHz) with 32 GB RAM and network storage. The sensitivity index was processed in Python (van Rossum et al., 2008) using Rasterio (Gillies et al., 2013), GeoPandas (Jordahl et al., 2020), GDAL (GDAL/OGR contributors, 2020), NumPy

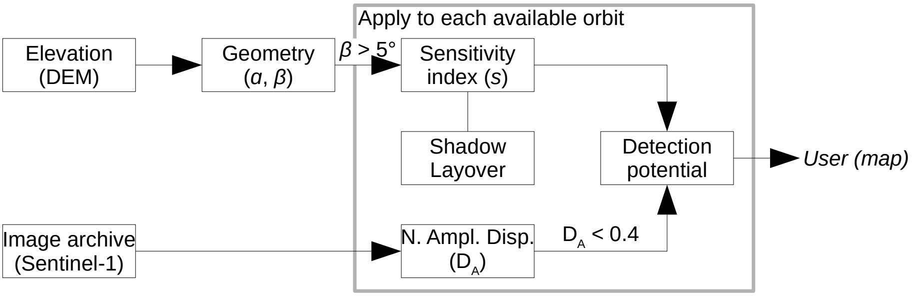

Figure 3.9: InSAR detection potential is defined as the product of the sensitivity index, shadow and layover, as well as scattering characteristics estimated from imagery. The application of InSAR is only feasible in the presence of unobstructed scattering surfaces on slopes with a sufficient sensitivity index for the expected landslide velocity.

(Harris et al., 2020), and accelerated by Numba (Lam et al., 2015). Figures were generated using Matplotlib (Hunter, 2007). Thanks to the algebraic expressions, Eqs. (3.11) and (3.12), calculation of the sensitivity index for four cases (ascending/descending, $\theta_{\mathrm{min}}/\theta_{\mathrm{max}}$) is a trivial operation. However, the estimation of shadow and layover effects is more involved.

Our simple, iterative algorithm to compute the sensitivity index does not require cluster computing and is suitable for desktop computers due to its low memory footprint, that allows for parallel processing of multiple tiles. Moreover, the theoretical efficiency of $\mathcal{O}(n)$ is not indicative of the actual performance per tile. As flat areas are ignored, tiles over river deltas require very little computations. Tiles with large height differences are the most computationally intensive, as they require most iterations to resolve shadow and layover.

3.3.2 Detection potential algorithm

The estimation of the detection potential is an extension to the sensitivity index estimation, but now including a preliminary analysis of the available radar imagery. Moreover, the procedure, illustrated in Fig. 3.9, is implemented differently from the sensitivity index to match the structure of Google Earth Engine. In this structure, the algorithm is stored and evaluated in Google's data centers, where a 'multi-petabyte data catalog' and 'high-performance computing' facilities are co-located (Gorelick et al., 2017). Only once a portion of the map is requested, will the algorithm be evaluated for the region shown. The technology has proven to enable global analysis of decadal time series (Donchyts et al., 2016; Hansen and Loveland, 2012).

Google Earth Engine has an archive of Sentinel-1 GRD amplitude imagery available for processing. The availability of Sentinel-1 acquisitions enables us to use the actual incidence angle (θ) to estimate the sensitivity index, rather than estimate the lower bound based on the theoretical range of the incidence angle. Unfortunately, the satellite heading (γ') is not provided in or with the radar imagery, and is estimated by Eq. (3.8).

The Copernicus DEM was not available in Google Earth Engine at the time of writing. Instead, SRTM (Farr et al., 2007) is available, and is supplemented with ALOS DEM (JAXA, 2019; Tadono et al., 2014) for higher latitudes. Predefined methods are available for the estimation of the surface geometry parameters, slope (β) and aspect (α) (Google, 2021a). Due to computational limitations, a global analysis, such as with the global sensitivity index, is impossible.

Shadow and layover are approximated with a shadow model that takes single values for heading and incidence angle. This shadow model cannot be adapted to the incidence angle at DEM-pixel level, and a conservative value is taken instead. Furthermore, the shadow model is unable to detect layover in the region indicated by the asterisk in Fig. 3.1. On steep Alpine slopes, 6% of the pixels affected by layover stays undetected. However, this is just 0.02% of the total area of Alpine SRTM tile `N47E011`, that was tested as a sample.

Normalized amplitude dispersion The normalized amplitude dispersion is defined as the ratio between the standard deviation of the amplitude, σ_A, and the mean amplitude, μ_A, of a stack of radar images (Ferretti et al., 2001), applied on linear amplitude values:

$$D_A \doteq \frac{\sigma_A}{\mu_A}. \tag{3.17}$$

The normalized amplitude dispersion is a popular method for the initial selection of potentially coherent scatterers, as a low normalized amplitude dispersion is an indicator of high phase coherence (Ferretti et al., 2001). Thresholds for D_A vary, depending on the application, between 0.25 and 0.6 (van Leijen, 2014; Hooper, 2008).

In Google Earth Engine only Ground Range Detected (GRD) imagery is available, that is a multi-looked (spatially averaged) amplitude derivative of the complex radar imagery (Google, 2021b). The use of the normalized amplitude dispersion on this type of imagery is unconventional, but is possible due to the radiometric consistency between the two products (Schubert and Small, 2016). However, as the multi-looking has a dampening effect on the amplitude dispersion, an area specific user interpretation of the normalized amplitude dispersion is recommended.

Polarity Given the radar geometry for a specific orbit provided by Google Earth Engine, the effect of downslope displacement on the line-of-sight range may be estimated. The polarity ($\text{sgn}(\mathbf{t} \cdot \mathbf{r}) \in \{-1, 0, +1\}$) indicates if downslope displacement is expected to shorten or lengthen the line-of-sight range. Together with the sensitivity index, the polarity enables preliminary estimates of the InSAR signal to be expected, based on prior knowledge of the specific slope. Moreover, spatial variability in the line-of-sight deformation direction could be misinterpreted for noise, but are not unlikely in mountainous topography.

User interface In the Google Earth Engine tool, the detection potential is presented to the user as a filtered sensitivity index: the sensitivity index is shown whenever the normalized amplitude dispersion is below a threshold of 0.4. The application leaves three variables for the user to decide: i) the orbit to analyze; ii) the time span to analyze and iii) the region of interest. First two parameters are offered to the user as selection boxes. The third is provided implicitly by moving around the map. Section 3.4.2 includes a demonstration of the application and associated user interface.

3.4 Global sensitivity index statistics and detection potential application

This study is accompanied by two tools: i) the first global sensitivity index for landslide deformation detection by InSAR, and ii) a Google Earth Engine tool for local analysis of the sensitivity index and detection potential. Both results are freely available to future users, either as data product, or as application and algorithm.

3.4.1 Global sensitivity index

The global sensitivity index, illustrated in Fig. 3.10, is available for download. Potential applications include combinations with regional landslide inventories or susceptibility maps, for example for monitoring planning. Tiling is equal to the tiling of the Copernicus DEM, and consists of 26 223 tiles of $1^\circ \times 1^\circ$. Each tile consists of three layers: s_{ASC}; s_{DSC} and s. The data is distributed as GeoTIFF, and is compatible with most common GIS software packages.

Sensitivity index values are stored as 16 bit floats, with a variable longitude resolution, matching the variation of the Copernicus DEM. Flat regions, including water, as well as gaps in the data are marked as no data. The global tile set is only 330 GiB in size, with individual tiles ranging between 50 kiB and 90 MiB. Moreover, the associated algorithm is available.

The global sensitivity index and Python code are available for download via:
doi:10.4121/14095777[1] (van Natijne et al., 2022b).

3.4.2 Sensitivity index and detection potential in Google Earth Engine

The Google Earth Engine tool allows the user for a more detailed study of in the sensitivity index and detection potential in their area of interest. At a regional level, the sensitivity index is shown (Fig. 3.11). Locally, the application will search the Google Earth Engine archives for available Sentinel-1 imagery in the desired time frame and offer the user a sensitivity index tailored to an orbit of choice.

---

[1] `https://doi.org/10.4121/14095777`

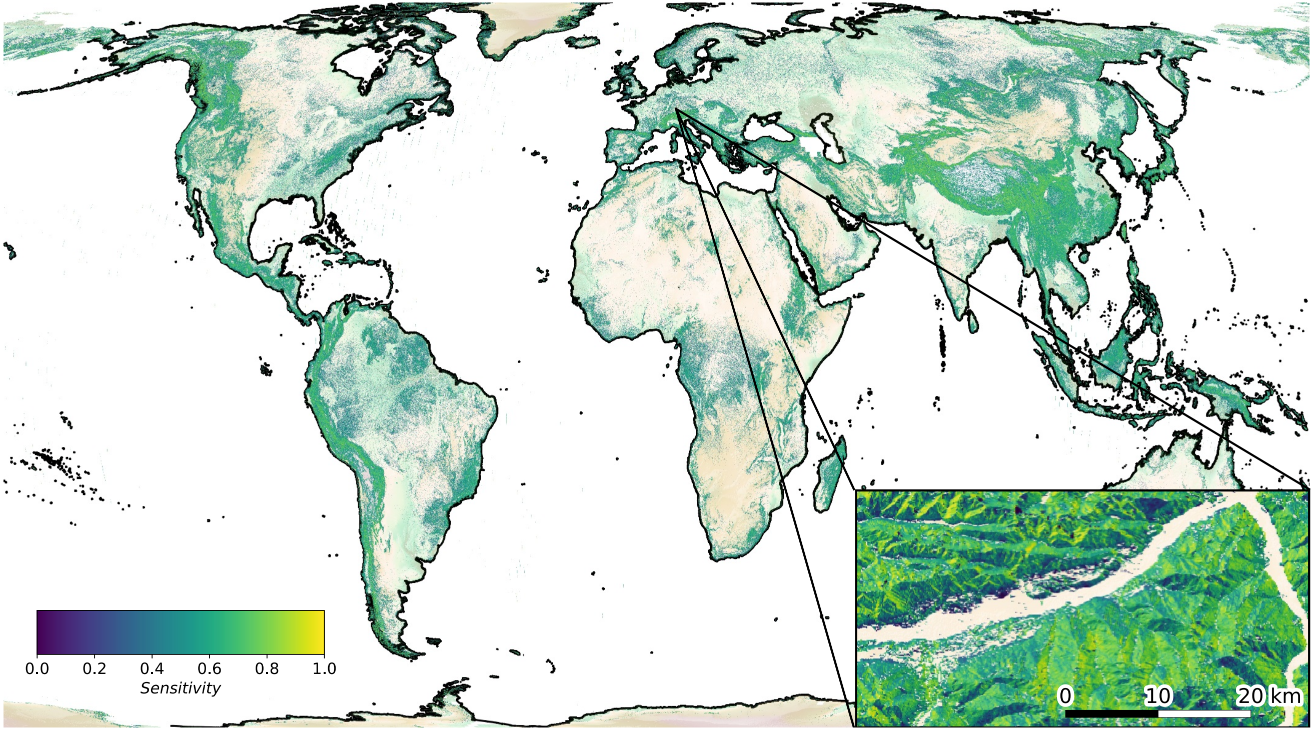

Figure 3.10: Global sensitivity index and an excerpt over the Inn valley, around Innsbruck, Austria. Shown is the combined sensitivity index, the highest sensitivity from the conservative, lower-bound, estimates of the sensitivity index for the ascending and descending orbits. The index is available globally, at around 30 m resolution. (Background: Copernicus DEM and OpenStreetMap coastlines)

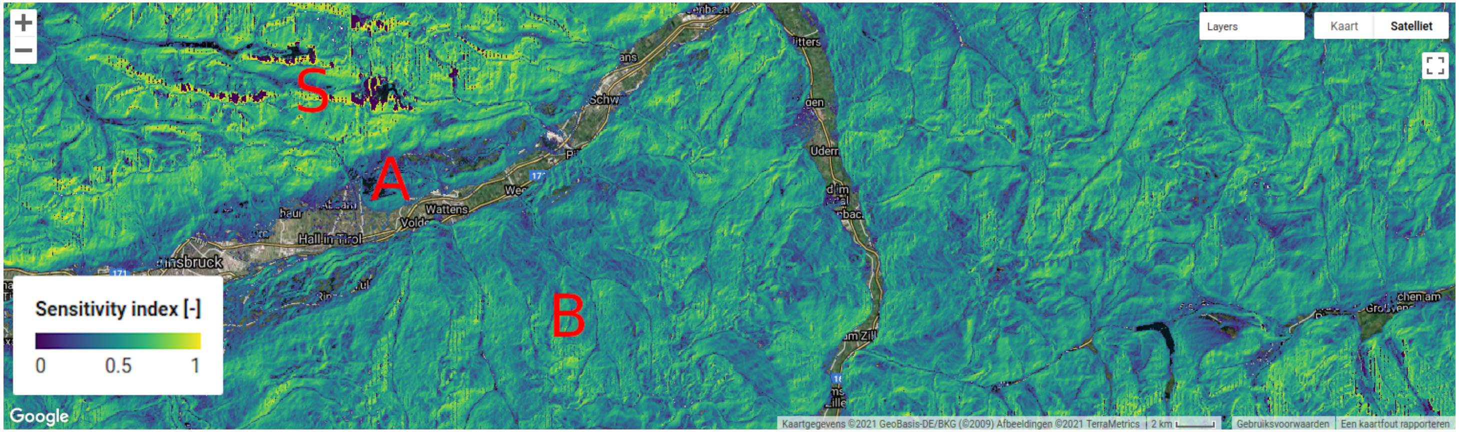

Figure 3.11: Example of the sensitivity index, as generated in Google Earth Engine, for part of the Inn valley, around Innsbruck and Wattens, Tirol, Austria. The valley is flat, at a slope of less than 5°, and reveals the underlying map. Small patches in the north-west, marked ‘S’ in the image, are shown as dark blue, indicating no sensitivity to deformation due to either shadow, layover or a combination of both. The south-east facing slopes on the northern side of the Inn valley, ‘A’, suffer from poor sensitivity. Therefore, only strong displacement signals will be detectable here, if at all. Side valleys in the south-east, of the image, at ‘B’, show more gradual topography and typically high sensitivity. As the highest sensitivity index value of either the ascending or descending orbit is reported, both east and west facing slopes are marked visible in this image. Note that the sensitivity index is higher on slopes facing north than on south-facing slopes. (Map: Google Earth Engine)

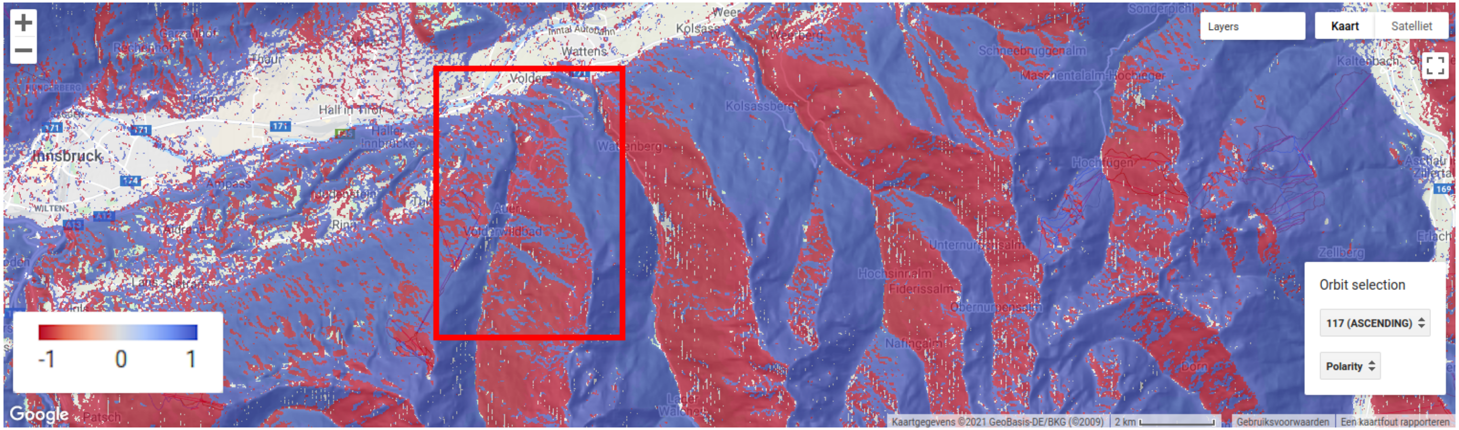

Orbit selection: 117 (ASCENDING)

Figure 3.12: Example of polarity product in Google Earth Engine. The area, marked by the red rectangle, is the Großvolderberg, near Innsbruck, Tirol, Austria. This slope shows how, even in a small area, downslope deformation will be represented by a mix of lengthening (+1) and shortening (−1) in the InSAR data. Prior knowledge of the polarity will aid the interpretation of the InSAR signal, that may appear noisy due to frequent sign changes within slopes. (Map: Google Earth Engine)

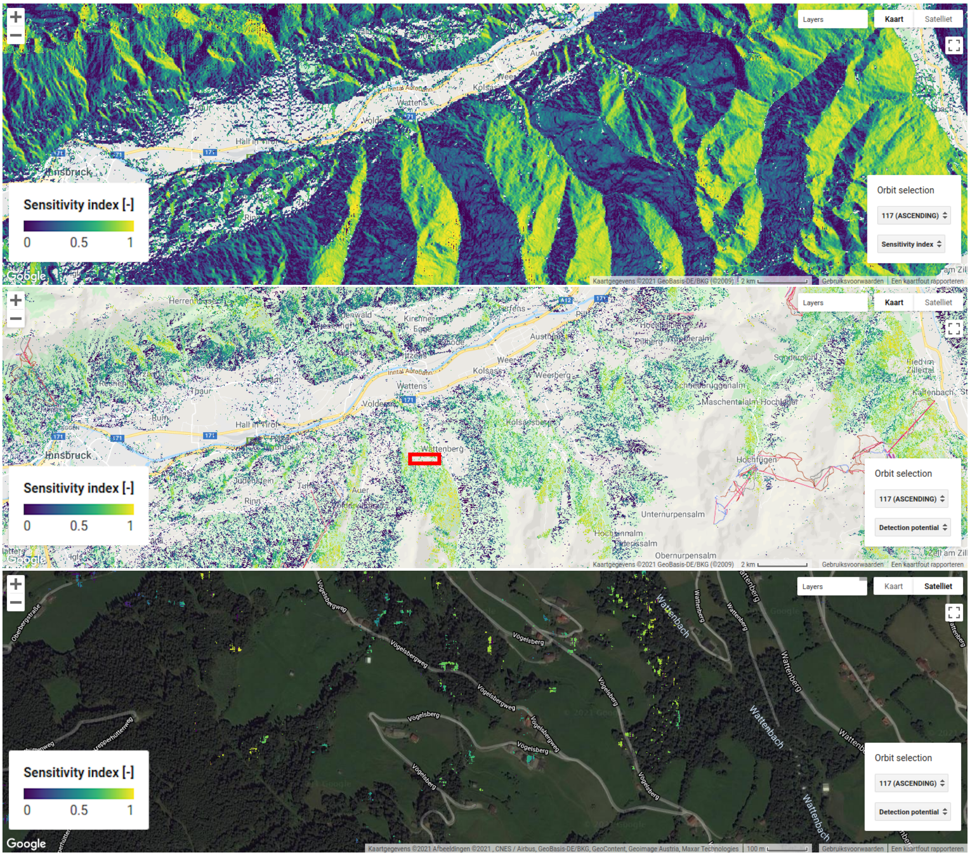

Orbit selection
117 (ASCENDING)
Sensitivity index

Orbit selection
117 (ASCENDING)
Detection potential

Orbit selection
117 (ASCENDING)
Detection potential

Figure 3.13: Three maps over the Inn valley, as generated by our Google Earth Engine tool. Coverage for the top two images is identical to Fig. 3.11: the Inn valley around Innsbruck and Wattens, Tirol, Austria. Top: the sensitivity index, with the radar geometry specific for ascending orbit 117 of Sentinel-1. Very few areas are invisible to the radar (dark blue). Flat areas, such as the Inn valley, where the slope is less than 5°, are transparent and show the underlying map. Center: The sensitivity index, masked by the detection potential, shows the sensitivity where the normalized amplitude dispersion is not greater than 0.4. Except for the high mountain ridges, the lower part of the slopes show patches of potential coherent scatterers, and are more likely to have a successful application of InSAR. Bottom: An excerpt of the previous map, marked by the red rectangle. This map shows the sensitivity index, again masked by the detection potential: a normalized amplitude dispersion not greater than 0.4. The map shows a high likelihood of finding coherent scatterers on/around the houses, while for fields an actual InSAR data processing procedure would be required to assess the actual coherence level. Forest pixels are unlikely candidates, but have a sufficiently low normalized amplitude dispersion due to their consistent, low amplitude. (Map: Google Earth Engine)

Furthermore, at slope level, the detection potential indicator can be used to highlight the sensitivity index for potential coherent scatterers.

The Vögelsberg slope, near Innsbruck, Austria, is affected by a deep-seated landslide (Zieher et al., 2019; Pfeiffer et al., 2021). The steep valley shape as well as the various orientations of the surrounding slopes make it a complex setting for the application of InSAR analysis. Fig. 3.12, for example, shows the spatial variability in the effect of downslope displacement on the line-of-sight range. Fig. 3.13 shows the sensitivity index, and detection potential indicator for the region around the slope, as well as the detection potential indicator on the slope scale. Contrary to Fig. 3.11, that showed the lower bound of the sensitivity index, the sensitivity index in Fig. 3.13 is calculated based on the specific orbit parameters.

Using the Google Earth Engine tool, the user may explore the properties of the different orbits available. On the Vögelsberg landslide, where ground truth velocity estimates are available, not only the sign, but also the approximate magnitude of the average line-of-sight velocity is available via the sensitivity index (Eq. 3.15). The various layers show not only the sensitivity index, but also the number of images available in each time frame and orbit. Especially with some prior knowledge of the landslide deformation pattern, the orbit with suitable coverage of the expected displacement can be found.

The Google Earth Engine tool is available on:
`https://avannatijne.users.earthengine.app/view/landslide-insar`[2].

3.5 Results of the global sensitivity index

A statistical analysis of the global sensitivity index is shown in Fig. 3.14. These numbers are aggregated statistics of all slopes in the Copernicus DEM, corrected for the reduced DEM-pixel size towards the poles. Notti et al. (2014) suggested that, as rule of thumb, landslides with a sensitivity index greater than 0.2 allow for deformation monitoring by InSAR. Based on this threshold, the global sensitivity index shows that displacement of at least 91% of the world's slopes would be observable by InSAR. If only a single orbit is available at a given location, either ascending or descending, 64% of the slopes is within this criterion. Our results for the individual orbit directions are in line with Novellino et al. (2017), who concluded that 67.2% of Great-Britain could be observed in an ascending orbit and 67.5% in a descending orbit.

3.6 Discussion

Various assumptions underpin our proposed methodology, allowing us to evaluate the sensitivity index globally and integrate the detection potential in Google Earth Engine as products that do not require expert knowledge and experience to operate.

---

[2] `https://avannatijne.users.earthengine.app/view/landslide-insar`

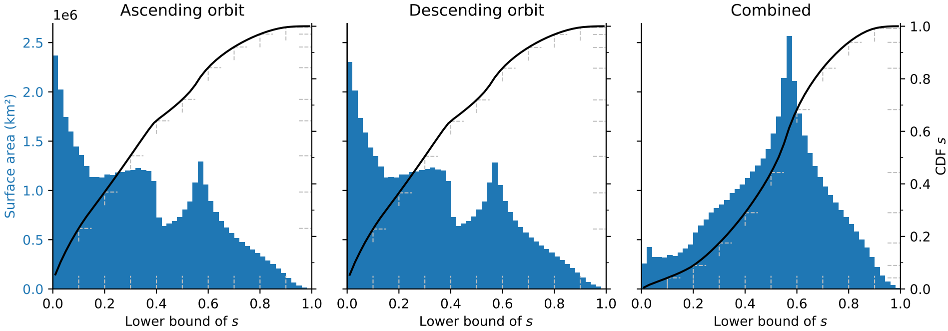

Figure 3.14: Histograms of computed global sensitivity index values, for both ascending and descending orbits, as well as the highest sensitivity index from either orbit. Included are all slopes mapped by the Copernicus DEM, steeper than 5°. Areas invisible due to layover or shadow are marked as 0 sensitivity. The cumulative distribution function of the absolute value of the lower bound of sensitivity, is given in black.

Landslide behaviour In the absence of information on the landslide type, in this study, a principal assumption is that landslides undergo downslope displacement only (Bianchini et al., 2013; Singleton et al., 2014). Although most landslide types undergo at least some form of downslope deformation, different parts of the landslide may move in different directions, such as uplift at the toe of a rotational landslide, or thinning at the scar of translational slides (Frattini et al., 2018). Schlögel et al. (2015) even suggest that vertical deformation signals, due to subsidence at the scarp and accumulation at the toe, are stronger than downslope deformation. Furthermore, basal sliding will follow the slope of the slip surface rather than the surface topography (Massey et al., 2013). If the landslide type is known, and a specific deformation pattern is expected, the sensitivity index can be adapted to include deformation in any direction (e.g. in case of subsidence: $\mathbf{r} = \begin{bmatrix} 0 & 0 & -1 \end{bmatrix}^{\mathrm{T}}$).

Radar geometry Thanks to the Copernicus program, there is and will be an abundant availability of Sentinel-1 imagery. Therefore, the focus of this paper is on Sentinel-1 data. However, there is no full coverage of the Earth with both ascending and descending orbits (Copernicus, 2019). As a consequence, the global sensitivity index may overestimate the sensitivity index in areas covered by only a single orbital direction.

The methodology could just as well be applied to any other satellite or satellite constellation. This method is already effective with knowledge of only three to four acquisition parameters: extremes of the incidence angle: $\theta_{\min}$, $\theta_{\max}$; satellite orbit parameters: inclination i and mean motion κ in revolutions per day. For TerraSAR-X, for example: $\theta_{\min} = 20°$, $\theta_{\max} = 45°$, $i = 97.44°$ and $\kappa = 15.1914$ (Airbus, 2015).

Time series All images are assumed to be usable for time series analysis. In practice, images might be missing or unusable due to anomalies (e.g. long baselines) or seasonal effects (e.g. snow cover). Long periods without observation may trigger unwrapping errors as well as increase the minimum significant detectable landslide velocity. Furthermore, significant changes in scattering characteristics will spoil the coherence of the scatterers fundamental to InSAR. Snow and flooding alter scattering characteristics temporarily and potentially permanently, leading to the loss of the time series.

The maximum landslide deformation resolvable from interferometric phase differences is limited by the wavelength as well as the gradient between neighbouring observations in space and time. Under ideal circumstances, without noise, this so-called unwrapping limit for independent observations is a quarter of the wavelength λ of the radar system: $\pm\frac{\lambda}{4}$. However, this assumption is too rigorous. First, especially on slopes with a low sensitivity s, the effective limit on deformation will be much larger: $\pm\frac{\lambda}{4s}$. Second, neighbouring observations on the landslide, that underwent less deformation since the last acquisition, may provide a spatial gradient of resolvable differences. Finally, under the assumption of downslope deformation only, the unwrapping limit may be expanded to half the wavelength: $\frac{\lambda}{2s}$.

3.7 Conclusions

Analysis of our global sensitivity index indicated that at least 91% of the global slopes are likely to allow for InSAR deformation monitoring with Sentinel-1. The Google Earth Engine tool provides an initial, local analysis of the available radar imagery, and highlights areas with potentially favourable scattering characteristics. Together, the sensitivity index and detection potential indicator provide an a priori indicator of the likelihood of success of InSAR campaigns. Therefore, they are valuable tools in the planning phase of an InSAR campaign, where the Google Earth Engine tool accelerates the initial site survey and orbit selection process, while the global sensitivity index extends landslide inventories, hazard or susceptibility maps with an indication of the InSAR monitoring potential. The methodology presented is easily extended to other satellite constellations and/or deformation patterns.

The global sensitivity index is available for download via doi:10.4121/14095777[3] (van Natijne et al., 2022b), the Google Earth Engine tool is available on `https://avannatijne.users.earthengine.app/view/landslide-insar`[4]. Underlying code is available with their products.

---

[3] `https://doi.org/10.4121/14095777`

[4] `https://avannatijne.users.earthengine.app/view/landslide-insar`

Chapter 4

Nowcasting of the Vögelsberg deep-seated landslide

Submitted to Natural Hazards and Earth System Sciences (European Geosciences Union/Copernicus Publishers) as: van Natijne, A. L., Bogaard, T. A., Zieher, T., Pfeiffer, J., Lindenbergh, R. C., 2022c. Machine learning nowcasting of the Vögelsberg deep-seated landslide: why predicting slow deformation is not so easy. `https://egusphere.copernicus.org/preprints/2022/egusphere-2022-950/`, accessed on 2022-10-04.

Abstract

Landslides are one of the major weather related geohazards. To assess their potential impact and design mitigation solutions, a detailed understanding of the slope processes is required. Landslide modelling is typically based on data-rich geomechanical models. Recently, machine learning has shown promising results in modelling a variety of processes. Furthermore, slope conditions are now also monitored from space, in wide-area repeat surveys from satellites. In the present study we tested if use of machine learning, combined with readily-available remote sensing data, allows us to build a deformation nowcasting model. A successful landslide deformation nowcast, based on remote sensing data and machine learning, would demonstrate effective understanding of the slope processes, even in the absence of physical modelling. We tested our methodology on the Vögelsberg, a deep-seated landslide near Innsbruck, Austria. Our results show that the formulation of such a machine learning system is not as straightforward as often hoped for. The primary issue is the freedom of the model compared to the number of acceleration events in the time series available for training, as well as inherent limitations of the standard quality metrics such as the mean squared error. Satellite remote sensing has the potential to provide longer time series, over wide areas. However, although longer

time series of deformation and slope conditions are clearly beneficial for machine learning based analyses, the present study shows the importance of the training data quality but also that this technique is mostly applicable to the well-monitored, more dynamic deforming landslides.

4.1 Introduction

Landslides make up for 6% of the weather related disasters globally (WMO, 2019). To protect the public, landslides have been a major research topic for the last decades. For local landslide mitigation by geotechnical intervention an up-to-date understanding of these hydro-meteorological phenomena, their feedbacks and impact is desired. This understanding may then be leveraged for the design of landslide hazard mitigation measures.

Where the installation of effective remediation concepts is not possible, early warning systems may help to reduce the landslide risk. Such systems should quickly adapt to changing conditions, both on the slope and global (e.g. climate change). Moreover, such a system should be fast to adapt and implement to assess as many slopes as possible.

Existing local systems typically provide early warning based on in-situ slope monitoring (Guzzetti et al., 2020). An example of a satellite based, global early warning system is the LHASA model (Kirschbaum and Stanley, 2018; Hartke et al., 2020; Stanley et al., 2021) that provides a global nowcast of acute landslide susceptibility. However, these systems typically focus on sudden, fast, and shallow landslides. Such catastrophic events change the landscape, and as a consequence the situation before and after the collapse are no longer comparable. Therefore, the landslide process preceding the collapse can only be studied if data from before the landslide is available.

We focus on slow moving, reactivating, deep-seated landslides on natural slopes, for which the deformation pattern is controlled by hydro-meteorological forcing. These deep-seated landslides are estimated to comprise 50% of the landslides globally (Herrera et al., 2018; Novellino et al., 2021). The deep-seated landslides we focus on rarely evolve into catastrophic collapse and often entail a complex response to hydro-meteorological conditions controlling the landslide's pore pressure (Bogaard and Greco, 2015). They are characterised by gradual, non-catastrophic deformations that can be responsible for extensive infrastructure damage (Mansour et al., 2011). Deformation rates typically vary from millimeters to decimeters per year, whereas phases of acceleration or deceleration often correlate with time-delayed hydrological conditions (Intrieri et al., 2018).

Monitoring systems only supported by the detection of currently emerging acceleration events (e.g. Carlà et al., 2017), can only be used to detect already ongoing acceleration. As a consequence, adequate early warning is only possible if the deformation can accurately be predicted beforehand. Therefore, the deformation should be predicted from the predisposing conditions on the slope, combined with dynamic factors such as infiltrating precipitation and snowmelt that lead to higher pore pressures, instability and subsequent deformation. However, the deformation behaviour of such slow, deep-seated landslides is 'extremely difficult' to model (Van Asch et al., 2007).

Past landslide deformation events are indicative of the future behaviour, as landslides are likely to display similar behaviour in similar situations (Fell et al., 2008; Guzzetti et al., 1999). Unlike catastrophic landslides, where the landslide dynamics change permanently, slow moving landslides are not single, catastrophic incidents. Therefore, analysis of the monitoring data of deep-seated landslides is expected to reveal causal factors in landslide deformation, which allow for a continuous cycle of forecast and validation of the relationship between deformation and the conditions on the slope.

Deformation nowcasting could be considered an intermediate option between monitoring and modelling, integrating sensor data to estimate the current situation (the system state) and extrapolate on a short timescale. New data and data integration methods, 'machine learning', offer new possibilities for such data-driven landslide forecasting (van Natijne et al., 2020). Furthermore, these techniques offer new capabilities to continuously track the system state without extensive, in-situ sensor networks and physics-based modeling. Such data-driven models could be used to 'learn' the landslide dynamics and the interplay of hydro-meteorological factors from the deformation signal of the landslide.

In the last decades satellite observations have increased in quantity, shortening the time between subsequent acquisitions, as well as increasing the variables observed (Belward and Skøien, 2015). These acquisitions provide us with a global overview of the status of the earth at local scale, often with weekly to daily updates. More recently there is the tendency to make the data freely available, a development that lowered the barrier for innovations (Zhu et al., 2019), and especially benefits experiments that require long time series, like this study. Even though their coverage is often limited to the surface, the repeated monitoring of the slope conditions may reveal the slope processes responsible for accelerated deformation (van Natijne et al., 2020).

Here we present a data-driven nowcasting model with a four day lead time of the deformation of the Vögelsberg landslide, near Innsbruck, Austria. We use readily available, remotely sensed data and products, and test various similar remote sensing products to assess their relative performance in the nowcasting model. We discuss the complications encountered during modelling: over-parametrization, the impact of optimization metrics, and the challenges due to the deep-seated landslide inertia compared to the highly dynamic forcing of the slope.

First, we introduce the modelling options, and study area. Second, we present the resources available to us, and our modelling approach, followed by the results and an extensive discussion on the insights gained during the modelling exercise. Last, we provide recommendations for future data-driven landslide nowcasting exercises.

4.2 Data-driven modelling approaches

In the present study we interpret data-driven modeling as a form of naive modelling. That is, the model is unaware of the physics behind the landslide process. For data-driven models, the deformation of the slope is merely a signal to be reproduced from a collection of observations by empirical relations, in contrast to traditional, landslide geomechanical modelling, that is rooted in physics. Table 4.3 features a selection of studies into data-driven deep-seated landslide nowcasting, demonstrating the recent interest in this topic. Various examples come from landslides around the Three Gorges Dam that are strongly controlled by the reservoir water level. However, this is not the most common type of deep-seated landslide. Deep-seated landslide deformation is typically driven by the water storage in the deeper subsurface, that is controlled by a long-term water balance of precipitation and snowmelt input, evaporation losses, and regional groundwater input and drainage (Bogaard and Greco, 2015).

The indirect transfer from precipitation and snowmelt to storage may be captured by, for example, including recent observations in a bucket model (Nie et al., 2017). A bucket model represents the subsoil as a storage that is replenished by precipitation and emptied by drainage and evaporation. Furthermore, changes to the storage may involve a time delay, depending on complex infiltration processes. This process may be dependent on the precipitation type, duration and intensity. Moreover, deformation may not be governed by a short and single precipitation event. For example, a short, extreme precipitation event or three days of consecutive drizzle may introduce similar amounts of water to the system, but will be represented differently in storage changes due to different infiltration abilities of the soil. All in all, modelling of deep-seated landslides will likely require some form of storage modelling, where these dynamics are either resolved by the model or in advance by an expert.

Two distinct modelling approaches can be distinguished. Modelling is either based on classification of the environmental conditions and associated deformation response, or calculates the expected deformation response from the conditions on the slope. In either case the model parameters are tuned on historic observations such that they best reproduce the deformation signal from the conditions observed previously at the slope. Our model of the Vögelsberg landslide is a continuous model. For completeness classification models will be introduced briefly.

4.2.1 Classification models

Based on the assumption that similar conditions trigger a comparable deformation response (Fell et al., 2008; Guzzetti et al., 1999), conditions and responses may be categorized. The current slope conditions are then matched against historic conditions, and the deformation response is assumed to be the same. Extrapolation of the response to previously unencountered conditions is typically impossible with these models. However, the system will therefore also not yield unrealistic results, and could be considered bound to the previously encountered deformation signal.

4.2.2 Continuous models

The simplest, linear, model is the weighted sum of the quantified conditions at the slope. However, the slope response may not be linear and is typically not immediate. Neural networks make may be used to estimate any signal by the formation of a network of interlinked nodes that ingest and combine the conditions on the slope in subsequent layers of nodes (Hornik et al., 1989; Hill et al., 1994). A time series passed to a single input neuron is equal to a weighted sum of the time series, plus a bias.

As more hidden layers of neurons are introduced to the system, the direct link to the (time series) input is lost, as combinations are made. Furthermore, an activation function may be applied to scale the output of each node, especially to normalize the response and filter outliers, at the cost of introducing non-linearity to the system. The number of parameters, degrees of freedom of the model, are associated with the number of input variables. When historic observations are supplied as additional observations, they will each require their own model parameters, and increase the degrees of freedom in the model.

State aware models, such as Recurrent Neural Networks (Connor et al., 1994), maintain a track record of the state of the landslide instead, and iterate over the input time series in successive model runs. Individual observations are fed into the system, with the system maintaining track of their contribution to the current state of the landslide. These models resemble a bucket model, a simplified representation of the water storage in the subsoil. However, unlike in a traditional (soil moisture/ground water) bucket model, all variables are taken into account, even if they do not directly represent water. Furthermore, unlike regular neural networks, the number of trainable parameters is not dependent on the length of the history supplied to the model, but on the number of memory cells and time series.

Models based on Recurrent Neural Networks suffer from computational difficulties during optimisation, where gradients may vanish (Bengio et al., 1994; Hochreiter and Schmidhuber, 1997; Hochreiter, 1998). Therefore, they are typically replaced by models based on Long Short-Term Memory (LSTM) nodes (Hochreiter and Schmidhuber, 1997), that do not suffer from this due to built-in normalisation. Each LSTM 'bucket' is capable of weighting, retaining and clearing a memory of previous inputs, and as such tracks the system state.

The challenge specific to forecasting and nowcasting is the absence of information on the future slope conditions. The latest information available to the system are the current conditions and the last estimation of the system state. Auto-regressive models predict these conditions as well, so that subsequent forecasts may use these environmental conditions in their models. However, especially precipitation is governed by external influences and may not be predictable from the other forcing parameters in the system. As an alternative, forecasts may be included into the model. However, this would require forecasts for all input variables. Therefore, such system was deemed not suitable for this application.

Special attention should be paid to the robustness of the model. Even ten years of daily observations will result a time series of less than 4 000 reference observations, much less than desirable for use in more complex machine learning models such as neural networks (Cerqueira et al., 2019). If too few training data are provided, the abundance of input data creates unique combinations of conditions and outputs. This will lead to excellent performance during training, but reduced performance during testing and application, and is known as over-fitting.

There are infinite data-driven modelling possibilities and the generic character of many data-driven models suits the diversity in available remote sensing variables. However, due to the limited length of the time series, in comparison to typical machine learning studies, one should stay close to the physics and processes, to limit the freedom of the model towards a solution. Therefore, one has to ensure a balance between the number of parameters to be estimated and the training/validation data available.

4.3 Case study: the Vögelsberg landslide

The Vögelsberg is a deep-seated landslide, located in the Wattens basin, near Innsbruck, Austria (Figure 4.1). Its north-east facing slope covers approximately 4.6 km^2, and ranges between 750 m and 2200 m above sea level. A nearby weather station reports an average yearly precipitation of 896 mm, of which 13% is in the form of snow. The lower, active part of the landslide is only about 0.2 km^2 and is covered by pasture fields, sparse forests and few houses and farm buildings. The shearzone was identified via inclinometer measurements to be at 43–51 m below the surface, although strongly disintegrated soil up to 52–70 m indicates a long history of activity (Pfeiffer et al., 2021).

In 2016 a Leica TC1800 Automated Total Station (ATS) was installed in Wattenberg, opposite to Vögelsberg, by the Division of Geoinformation of the Federal State of Tyrol. The system surveyed each of the fifty-three benchmarks every hour. Extensive corrections to the measurements were necessary, primarily due to the instability of the monument the total station is located on. In this study a series of pre-processed range measurements was used, fixed to stable benchmarks around the active area that showed no signs of landslide deformation damage. The accuracy of this time series was estimated to be in the order of ±0.54 cm/a (Pfeiffer et al., 2021). The time series of the displacement rate at the two benchmarks used in this study are shown in Figure 4.2, their locations are indicated in Figure 4.1. Time series of the other benchmarks are shown in Pfeiffer et al. (2021, Figure 3).

The deformation of the Vögelsberg landslide is a complex response to the hydro-meteorological conditions in the catchment, in particular precipitation and (delayed) infiltration from snowmelt. A binary prediction of stability/instability or acceleration/deceleration is insufficient for the Vögelsberg landslide, as the slope is undergoing continuous deformation. Pfeiffer et al. (2021) conducted a full assessment of the hydro-meteorological drivers and found a 20–60 day time lag between rainfall and

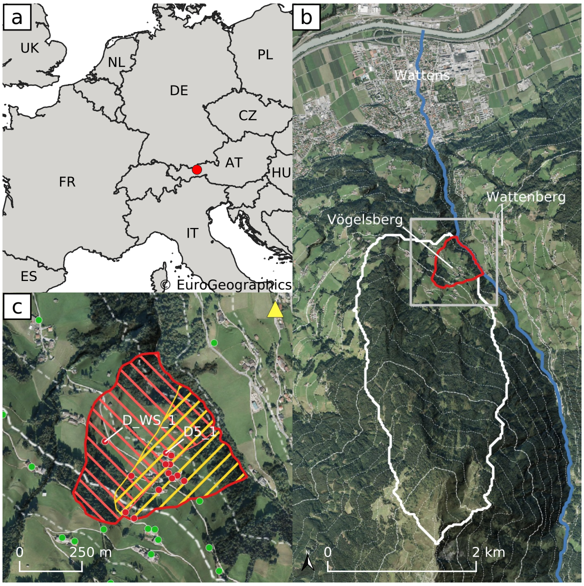

Figure 4.1: a) Location of Vögelsberg in Europe. b) Overview of the landslide catchment (white) and active region of the Vögelsberg landslide (red). Dashed contour lines are shown every 100 meters of elevation change. The coverage of sub-figure c is indicated in gray. c) Detail of the active region of the Vögelsberg landslide. The northern subsection of the slope (red) and southern (yellow) section and overlapping area are marked. Out of a total 53 retroreflecting prisms, the 29 benchmarks with the longest time series (2016–2020) are shown. Benchmarks on the landslide are shown in red, stable, reference benchmarks in green. The time series of benchmarks 'D_WS_1' and 'D5_1' are shown in Figure 4.2. The location of the total station in Wattenberg is marked by a yellow triangle. (Backgrounds: Eurostat/EuroGeoGraphics; Federal State of Tyrol, Austria)

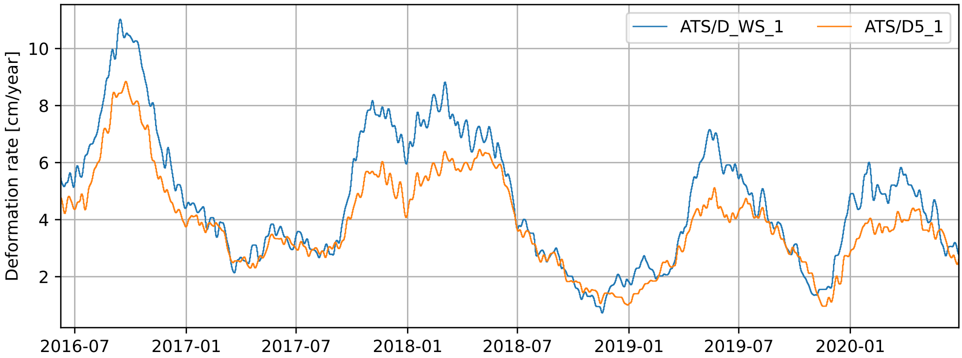

Figure 4.2: Daily deformation rate of the Vögelsberg landslide at benchmarks ‘D5_1’ and ‘D_WS_1’ (Figure 4.1), as measured by the automated total station and smoothed by a moving average filter over the last 32-days.

acceleration and a 0–8 day time lag between snowmelt and acceleration. Noteworthy is the difference in behaviour between the northern and southern sections of the slope, represented by benchmarks ‘D_WS_1’ and ‘D5_1’ respectively (Figure 4.2). The northern section of the slope (‘D_WS_1’) shows a higher variability in the deformation signal, with stronger accelerations than the southern, inhabited section of the slope (‘D5_1’). We focus on these two benchmarks, as a balanced representation of the two landslide sub-systems.

The deformation rate, derived from the total station range measurements, was smoothed by a moving average filter until few, noise induced, negative (up-slope) deformations remained, while maintaining the highest possible temporal resolution (Figure 4.14). Only historic observations may be used in an operational early warning system, and a moving average of the most recent 32 days was necessary to remove most of the noise. As a consequence, the onset of acceleration will be only 1/32 of the signal and thus severely dampened, stressing the need for an acceleration prediction rather than extrapolation of deformation measurements as warning signal. Moreover, signals shorter than the filter length will be reduced in amplitude.

4.4 Methodology

Our model’s aim is to predict the landslide deformation based solely on the current conditions at the slope. No recent deformation observations or prior defined geomechanical model will be available to our model during prediction. The main model constraints are that we have a relatively limited amount of data points (1 482 samples) and will work with readily available remote sensing data and products. Furthermore, we set the objective to model with daily time steps and a forecast lead time of four days. A successful prediction of the deformation rate four days ahead will demonstrate the model’s ability to predict a tipping point based on the environmental conditions (acceleration, peak, deceleration). Moreover, a four day prediction would give sufficient time for further investigation as part of an early warning system.

With these constraints in mind, a system was designed based on a parsimonious recurrent neural network. First, we will introduce the data available. Second, an overview is provided of the pre-processing applied to the input variables. Third, we provide the specifications of our model. Last, the training and validation of the model are discussed.

4.4.1 Model variables

The model variable selection is based on the analysis of factors of influence (Pfeiffer et al., 2021), and are mainly of data-driven nature. Pre-disposing or causal factors, such as topography, that are necessary for a landslide to form, are considered static in this study. Therefore, the focus is on the dynamic conditions leading up to landslide instability and deformation, and triggering factors. The selection of variables is listed in Table 4.1.

Our method is designed with the intent to be generally applicable. Therefore, where possible, remote sensing products were used, as they are likely to be available elsewhere as well. Where available, redundant products, that represent the same or similar quantities, were included to assess their relative performance in the nowcasting model. The correlation between the products is limited ($\mu_{|\rho|} = 0.16$, $\max|\rho| = 0.7$, Figure 4.13), indicating differences between the products of the same quantity. Effects that may not be observed directly, such as soil moisture under snow, require some form of modelling or re-analysis. These quantities, not directly available from remote sensing, are taken from re-analysis models 'ECMWF Re-Analysis, version 5' (ERA5) and the 'Global Land Evaporation Amsterdam Model' (GLEAM).

The desired output of our model is a daily, four days ahead prediction of the landslide deformation rate at benchmarks 'D_WS_1' and 'D5_1'. Reference, training and validation samples are provided by the automated total station located on the Wattenberg, opposite to Vögelsberg (Figure 4.1). Deformation measurements were performed hourly from 2016-05-04 to 2020-06-28, and aggregated to 1 482 daily averages to reduce noise. The noise in the signal was further reduced by a 32-day moving average filter, of which the results are shown in Figure 4.2. The time series at the 51 other benchmarks (Figure 4.1) were not used in the modelling.

Daily precipitation information is provided by the Integrated Multi-satellitE Retrievals for GPM (IMERG) algorithm of the Global Precipitation Measurement mission (GPM) (NASA, 2018). 'Early' results are provided with sub-day delay, and are therefore especially suitable for an operational nowcasting model. For comparison daily precipitation from the ECMWF ERA5 Land re-analysis is included as well (ERA5, 2019). Snow properties are covered by two products of the ERA5 Land re-analysis: snow water equivalent, and snowmelt.

Soil moisture, especially at depth, cannot be observed directly from space at a

Table 4.1: Selection of time series considered for integration into the model. Deformation variables are marked ‘D’, while slope conditions, input variables to the model, are marked ‘V’. Observations are marked ‘S’ for directly observed variables processed and available within the time frame of a nowcasting system; ‘R’ for re-analysis variables, and ‘M’ for variables modelled within this study (see §4.4.2). References to the various sources are provided in the main text. The internal identification is derived from the variable as referenced by the source, and is used throughout the figures to refer to the various time series. From rasterized products, only the time series closest to Vögelsberg was used.

	Variable	Source	Type	Spatial res.	Temp. res.	Int. identification
D1	Deformation ‘D_WS_1’	ATS (local)	S	point	daily	`ATS/D_WS_1`
D2	Deformation ‘D5_1’	ATS (local)	S	point	daily	`ATS/D5_1`
V1	Precipitation	ERA5	R	0.1° (≃ 10 km)	hourly	`ERA5/tp`
V2	Precipitation	GPM	S	0.1° (≃ 10 km)	30 min.	`GPM/precipitationCal`
V3	Snow water equivalent	ERA5	R	0.1° (≃ 10 km)	hourly	`ERA5/swe`
V4	Snowmelt	ERA5	R	0.1° (≃ 10 km)	hourly	`ERA5/smlt`
V5	Soil moisture, full profile	SMAP	R	0.1° (≃ 10 km)	3 hrs.	`SMAP/sm_profile`
V6	Soil moisture, root zone	GLEAM	R	0.25°(≃ 25 km)	daily	`GLEAM/SMroot`
V7	Soil moisture, 100–289 cm	ERA5	R	0.1° (≃ 10 km)	hourly	`ERA5/swvl4`
V8	Evaporation	GLEAM	R	0.25°(≃ 25 km)	daily	`GLEAM/E`
V9	Air temperature	ERA5	R	0.1° (≃ 10 km)	hourly	`ERA5/t2m`
V10	API		M	point	daily	`API/API`
V11	Sesonal noise		M	point	daily	`fake/fake`

high enough resolution for this application. The low latency, operational products from the Copernicus Land Service, Soil Water Index and Surface Soil Moisture, are frequently unavailable either due to unfavourable slope topography or due to snow cover. Alternatives are provided by SMAP L4 (Entekhabi et al., 2010; Reichle et al., 2022); 'Global Land Evaporation Amsterdam Model' (GLEAM) (Martens et al., 2017; Miralles et al., 2011); and ERA5 Land (ERA5, 2019). Evaporation estimates are taken from GLEAM as well. Air temperature, a proxy indicator of evaporation and snowmelt, is included from ERA5 Land (ERA5, 2019).

4.4.2 Variable preparation

The model is fed with the eleven variables defined in §4.4.1 (Table 4.1). Except for the deformation time series, all sources consist of gridded products, with wide area coverage. In this study only the data point closest to the active part of the Vögelsberg landslide was used. To match the time resolution of the deformation measurements the model is run at daily intervals. Observations available at shorter intervals are aggregated to daily means first. Where data is missing, for example due to sensor failure, the values are filled with the data from the previous day (forward filling), as would be possible in an operational scenario. Furthermore, two modelled time series were added to the system: an antecedent precipitation index (API) as basic hydrological model and a random, seasonal noise signal.

The Antecedent Precipitation Index (API, `API/API`, V10) was designed to estimate the water present in the watershed (Kohler and Linsley, 1951; Heggen, 2001). The API is included to determine if such variable could support the deformation nowcasting model. Precipitation less than 0.1 mm was ignored, in addition a 10% direct evaporation loss, and a 4% daily storage loss is assumed. These parameters were chosen based on an expert's estimate of the hydrological setting. The API at time step t is calculated as

$$\mathrm{API}_t = \max(0, p - 0.1) \cdot 0.9 + 0.96 \cdot \mathrm{API}_{t-1}, \tag{4.1}$$

with p the daily precipitation sum. The API, calculated from the operational GPM precipitation data (`GPM/precipitationCal`), is shown in Figure 4.3.

A random variable with seasonal characteristics is added to the variable selection to analyze the effect of spurious correlation on the model. The random variable, `fake/fake` (V11), based on Brownian motion, is tuned to match a typical seasonal characteristic in the 32-day history relevant to the model. The auto-correlation behaviour is illustrated in Figure 4.4, and resembles the dynamics of both the surface temperature as provided by ERA5 and the soil moisture from SMAP for the first 2–3 months. Longer correlation periods are not relevant for our model.

All variables are offset to become zero-mean and scaled by the standard deviation. Therefore, all input variables are on approximately equal scale and represented as deviations from their average condition. The normalization parameters, mean and standard deviation, should be kept fixed while new data is added, to remain consistent with the scaling of the time series used during training. The data set is

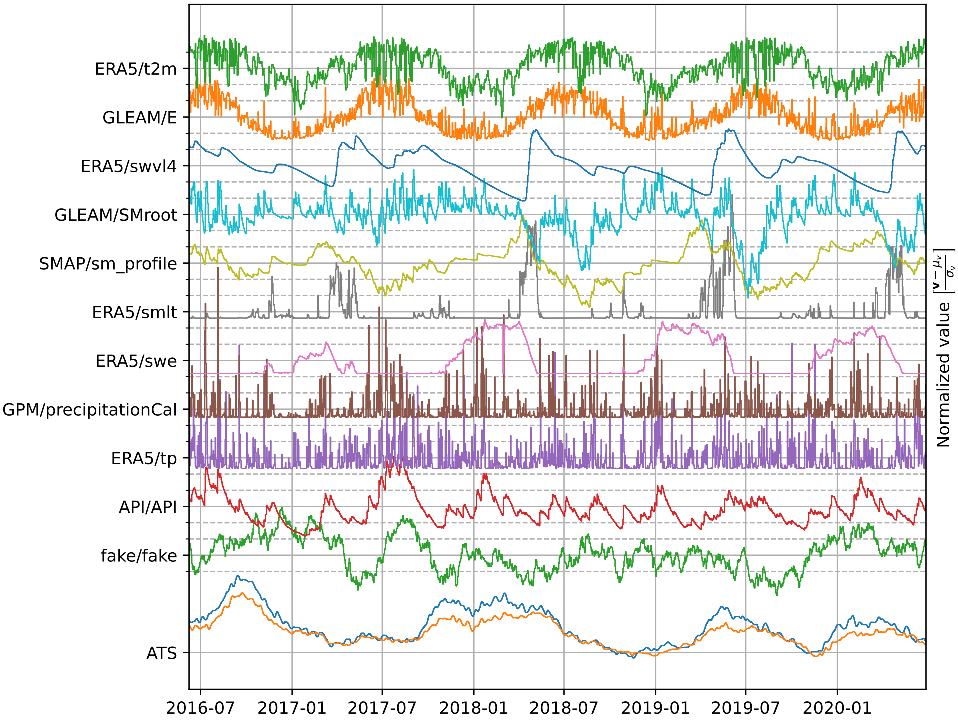

Figure 4.3: Overview of the variable space (Table 4.1). The values are offset to a zero mean and scaled by their standard deviation. A single iteration of the seasonal noise (`fake/fake`) is shown as an example.

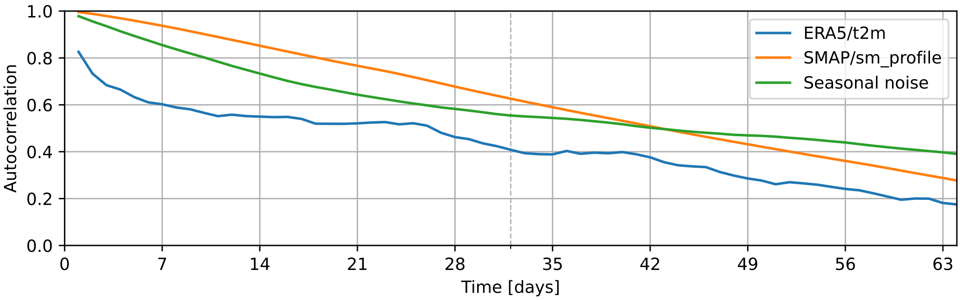

Figure 4.4: Autocorrelation of one of the generated signals compared to the autocorrelation of the temperature as taken from ERA5 (`ERA5/t2m`) and the soil moisture estimate from SMAP (`SMAP/sm_profile`). The length of the history as used by the model, 32 days, is indicated by the dashed line.

fed to the model as a time stamped collection of daily observations, illustrated in Figure 4.3.

4.4.3 Model configuration

Our model is a shallow neural network with only a single hidden layer (Jain et al., 1996). This hidden layer consists of a single Long Short-Term Memory (LSTM) node (Hochreiter and Schmidhuber, 1997), that resembles a bucket model for the water storage in the subsoil. The model is supplied with a thirty-two day history of observations, equal to the length of the moving average filter, longer than the lag time for snow (0–8 days) and sufficient to cover most of the 20–60 day lag time for rainfall at the Vögelsberg landslide found by Pfeiffer et al. (2021). From a pre-defined, optimized initialisation, the model is cycled for each day of preceding observations, feeding the observations into memory, before a prediction is made based on the final bucket values ($\mathbf{m}$). The model is illustrated in Figure 4.5, as function of environmental conditions ($\mathbf{x}$, Table 4.1), at each of the $n = 32$ days preceding the nowcast, the LSTM node and four neurons of a single benchmark, one for each prediction day. This last, output, layer is repeated for both benchmarks ('D_WS_1' and 'D5_1') to be predicted, while the LSTM memory ($\mathbf{m}$) is shared between the benchmarks to reduce the number of parameters.

In total, for a network configuration with a single memory cell ($\mathbf{m}$), 68 parameters have to be estimated. The LSTM node, with one hidden state, requires 52 parameters to be estimated for the eleven variables (Table 4.1). Sixteen parameters are required for the output, eight for each of the deformation time series: one bias and one scaling parameter per day for the final state of the LSTM node. The number of parameters to be estimated is independent of the history length.

Four parameters are added per extra prediction day (two benchmarks, one bias and weight each). An extra memory cell requires $8h + 4x + 1$ extra parameters, with h the current number of hidden nodes and x the number of input variables. While only four parameters are added for each additional input variable. Hence, extra memory always requires more parameters than extra input variables. Therefore, to limit the number of parameters in the model and minimize the risk of over-fitting, the addition of a variable to the model should be preferred over the addition of a memory cell.

An interpretation of the network is that the development of the slope state in the last 32-days is described by the LSTM node. The state is scaled, and otherwise matched to the individual benchmarks, by the output neurons. The four days are an extrapolation of the current state of the system, no prediction of the conditions on the slope is made.

The 'mean squared error' was chosen as the loss function. This function, that quantifies the difference between the predicted and observed deformation, is to be minimized during training. The quality of the prediction is measured on the period not used for training. This function assures the cumulative deformation over time

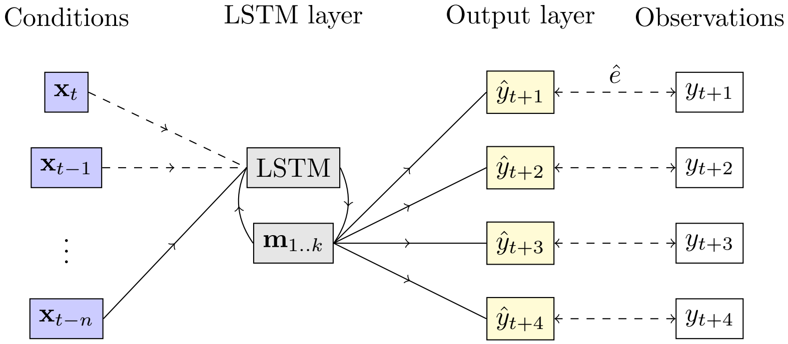

Figure 4.5: Simplified schematic of the model. From left to right: the hydro-meteorological conditions ($\mathbf{x}_t$) on the slope at the current (t) and n preceding time steps; the LSTM layer, including its internal feedback and memory cells ($\mathbf{m}_{1..k}$); the output layer $\hat{y}_t$, which combines the k memory-cells $\mathbf{m}$ of the LSTM node to four predictions; the observations y_t, as available for comparison during training and validation. During initialisation, the conditions on the slope are fed to the system on a day-by-day basis, starting at the oldest observations. The output layer is only invoked at the last iteration, with the final values of the LSTM memory. The parameters of the LSTM layer are optimized on both deformation time series in parallel, the output nodes are tuned individually for each benchmark.

is realistic, as errors are balanced between over- and underestimation. Therefore, the predictions will not show a bias towards acceleration or deceleration.

The TensorFlow machine learning framework was chosen to implement the model (Google, 2022). The LSTM model is implemented in a stateless fashion: the warm-up phase is repeated for every nowcast. The model was run on a workstation based on an Intel Xeon W-2123 (4 cores, 8 threads, 3.6 GHz) with 32 GB RAM, while model variations were tested on the high performance computing cluster of the Delft University of Technology. Given the limited size of the region of interest, as well as the limited number of parameters, the full model fits into 1 GB of memory.

4.4.4 Model training & validation

During training the model parameters are tuned such that the final model state best describes the deformation prediction. The model is optimized with the Adam optimizer (Kingma and Ba, 2017). The model is trained on the loss, after 50 training passes that do not lower the mean squared error over the training period, the model's parameters are fixed. If this steady state is not achieved after 25 000 passes, the training is stopped anyway and the model parameters used as-is.

Due to temporal correlation training and validation cannot be divided over random chunks or batches, according to the 'traditional' 30%–70% chunks (Gholamy et al., 2018). Therefore, the training data is split into equal years instead, as shown in

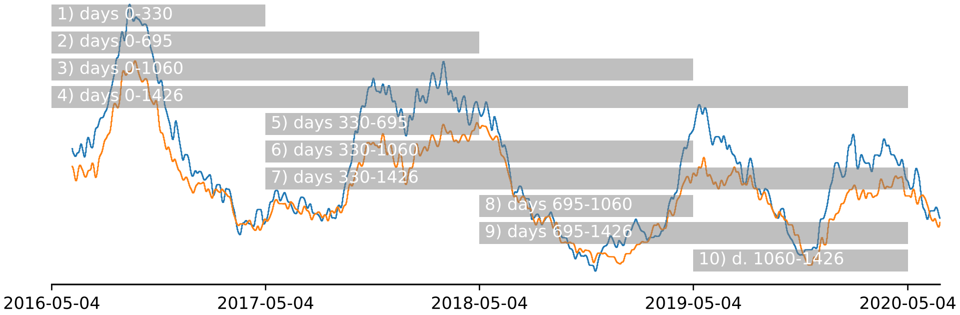

Figure 4.6: Training periods as supplied to the model. The data outside the training period is used for validation. Note that with the longest training period (4), there is very limited validation data left. The deformation pattern (Figure 4.2) is shown in the background for reference. As there is no clear seasonality in the deformation signal, the data set was split in approximate years from the start of the measurements.

Figure 4.6. Data outside the training period is used for validation. This includes the period before the training period, when available.

The robustness of the model to the selection of the training data is assessed from the stability of the results when training over the subsequent periods (Figure 4.6), a variation on cross-validation (Krkač et al., 2020). Each model iteration starts with the same (random) initial weights, but is trained independently from the start. The quality of fit is assessed by evaluation of the loss function, the mean squared error, on the periods not used for training. Finally, the model performance is compared between the training periods. Large deviations of the model quality suggest there are dynamics the system is not capable of describing.

To assess the impact of irrelevant data on the system, as well as the effect of over-fitting, the additional, correlated random variable (`fake/fake`) is used. Over-fitting will make the model prone to spurious correlation with this variable, that results in poor performance in the validation stage. Furthermore, to ensure there is no accidental correlation between the seasonal noise and the deformation signal during training and/or validation, the signal was re-rendered for every model run.

All possible combinations of the eleven input variables were tested on the model. With eleven variables this results in $2^{11} - 1 = 2047$ combinations, as each of the time series may be used or not (2 options), expect for the case where no input is used. Furthermore, the model was trained and validated on each of the ten combinations of training and validation year(s). Each sequence of model training and validation was repeated at least three times, to account for the 'luck' introduced by the random initialization of each model. In total 147 984 model runs were performed.

4.5 Results

The best solution out of all model runs, judged on the minimal mean squared error on validation, is based on a single LSTM-node and only four of the eleven input variables available: precipitation from GPM (V2); soil moisture from SMAP (V5) and ERA5 (V7); and evaporation from GLEAM (V8), where the numbers refer to Table 4.1. The minimal mean squared error on validation was achieved when the model was trained over period 3 (Figure 4.6, 2016-05-04–2019-05-04), the mean squared error of this model run was 1.03 $\frac{\text{cm}^2}{\text{year}^2}$, below the average of 3.15 $\frac{\text{cm}^2}{\text{year}^2}$ ($\sigma \approx 1.3\,\frac{\text{cm}^2}{\text{year}^2}$, from 1718 samples) for this model configuration.

The full nowcast is shown in Figure 4.7, including the training period shaded in gray. Although, based on visual inspection, reasonable results are achieved in summer and autumn, the nowcasting model is unable to predict the deformation rate in winter and spring in the training period. Especially surprising is the jump in the winter of 2018/2019, where a strong acceleration is predicted which does not occur until early summer. The validation period, from 2019-05 onwards, shows little variation. The deceleration in the summer and autumn of 2019 is overestimated and shifted, likewise the acceleration in the December 2019 is predicted correctly, but too early. Overall the predictions show long-term stability (Figure 4.8) as enforced by the choice of the mean squared error as loss function.

The modelling results are overall unsatisfactory: the acceleration and deceleration are typically not predicted timely, or not at all. This is surprising in the light of the success reported by others (Table 4.3). Although we designed our model to match our understanding of the interplay of hydro-meteorological conditions and deformation, the physics behind slope processes at the Vögelsberg landslide, the model was unable to capture this relation. The deformation at Vögelsberg is driven by a complex interplay of hydro-meteorological conditions, unlike most of the examples in Table 4.3, that often includes a strong, stable driver, such as a reservoir. This lack of such a single, strong, driver complicates the working of our data-driven model.

4.5.1 Contribution of individual variables

Due to the complexity of the operations applied to the input signal in the LSTM layer, it is not straightforward to analyze the contribution of the individual components to the final model outcome. As all model variations were tested (§4.4.4), it is possible to analyze the influence of the presence of a variable by comparing the quality of the model variations. For this analysis only model iterations with a training period (Figure 4.6) that left at least one year left for validation were used. Furthermore, all model variations were run multiple times to assess the robustness of the outcome to the random initialisation.

Figure 4.9 shows the results of this analysis, and illustrates the mean squared error over the validation period for all models including each variable. For each variable the minimum and average mean squared error for the validation period are shown, while the maximum mean squared error is often out of range. The thickness of the

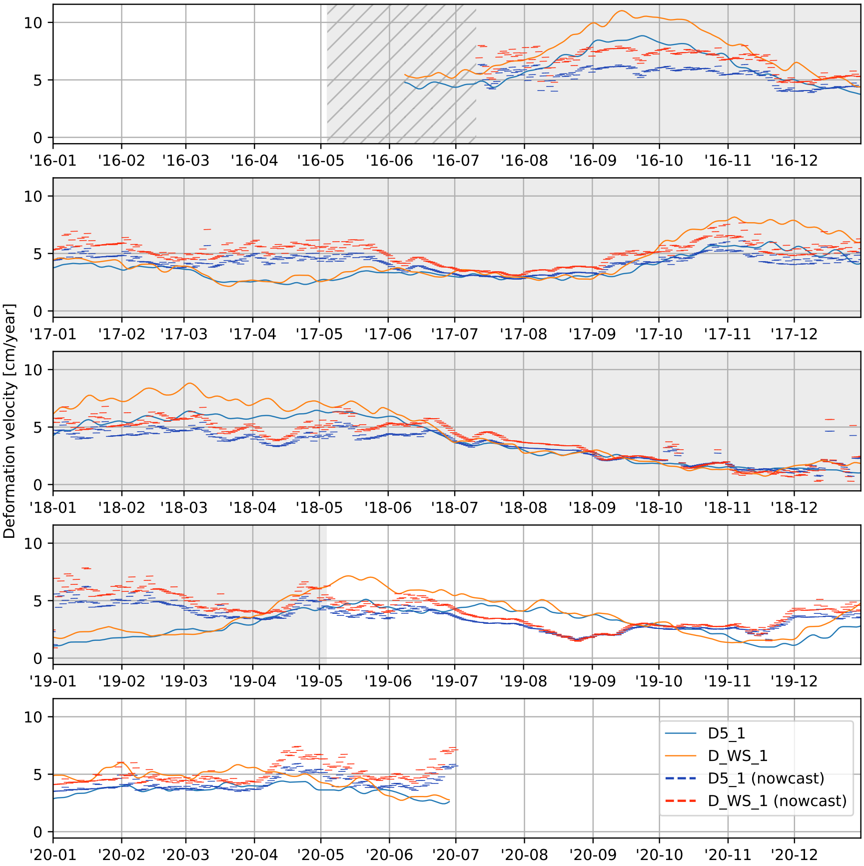

Figure 4.7: Result of the deformation nowcast, run of the full time frame of the available deformation time series. The shaded time span was used for training. Shown as thin lines are the subsequent, daily, nowcasts for benchmarks 'D5_1' and 'D_WS_1'. Per day four deformation nowcasts are shown, with the start of each line being the day after the day the nowcast was issued. Note the warm-up time at the start, shown hatched and without predictions, that is required to initialize the moving average filter on the deformation data and fill the memory of the LSTM-node. The final nowcast ends four days after the end of the reference measurements.

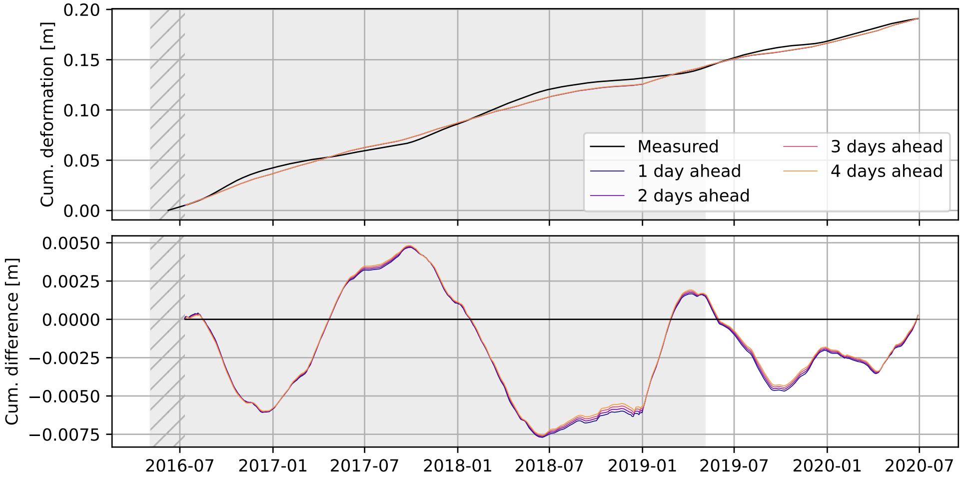

Figure 4.8: The cumulative deformation, as predicted by the consecutive, individual model runs closely matches the observed deformation over the full four years of deformation measurements. The difference is calculated as 'modelled - observed' ($\hat{\mathbf{y}} - \mathbf{y}$) cumulative deformation. The training period of the model is marked in gray, hatched are the warm-up periods of the moving average filter and memory of the model.

line indicates the density of results for that mean squared error, where thicker lines at lower mean squared error indicate a concentration of models with high quality of fit.

Models based only on `SMAP/sm_profile` (V5) score the poorest (highest mean squared error) on average, but with the widest distribution, including many solutions with a low mean squared error. The difference in performance between the variables vanishes as more variables are introduced into the model, however, the models including the SMAP soil moisture (V5) time series show a consistently larger range in performance, including models with a low mean squared error. Remarkable is the approximately equal performance between `API/API` (V10) and `fake/fake` (V11), where the latter contains no information on the hydro-meteorological processes and is only marginally outperformed by the Antecedent Precipitation Index (API, V10). For models with more than four variables, there is no significant difference in model quality for any of the variables.

4.6 Discussion

We believe the unsatisfactory performance of the model has three root causes: i) the inability of the model to capture the complex dynamics of the system; ii) the limited quantity of training data available to this type of problem; and iii) the limited, noisy representation of the slope dynamics in the available remote sensing

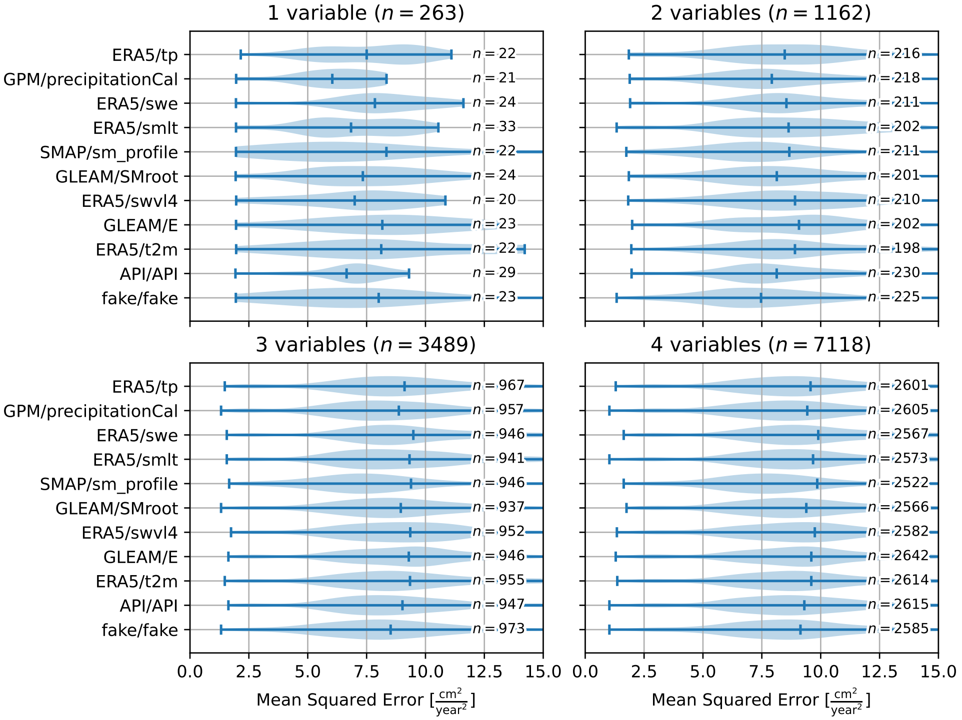

Figure 4.9: Violin plots of the mean squared error for model variations with one to four variables, including the variable listed. For more than four variables the relative importance of the individual variables to the model quality becomes insignificant.

data. Most natural deep-seated landslides are characterized by a complex interplay of causal (antecedent) and triggering conditions: this is also true for the Vögelsberg landslide. However, we believe that it is exactly these challenges that we should aim to tackle with a machine learning model approach.

4.6.1 Model configuration

The possibilities for data-driven modelling are infinite: our model is only a single realisation of the possible combinations of variables and operations. This raises three questions regarding the model selection: i) how to match model and process; ii) how to validate and quantify the quality the nowcast; and iii) how to tune the model implementation.

The major challenge for the model of a deep-seated landslide is the discrepancy between the sub-daily variations of the input (especially precipitation and snowmelt), and a delayed, daily output (accelerated deformation). Therefore, non time-aware models show erratic behaviour, as the consequence of sudden changes to conditions such as snow cover and as well as (extreme) precipitation, that, in reality, do not translate into immediate acceleration. Traditionally, the addition of groundwater physics, smoothing the hydro-meteorological signal, circumvents these peaks. However, the addition of groundwater physics requires knowledge of the geohydrology of the specific slope.

An LSTM-node resembles a bucket model, and was chosen such to capture the delay between precipitation and deformation, by modelling the build-up of water in the model. Our results showed that our model was unable to fully capture these hydro-meteorological dynamics. For reference five alternative models were implemented (Table 4.2), that were designed to better address the diversity of the slope, and/or lower the number of parameters required by the model to prevent over-fitting.

The `lstm3-32` model contains two additional memory cells (buckets) in the LSTM-node, compared to the `lstm1-32` model previously used. The concept is that the memory cells may represent different systems or layers in the subsurface, potentially interacting with each other. For each subsequent time step, all states are included in the calculation of the new states, and could therefore also model interactions between layers in hydrology, such as the transfer of between layers. The `rnn1-32` and `rnn3-32` models based on a traditional Recurrent Neural Network are similar to their LSTM counterparts, with one and three memory cells respectively. However, unlike an LSTM-node, they are unable to ‘forget’ their state on command, and are more susceptible to unstable behaviour. The `rnn1lin-32` did not incorporate an activation function and is comparable to a moving average filter with interaction between the variables. For all three models the number of parameters is less than for the equivalent LSTM based models.

The `da-32` model resembles a linear least squares model. Variables are first summarised as their average over their 32-day history, and included in eight nodes without bias in the hidden layer of the network. The final predictions are a lin-

Table 4.2: List of reference models tested for comparison to `lstm1-32`. Their performance is shown in Figure 4.10. To calculate the number of model parameters: n the length of the time series provided to the model, k the number of input variables, m the number of memory cells, and h the number of hidden nodes. A single hidden layer is assumed. The number of parameters includes the final, output layer of four nodes for each of the two deformation time series.

Model	Hidden layer	Activation	History	Parameters
`lstm1-32`	LSTM (1 memory cell)	tanh	32 days	$4(k+m+1)h+2(4\cdot m+4)$
`lstm3-32`	LSTM (3 memory cells)	tanh	32 days	” ”
`rnn1-32`	RNN (1 memory cell)	tanh	32 days	$h(k+m+1)+2(4\cdot m+4)$
`rnn3-32`	RNN (3 memory cells)	tanh	32 days	” ”
`rnn3lin-32`	RNN (1 memory cell)	none	32 days	” ”
`da-32`	8 cells	none	32 days	$h\cdot k+2(4\cdot h+4)$
Lin. Least Sq.	none	none		$2(n\cdot k\cdot 4+4)$

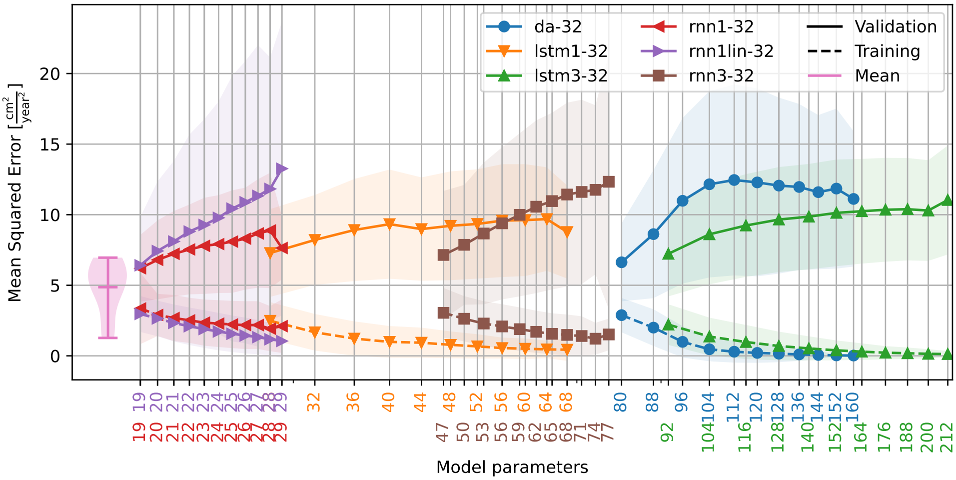

Figure 4.10: Relationship between the number of model parameters and the quality (mean squared error) of training and validation as extracted from the 147 984 model runs. The number of parameters is related to the number of input variables. For LSTM based networks, for example, there are four parameters per input variable per LSTM memory cell required. Note the logarithmic scale on the x-axis. On the left, the mean squared error is shown would the mean deformation rate be used as a nowcast, based on all nine training periods (Figure 4.6).

ear combination of the node values. In a ‘traditional’ linear least squares solution, a direct combination of all input variables, the number of parameters will often outnumber the number of observations available, and was therefore not tested.

The performance of each model is shown for comparison in Figure 4.10, as function of the parameters required. Model performance is typically optimal for models with only a single parameter, and is comparable between the models. Like the original model (`lstm1-32`), each model was re-run multiple times with a random initialisation of the seasonal noise (V11) and model parameters, to verify the consistency of the output. Most alternative models do not outperform the average deformation rate as predictor for the future deformation rate, as shown in Figure 4.10.

Performance metric

For early warning systems, prediction of the onset of acceleration (Figure 4.11) is more important than the deformation quantity. However, false alarms, triggered by insignificant accelerations, may undermine confidence in the early warning system. At this stage of development, we would rely on professional interpretation by an expert to limit the number of false alarms. However, the system should warn the expert for potentially bad predictions, for example due to previously not encountered conditions. The timing of the nowcast should allow for further analysis of the prediction without jeopardising precautionary measures for accelerated deformation.

This leads to five desired properties for the nowcasting system: the system should i) predict onset of acceleration; as well as ii) the maximum deformation velocity; iii) four or more days ahead that deformation will begin; iv) predict when the slope is 'stable' again; and v) quantify the certainty in the prediction. Unlike most estimation problems, the timing and not only the quantity of the predicted deformation is important to the user. An acceleration phase predicted too early or slightly late may still trigger the desired alertness, and still serve a purpose, even though the predicted amplitude on that day is wrong.

A 'standard' error metric, e.g. the mean squared error, is sensitive to the mean as local optimum, but is unbiased and therefore stable in the long term. As an alternative such error metric could be evaluated at 'peaks & valleys', the peaks of the deformation rate, only, emphasizing extremes and disregarding their onset. With this method there are less samples, only the extremes, but they are less correlated and include the amplitude of the event. Although this captures the timeliness of the extremes, it disregards timing of the onset and pattern of the acceleration phase. Moreover, this approach requires information on the peaks and valleys, and that those are correctly identified beforehand.

Due to the lack of information on the extremes of the deformation, we chose to use the mean squared error as error metric. This metric ensured a long term stability, and connected stability of the deformation nowcast, as demonstrated by the cumulative deformation (Figure 4.8). As a consequence, the system preferred 'average' solutions, overestimating the deformation rate in stable periods and underestimating the deformation rate in periods of accelerated deformation. For reference, the mean deformation rate was determined over each of the nine training periods (Figure 4.6) and used as 'predictor' for the remainder of the time series. This constant deformation rate 'model' outperforms many of the more parameter heavy models over the validation period and its mean squared error is shown on the left of Figure 4.10.

Accelerations of the Vögelsberg landslide are known to be triggered by precipitation in summer/autumn and by snowmelt in winter/spring (Pfeiffer et al., 2021). Simple models, based on a limited number of variables and/or with limited modelling freedom, may not be able to cope with both driving forces. As a consequence, their overall performance will be poor. The overall performance, however, does not reflect the performance per season or acceleration trigger. Therefore, to make such model behavior explicitly visible, seasonal differences in performance could be included in the evaluation of the model's performance for example by evaluating a model's performance metric per season as well. Training the model per season, however, will require sufficient, dynamic training data to be available over each season, severely reducing the length of time series available.

Derived variables

Additional variables may be derived from the direct observations. In our model, the Antecedent Precipitation Index (API) is such derived observation, and was chosen to enhance the information content of the hydro-meteorological observations to the model (i.e. provide higher predictive power to the model). This ‘feature generation’ is an important component of more traditional machine learning techniques, where the system is not expected to derive those relations autonomously. Derived, additional features were extensively used by Krkač et al. (2020, 2017), for example, who created additional features to capture the conditions on the landslide, or Miao et al. (2022) who derived ten features from only two sources (rainfall, reservoir level). Drawback of the addition of large quantities of such derived variables to the system is that each additional time series requires additional model parameters to be optimized.

Handling unencountered conditions

Given the limited availability of deformation measurements, most of the data is required to train the model. Moreover, the variation in conditions is limited to the variation in those five years. It is therefore likely that the model will encounter conditions in operation that it had not encountered before. The continuous nature of the model proposed, and the alternatives discussed in §4.6.1, the output for such conditions is not bound to the previously encountered conditions.

For simple combinations of variables, i.e. of a single or a few variables, the response may be tested empirically. Note that the full 32-day history has to be included in this simulation. However, the response may not be so straightforward: a warm summer day combined with hail from a thunderstorm may trigger an unrealistic ‘path’ in the model. Therefore, for more variables, the number of potential combinations increases drastically and may no longer be feasible to simulate.

Predictions of extraordinary responses are not necessarily undesirable, an unbound acceleration, i.e. landslide collapse, prediction should be possible. However, the model would preferably warn for a potential unstable state of the nowcasting system. This could be achieved by an ensemble of models, either based on the same model, or model variations. Especially models with different time series lengths may be able to help pinpoint the source of the discrepancy.

Spatial distribution

Our model of Vögelsberg is based on two benchmarks, that are on two distinct sections of the slope (Figure 4.1) that have shown to exhibit different deformation behaviour. The southern, inhabited part of the slope exhibits constant deformation, with limited acceleration in wet periods. In contrast, the benchmark on the northern part of the slope shows strong accelerations and deceleration as a delayed response to strong precipitation (Pfeiffer et al., 2021). Although our models are unaware of this spatial relationship, it is found empirically during training as the shared LSTM-node, representing the slope processes, is weighed differently for each benchmark.

As an alternative, a location index could be specified, for example as binary indicator of the landslide section, or as continuous signals such as a distance to the centre.

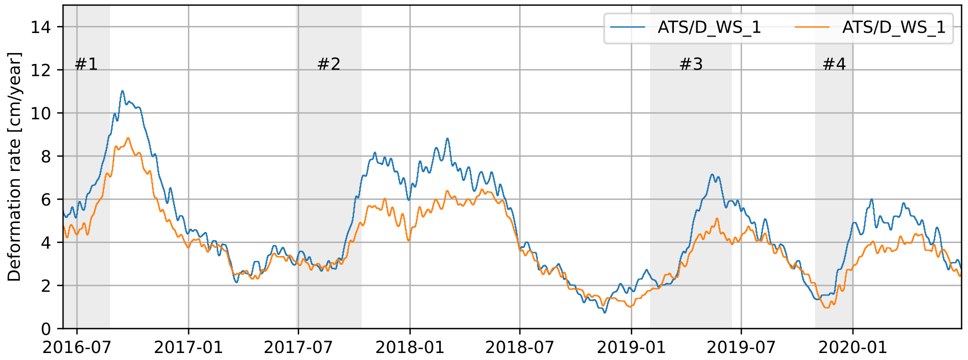

Figure 4.11: Three acceleration events (#1, #2 & #3) at the Vögelsberg landslide, as identified by Pfeiffer et al. (2021). The fourth acceleration period (#4) was identified in the data acquired after Pfeiffer et al. (2021).

Instead of two or more predefined outputs from the same model, a single model may handle different benchmarks differentiated by additional input variables encoding their position within the system. However, given the shallow model design, care should be taken to design the model such that this index works as a scaled multiplier of the hydro-meteorological conditions.

4.6.2 Limited number of distinct events

Over the full time span of the measurements, four distinct acceleration periods can be identified (Figure 4.11). Especially these acceleration periods are of interest to an early warning system, as they mark the start of a period of accelerated deformation and associated hazard. Although the periods of accelerated deformation are comparable in length to the periods of continued, but reduced, deformation, the acceleration events are much shorter (Figure 4.11). Therefore, these periods are underrepresented in error metric during training and validation. However, training on these four periods alone leave insufficient variability to describe the system and reliably fit the required model parameters. Furthermore, the episodic deformation behaviour poses a challenge to the prediction system since the forcing variables on the slope do not reflect such sudden changes observed in the deformation behaviour, as shown in Figure 4.3.

Length of training

Given there is more than a single degree of freedom in the model, without prior knowledge of the process, there is no predictive power in a single acceleration event. Hence, multiple events are required to properly train complex models, in the absence of constraints on the process/model. As a consequence, due to the limited variety of events in the training data, the predictive power of the nowcasting system may be reduced, due to over-fitting on the characteristics of these events only.

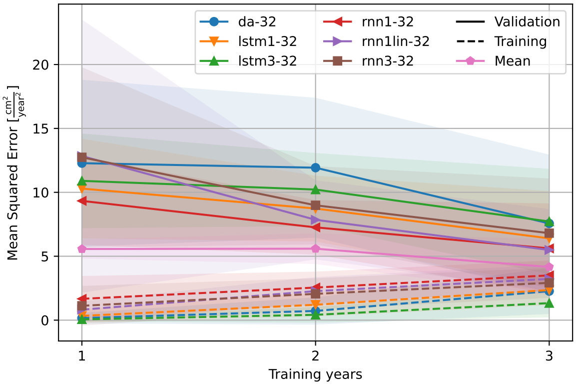

Figure 4.12: Length of the training region, aggregated to (approximate) years, compared to the quality of fit of the model, measured as the mean squared error. An increase in model fit is visible with the increase in training length, however, most models are outperformed by the mean deformation rate as a predictor.

To test the effect of the training length on the models, the models were trained on nine of the ten training periods identified in Figure 4.6 that had a least a year left for validation. The mean squared error, measured on the training as well as validation period, is shown in Figure 4.12. The results are consistent between the models: all models show that as the training period increases, the quality over the training period decreases (dashed line, increasing mean squared error) due to the increased variability of the events therein. Likewise, the quality over the validation period increases (solid line, decreasing mean squared error), as the model generalizes better. This is also reflected in the lower standard deviation for validation over longer training periods. Hence, a longer training period makes the system more robust against the variations encountered by the system.

To train and validate the nowcasting system, the time series was subdivided in calendar years measured from the start of the measurements. An alternative, common subdivision would be in hydrological years or water years, that are typically defined to be from October 1 to September 30 and divided by the precipitation minimum (Lins, 2012). This subdivision is typically applied to cut the data in a hydro-meteorologically quiet period of the year. However, the strong deformation events in period 1 and 2 overlap with this subdivision. Furthermore, with this subdivision, only three periods would be available, instead of four. Moreover, Parajka et al. (2009) show that the period of minimum precipitation cannot be pinpointed to a single winter month. Therefore, the decision was made to align the training years with the measurements instead.

Noise reduction of the deformation signal

Essential to the success of the nowcast are the properties of the signal to be predicted. The effect of noise in the deformation signal on the modelling is twofold: first, random perturbation complicates the training by masking the best solution, and, second, leads to an underestimation of the final quality of the model during validation. Hence, the noise in the deformation signal defines the upper limit for the quality of the deformation estimate. Up-slope deformation, present in the raw deformation time series, was considered to be unrealistic and therefore noise by definition. Under the assumption that the noise is unbiased, the noise will be reduced in averaged samples. Therefore, a moving average filter was applied to the deformation time series with increasing length until no negative deformation remained.

The model was developed with the requirements for an operational system in mind, restricting the system to only use historic observations at any point in the process. Inclusion of future samples would require the system to react to future conditions that have not (yet) been observed on the slope: any filtering, such as smoothing, should not drag future observations back in time. Therefore, the moving average filter cannot be centered, and averaging is applied to the preceding 31-days, rather than ±15 days around the current time step as would be possible in re-analysis.

The variation in the deformation signal at Vögelsberg is relatively small, in deviation from a long term trend. Due to the milimeter-scale measurement uncertainty in the deformation measurements, the deformation signal is dominated by noise on the short time scale of days to weeks, the relevance of a deformation prediction on a daily basis is doubtful. Furthermore, due to the inertia of the landslide body, as well as smoothing of the deformation measurements, accelerations and decelerations are spread over adjacent days (Figure 4.6) and the amplitude of the acceleration is lost. For a successful, daily application, a clear separation between events and noise is required (higher signal to noise ratio), either due to a faster process, or due to reduced noise in the deformation observations.

4.6.3 Input variables

The variable selection in Table 4.1 was compiled based on our knowledge of the physics behind the landslide process, as well as the availability and continuity of the data. With the ambition for a future, regional implementation in mind, the variables preferably come from satellite remote sensing observations rather than local, field sensors. However, we did not succeed in a fully remote sensing driven operation, due to the limited availability of such operational products. Especially deformation observations from space ('InSAR') were found to be promising but we were unable to replace our local deformation time series with the noisier satellite deformation data.

Availability of variables

The model was designed under the assumption that data from all sources is continuous and readily available to the system. Traditionally, local weather and groundwater monitoring stations provide timely, local, high quality observations. However, such monitoring stations are not available everywhere. Out of the variable selection (Table 4.1) only GPM (V2) and SMAP (V5) satisfy this condition and provide operational data products, that could be integrated in a nowcasting solution.

For a successful integration of satellites observations in an operational nowcasting system, a high, sub-weekly, update frequency is required. However, most remote sensing products were available at a delay of days to weeks, still too late for integration in a nowcasting system. As a consequence, the variable selection in Table 4.1 contains variables that are only available in yearly iterations (e.g. GLEAM).

Satellite radar interferometry (InSAR) is a proven method for landslide deformation monitoring (Colesanti and Wasowski, 2006; Hilley et al., 2004). However, especially mountainous environments create a complex interplay of local atmospheric effects and topography (Hanssen, 2001). A feasibility study showed that the slope orientation and topography would allow for the application of Sentinel-1 satellite radar deformation measurements at Vögelsberg (van Natijne et al., 2022a). Further processing of Sentinel-1 data demonstrated the presence of persistent scatterers on and around the houses at the slope, the objects of primary interest. However, the use of satellite based InSAR as source of the deformation measurements was not feasible, due to the low temporal resolution, as well as the noise in the deformation signal (Zieher et al., 2021).

Data continuity

Temporal continuity of input data is required to provide the model with consistent samples of the slope conditions. Short periods of missing data, e.g. days, may be forward filled, but will reduce the data quality for the full integration length (i.e. 32 days). Observations received late may still be updated in later iterations, to mitigate this effect. However, what to do with missing data: a single day or a whole season, or the termination of a data source, for example due to satellite failure? As a fallback one could model and train systems with different variable combinations in advance, and nowcast based on the best model available for the variable combination available in the 32 days prior.

The LSTM-nodes may be implemented in a stateful fashion, where the state of the hidden nodes is retained after each prediction. Such implementation is more computationally efficient, as each subsequent nowcast will require only a single pass over the most recent data. In such implementation, however, discontinuous or erroneous variables may have a lasting effect on the model memory. Therefore, the system was based on continuous re-initialisation with a 32-day observation history instead. The computational drawback is limited, given the small scale of the model, and is acceptable in the light of the greater operational flexibility.

Variables not related to the hydro-meteorological cycle

Indirect observations of the hydro-meteorological cycle may still prove valuable to the nowcasting system. The temperature, for example, may serve as a proxy indicator for evaporation. Temperature is related to the seasons in most climates, and therefore there will be a correlation with the season (day-of-year) as well. However, extra care should been taken including variables that describe the typical/average condition, such as the season. Such variables do not capture the current dynamics of the system and may only describe average conditions, and constrain the system in extraordinary circumstances. The Vögelsberg landslide is known to be sensitive due to changes in the ground water level, irrespective of the season.

Input variable selection

The success of a data-driven model lies in the (expert) selection of the input data. Unrelated variables make the system prone to spurious correlations, especially with limited training data compared to the degrees of freedom in the model or if the method is unable to discard or otherwise ignore sources with low information content. Furthermore, unrelated input variables, or even just noise, should not yield sensible results: “garbage in, garbage out”.

The effect of noise in the conditions was tested by the inclusion of a Brownian motion signal (see §4.4.4), that does not have a relation to the system, except for basic properties (i.e. mean, standard deviation, autocorrelation period) similar to the input variables. Any model run including this signal should not outperform an otherwise comparable model without this variable. However, many of the models did, especially when many (≥ 5) variables were included, where it helped to create unique variable combinations and allowed the model to over-fit.

Parameters on geology and topography were left out of the selection, and assumed static. However, neither were land cover changes included. In the case of Vögelsberg, it was known that little changes were to be expected over the time frame of the measurements available. An alternative to the inclusion of such variables is to frequently re-train the model on a recent section of the time series only to adapt to changes. However, although the system will adapt to changing dynamics, relearning will mask the drivers behind long term effects, and/or adapt too swiftly, for example to seasonal differences, reducing the overall model quality. Land cover changes will not be uniform across slopes, as well as act on different time scales (e.g. neglected pasture fields versus forest fires), and may not be trivial to capture by remote sensing. Moreover, especially in regional studies, the land cover and land cover change may not be comparable between slopes.

To limit the number of variables, only the observation or modelling result closest to the Vögelsberg landslide was used from regional products. However, as Pfeiffer et al. (2021) found, precipitation and snow-melt higher up in the catchment is relevant for the system (Figure 4.1). Based on the typically low ($\simeq 10$ km) spatial resolution of the variables (Table 4.1) it is justified to consider a single observation only. When higher resolution observations are added, this should be reconsidered, and additional points may be added as extra variables.

4.6.4 Outlook

Our results show that deformation nowcasting is an open challenge. Although well monitored, the Vögelsberg landslide is a complex system, and therefore not a straightforward test case. Our results are inconclusive whether our method could work on other deep-seated landslides. More direct dynamics, and/or stronger and more frequent acceleration periods would help constrain the system. The inclusion of field data, such as groundwater level (Krkač et al., 2020), might be another approach to bypass modelling of the most volatile hydrological processes. The ideal slope to further develop a machine learning based nowcasting method has the following characteristics: i) a dynamic deformation behaviour; ii) is controlled by hydro-meteorological conditions, with limited delay; and iii) has field monitoring data for reference and training.

For short time series machine learning methods are known to be outperformed by basic statistical methods (Makridakis et al., 2018). Therefore, our current challenge to nowcast deformation time series may be partially solved in the near future by the natural extension of time series. Furthermore, continued development of the (satellite) data products by their providers may enable new possibilities. Desirable improvements include timeliness of delivery of data products, as well as their precision and spatio-temporal resolution.

Notable is the recent publication of the first version of the European Ground Motion Service data set (Crosetto et al., 2020), a pan-European InSAR product. This data set will allow for experimental, regional, weekly nowcasting systems based on a replay of historic observations. Regional applications will enhance training possibilities and may help overcome the hurdle of limited deformation time series, as multiple slopes are monitored simultaneously. However, to 'learn' from the differences between slopes, and enlarge variation in training data, events have to be largely uncorrelated.

4.7 Conclusions

Although Vögelsberg is a well monitored landslide, the number of recorded acceleration events, within the available four years of daily deformation measurements, is limited compared to other machine learning problems. A simple, time series capable model with limited parameters was required, therefore, we designed an LSTM-based machine learning algorithm to nowcast the deformation of the Vögelsberg deep-seated landslide from the conditions on the slope. The algorithm was trained on maximum three years of deformation observations and satellite observations of relevant hydro-meteorological conditions at the slope. The best model configuration and variable combination was determined by cross-validation with 147 984 model variations.

Although rooted in the landslide dynamics, even our best model was incapable of capturing the versatility of responses of the Vögelsberg landslide, and convincingly predict the deformation rate at Vögelsberg four days ahead. Especially the four acceleration events were not predicted timely, although the mean squared error successfully constrained the average deformation rate of the prediction to that of the training time series. The Vögelsberg landslide showed versatile dynamics, where the full range of slope dynamics and responses to the hydro-meteorological conditions were not present in the available data. Therefore, the slope processes were too complex to model the landslide deformation from satellite surface observations, given the limited observations of acceleration events. Hence, the machine learning model was incapable of 'understanding' the relation between conditions and deformation.

Deformation nowcasting will be a necessity for regional or even continental landslide monitoring and early warning systems. Satellite remote sensing has the potential to provide longer time series, over wide areas. This leads us to the general recommendation for the application of machine learning to reactivating, deep-seated, landslides: improve data quality, and lengthen the deformation time series. The ideal landslide for further development of deformation nowcasting: is highly dynamic (many events to train on), has a limited delay between forcing conditions and deformation, is well monitored, and does not undergo catastrophic failure.

4.8 Appendix

4.8.1 Data

See Figure 4.13.

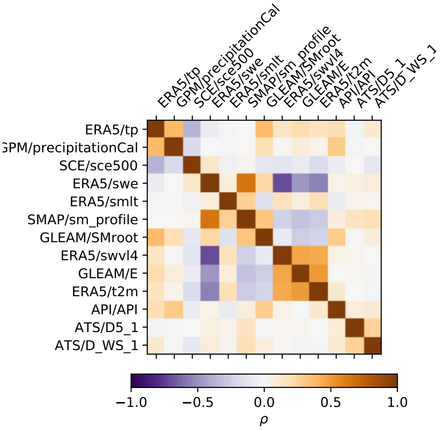

Figure 4.13: Correlation between variables.

4.8.2 Total Station

See Figure 4.14.

4.8.3 Models

State-of-the-art

See Table 4.3.

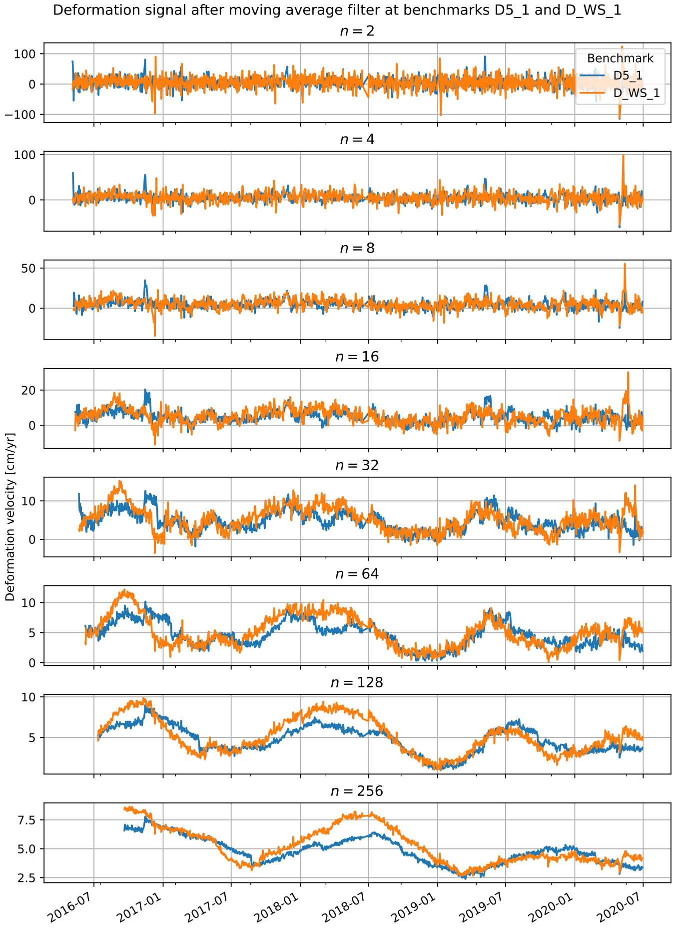

Figure 4.14: Smoothed deformation signal, shown for an increasing length (in days) of the moving average filter. The filter only includes historic observations, and is not 'centred', to match the properties of an operational system. The increasing time lag is visible for the subsequent filter lengths by the right shifting of the velocity peaks. For initial observations, a filter length of half the final length of the filter was accepted.

Table 4.3: Examples of different integration methods, linking hydro-meteorological conditions to deformation time series, and associated case studies. Most studies are at deep-seated landslides that did not undergo catastrophic collapse. Where applicable the reference methods used in the paper are listed in brackets. Updated after van Natijne et al. (2020).

	Case study	Obs. driving forces	Deform. meas.	Notes
Miao et al. (2022)	Baishuihe, China	Rainfall, reservoir level	GNSS	
Zhang et al. (2021)	Fengning, China	Rainfall, toe excavation (incl. blasting)	Total station, inclinometer, fissure meter	
Deng et al. (2021)	Hollin Hill, United Kingdom	Rainfall, acoustic	Inclinometer	
Li et al. (2021)	Baishuihe & Bazimen, China	Rainfall, reservoir level	GNSS	
Liu et al. (2020)	Baishuihe, Bazimen, Baijibao, China	Rainfall, reservoir level	GNSS	
Krkač et al. (2020)	Kostanjek, Croatia	Rainfall, groundwater	GNSS	
Bossi and Marcato (2019)	Passo della Morte, Italy	Rainfall, groundwater	Inclinometer	
Li et al. (2019)	Baishuihe, China	Rainfall, reservoir level	GNSS	
Liu et al. (2021)[a]	Longnan, China	Rainfall	InSAR	
Wang et al. (2019)	Tanjiahe, China	Rainfall, reservoir level	GNSS	
Xie et al. (2019)	Laowuji, China	Rainfall, toe excavation	Total station	
Yang et al. (2019)	Baishuihe & Bazimen, China	Rainfall, reservoir level	GNSS	
Zhang et al. (2019)	Majiagou, China		Inclinometer	
Li et al. (2018)	Baishuihe, China	Rainfall, reservoir level	GNSS	
Miao et al. (2018)	Baishuihe, China	Rainfall, reservoir level	GNSS, inclinometer	
Huang et al. (2017)	Baishuihe & Bazimen, China	Deformation	GNSS	
Krkač et al. (2017)	Kostanjek, Croatia	Groundwater (change), season	GNSS	
Logar et al. (2017)	Ventor, United Kingdom	Rainfall	Crackmeter	
Ma et al. (2017)	Zhujiadan, China	Rainfall, reservoir level	GNSS	
Wen et al. (2017)	Shuping, China	Rainfall, reservoir level	GNSS	
Zhu et al. (2017)	Kualiangzi, China	Rainfall	GNSS	
Cai et al. (2016)	Xiluodo, China	Rainfall	Extensometers	
Cao et al. (2016)	Baijiabao, China	Rainfall, groundwater, reservoir level	GNSS	
Zhou et al. (2016)	Bazimen, China	Rainfall, reservoir level	GNSS	
Jiang and Chen (2016)	Baishuihe & Liangshuijing, China	Rainfall, reservoir level	GNSS	
Lian et al. (2015)	Baishuihe & Bazimen, China	Rainfall, reservoir level	GNSS	
Ren et al. (2015)	Shuping, China	Rainfall, reservoir level	GNSS	
Liu et al. (2014)	Baishuihe, China	Deformation	GNSS	
“ ”	Super-Sauze, France	Deformation	Extensometer	
Chen and Zeng (2013)	Baishuihe, China	Deformation	GNSS	
Du et al. (2013)	Baishuihe & Bazimen, China	Rainfall, reservoir level	GNSS, inclinometer	
Lian et al. (2013)	Buishuihe, China	Undisclosed?		
Corominas et al. (2005)	Vallcebre, Spain	Groundwater	Extensometers	Physics based
Neaupane and Achet (2004)	Okharpauwa, Nepal	Rainfall, groundwater	Autoextensometer	

---

[a] Analysis, allows for prediction.

Chapter 5

Synthesis

In this project we set ourselves the goal "to create a system for nowcasting of landslide deformation at Vögelsberg based on readily available remote sensing data using machine learning techniques". At the start of the project, we found ourselves strengthened by the confidence of Logar et al. (2017): "for such landslides [with displacement monitoring systems, red.] it shouldn't be too difficult [sic] to study the evolution of its displacements vs. time taking into account relevant influencing parameters with the aim to make the accurate short term prediction of their further movements." The complex slope dynamics at the Vögelsberg, however, proved to be a challenge.

Landslides are just one of the many processes that may be monitored from space, and the Vögelsberg was only one of the Open Air Laboratories (OALs) in the OPERANDUM project (Figure 5.1). Although the natural hazards in OPERANDUM are very diverse, their common denominator is the relevance of hydro-meteorological forcing. Furthermore, they share the necessity for monitoring. Although the specific requirements for monitoring may be different at each OAL, a standardised practice in the collection and ingestion of data is desired.

The implementation of Nature Based Solutions (NBSs), as envisioned in the OPERANDUM project could be simplified to a five-step procedure that can be applied to natural hazards at any scale: detect, track, identify, mitigate, and verify. Specific to deep-seated landslides this procedure would be as follows: detect landslide systems by their (ongoing) deformation or by landscape patterns as a result of deformation; track the slope for reactivation by monitoring deformation; identify the underlying processes, by linking the conditions on the slope to landslide deformation; mitigate the hazard by the implementation of (nature-based solutions) targeting the triggering factors previously identified; and verify the working of the mitigation solution by continued monitoring.

It is, however, impossible to design, implement and monitor an experiment within

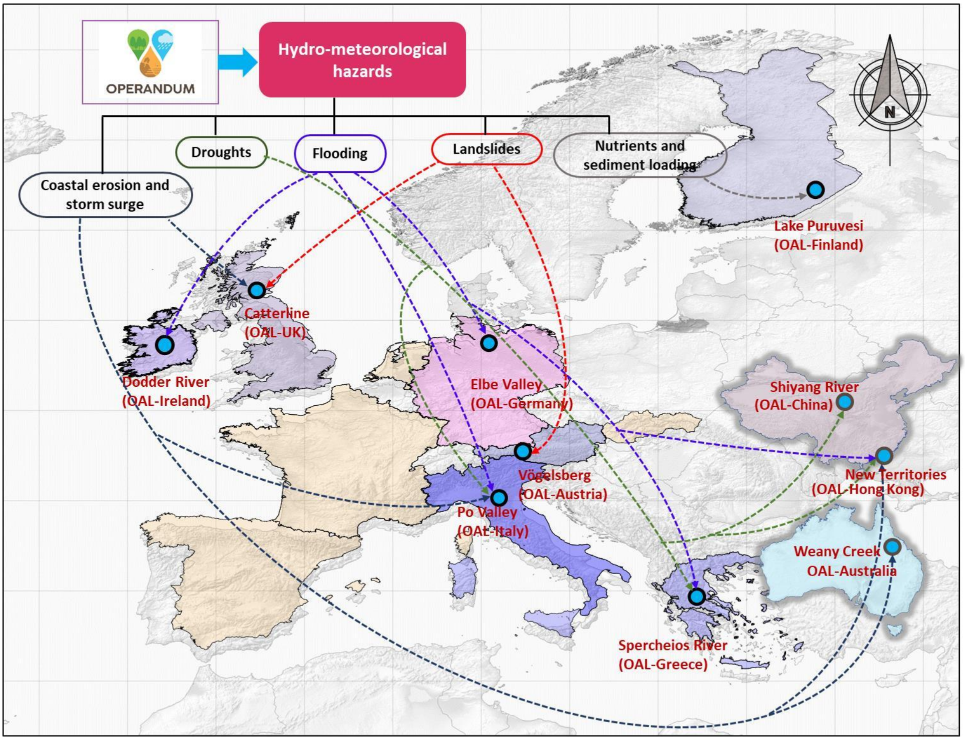

Figure 5.1: Open-Air Laboratories (OALs) within the OPERANDUM project. (Map taken from OPERANDUM deliverable 1.2.)

the four year time-span of the OPERANDUM project. Furthermore, the small scale of the experimental intervention at the Vögelsberg, made it largely impossible to draw conclusions at slope scale. Nevertheless, the effectiveness could be estimated from the local effects, via surveys around the intervention. However, due to the scale of this analysis, there was little role for satellite monitoring.

This lack of success in the implementation of remote sensing for landslide nowcasting, however, should not overshadow the possibilities of remote sensing. After all, remote sensing does provide all ingredients for a nowcasting procedure and has a positive track record from continental scale vegetation monitoring (Büttner, 2014) to the small scale analysis of individual industrial facilities (Villamil Lopez and Stilla, 2021). Domain expertise, on the specifics of the natural hazard and its surroundings, may help pinpoint variables of extra interest. Furthermore, the conclusion of Chapter 4, that machine learning requires an extensive, diverse and high quality training data set, provides a reference frame for future attempts.

This synthesis chapter covers two elements from this thesis, that deformation nowcasting experiment at the Vögelsberg has revealed. First, Vögelsberg specific considerations that do not necessarily transfer to other slopes will be reviewed. Second, challenges regarding the data processing chain, that are more generally applicable to modeling problems, will be discussed. We made it work, however, there are improvements possible to accelerate geo-information workflow.

5.1 Modelling choices at the Vögelsberg

Three design decisions, embedded early-on in this study, are reflected upon in order to ease and improve future machine learning modelling research. The considerations are: i) the applicability of the long short-term memory model to reactivating, slow-moving landslides; ii) the domain of validity of our models; and iii) the choice not to include historic deformation data as input to the model.

5.1.1 Applicability of long short-term memory model

Although various other models were tested (§4.6.1), a Long Short-Term Memory (LSTM) based model proved to provide the best results with minimal variables (§4.5). LSTM (Hochreiter and Schmidhuber, 1997) was designed to cope with training problems encountered in long time series. Although more stable, and easier to train, the output of the LSTM nodes is less intuitive, and yields a complex response to the input variable time series. Therefore, two topics require a review: i) interaction of the model with the input variables; and ii) the performance of the models compared to trivial models.

Input variable selection and preparation was a manual, expert driven, exercise. Due to the limited surface displacement training data, automated extraction of relevant input variables, i.e., end-to-end deep-learning, has not been scratched upon. The effectiveness of our selection of input variables has been reviewed in §4.5.1, indicating soil moisture as the most promising variable. In the absence of sufficient, redundant surface displacement training data, expert feature creation is required. Moreover, expert selection helps to understand the model and helps prevent the creation of a model based on spurious correlation (Kirchner, 2006). Meyer et al. (2019), for example, demonstrate the consequences of model over-fitting due the inclusion of geospatial variables not representative to the process.

In an attempt to create an enriched input variable with improved predictive power, the Antecedent Precipitation Index (API) was calculated and added as a separate variable (§4.4.2). As the process it describes is known to be related to the landslide process, such information rich variables were expected to help the model training. However, the addition of the API to the input variables did not have the desired effect, and did not lead to an improvement of the quality of the prediction (Figure 4.9). In hindsight, the addition of the API, that acts as a bucket model, may counteract a similar, desired bucket-like effect of the LSTM nodes.

The LSTM nodes activate their memory cells based on a trigger in the variables. In another application of LSTM nodes, namely natural languages, the nodes are used to model the probability of word sequences (Sundermeyer et al., 2012). Contrary to this application, in our setup there is a filling of the bucket, but not a single signal that indicates a critical stage that might initiate acceleration. Therefore, there is limited added value in the ‘gates’ of the LSTM node for our application, also indicated by the similar performance of the traditional recurrent neural network (`rnn1-32`, Figure 4.10) that does not have them.

Chatfield (1993) hinted on the importance of the comparison between predictions based neural networks and those based on traditional methods. As example, Chatfield provided a financial model, that, although ‘optimal’ had curious coefficients upon further inspection. Our models were compared against the mean deformation (Figure 4.10), and were shown to be outperformed by mean deformation as predictor based on the mean squared error. However, we would like to add the need for a ‘soft’ verdict by a domain expert. The mean deformation does not convey the variability in the deformation, nor the timing of such changes, and is therefore not a helpful insight in landslide deformation hazard management (Kirchner, 2006).

Unresolved in this thesis is the link to true deterministic modelling and training such model on this data. Crosta et al. (2014), for example, calibrated a physics based model based on the deformation data with partial success.

5.1.2 Model domain

During operation, nowcasting systems may encounter previously unseen conditions. Extreme precipitation, for example, that had no comparable counterpart in the training phase, should still result in a sensible prediction and/or warning of a potentially unstable prediction. Therefore, knowledge on the limits of the validity of the model is required. Furthermore, the model could be purposely operated on simulated conditions such as provided by climate models. Moreover, the current model was based on two point measurements only, and it could be beneficial to extend the knowledge gained from the deformation time series to a spatially continuous model of the slope. Each of these use-cases requires an estimate on the validity of the prediction.

The model validation performed in this thesis, is a variation of cross-validation with both Leave-Time-Out and Leave-Variable-Out strategies (Meyer et al., 2018). In a Leave-Time-Out strategy a subset of the time series was used for training (Figure 4.6), while the rest was used for validation. The Leave-Variable-Out strategy was evaluated in §4.5.1 by the evaluation of all model combinations. However, in this context the short surface displacement time series used for training did not contain a redundant series of events. Therefore, every Leave-Time-Out run had to predict one or more previously unseen acceleration phases but could also not be validated on successful recall of comparable situations.

The lack of recurring events within the training data could be circumvented by training on simulated slopes responses. A deterministic, physics based model, could be run on a large number of combinations of conditions, after which the simulated slope response is used to train the model. This technique was applied for the forecasting of the stability of dikes by Jamalinia et al. (2021), and to landslide slopes by Biniyaz et al. (2022). As there was no physical model available of the Vögelsberg, we were unable to test the stability of the nowcasting system based on synthetic data. Question is, however, if such model could be formulated given the complex interactions at Vögelsberg as identified by Pfeiffer et al. (2021, 2022).

The sparse surface displacement time series do not convey the spatial variability in the slope (Figure 4.1). A simulation based training technique could provide spatially continuous model training data at the cost of prior knowledge of the spatial discontinuity. However, due to the required prior knowledge of the variability, such modelling is mostly useful as proof of concept. Including spatial variation, however, requires some form of spatial encoding of the desired slope position. Either the spatial encoding, in the form of an extra variable, or the model should account for the spatial differences on the slope, such as geological variation.

Inspiration may be drawn from land cover classification systems that have shown to be capable of describing both sharp and gradual transitions between different land cover types. Kathmann et al. (2022), for example, showed that training on two distinct vegetation covers may still lead to smooth classification, including classification of intermediate vegetation types. However, this conclusion could only be drawn after expert consultation, and may not generalize to spatial variability in the landslide process. In a study designed for continental and hence spatially diverse models, Meyer and Pebesma (2021) defined a model's 'area of applicability'. Their accuracy estimate, delineating the region of applicability, was based on an a dissimilarity index of the variables encountered during training and the current input to the model. This estimate, however, was solely based on the input variables, and unless the input includes information on the slope, does not cover its spatial variation.

5.1.3 Exclusion of the deformation signal

Failure predictions based on satellite radar deformation time series only were not possible due to the too low repeat frequency of acquisitions (e.g., 6–12 days for Sentinel-1). Increase in deformation data availability possible by additional satellites and different acquisition strategies may change this in the future. For the 10th ESA Earth Explorer mission opportunity a geostationary radar satellite mission, HydroTerra, was proposed. The geostationary orbit would enable it to provide sub-daily observations (Calvet et al., 2019). Such observations would benefit both shallow and deep-seated landslide monitoring, due to the very high repeat frequency of observations. However, even if it would have been selected as candidate mission, we are at least a decade away from operational systems, notwithstanding the complex interaction of the observation scenario with the mountainous topography.

Our model was developed with this lack of adequate deformation time series in mind, and with the strict design decision not to include the current deformation rate. At the Vögelsberg, however, daily deformation updates are available. Knowledge of a recent, known status is likely beneficial to the prediction of subsequent deformation. Models including recent deformation resemble a Kalman filter setup, where a model run is an update to a known, recent state (Kalman, 1960). However, due to the small day-by-day changes, such configuration comes with increased risk of inadequate error metrics. Furthermore, there is a limited number of tipping points in the data, only three for every acceleration event, to train and validate the system on.

However, the inclusion of previous deformation could be useful to restrict the possibilities of the system and force the model to chose the relevant path. Such steering is possible in neural networks, where in deeper networks there may be multiple routes through the network. As an alternative, the system could be designed to predict change (of deformation behaviour), rather than exact deformation rate, and hence be independent of the current deformation rate.

To assess the model's performance, it should be verified by a comparison to a trivial model (Chatfield, 1993; Makridakis et al., 2018). Chapter 4 demonstrated that average deformation rate has comparable or better predictive power than most of the machine learning models. This demonstrated the ineffectiveness of our models in the prediction of Vögelsberg landslide deformation. The comparison is fair, as both the machine learning model and the average deformation are unaware of the current deformation characteristics.

The `lstm1-32` model (§4.6.1) was re-run on model configurations including a historic deformation rate time series. Including the deformation history as model input did severely reduce the mean squared error. For comparison, the mean squared error was calculated for the trivial prediction of constant deformation, i.e., tomorrow will be equal to today. The mean squared error under the assumption of constant deformation was calculated as:

$$\mathrm{MSE} = \frac{\sum_{t=1}^{n}\left(r_t - r_{t-1}\right)^2}{n} \approx 0.006\ \mathrm{cm}^2/\mathrm{year}^2, \tag{5.1}$$

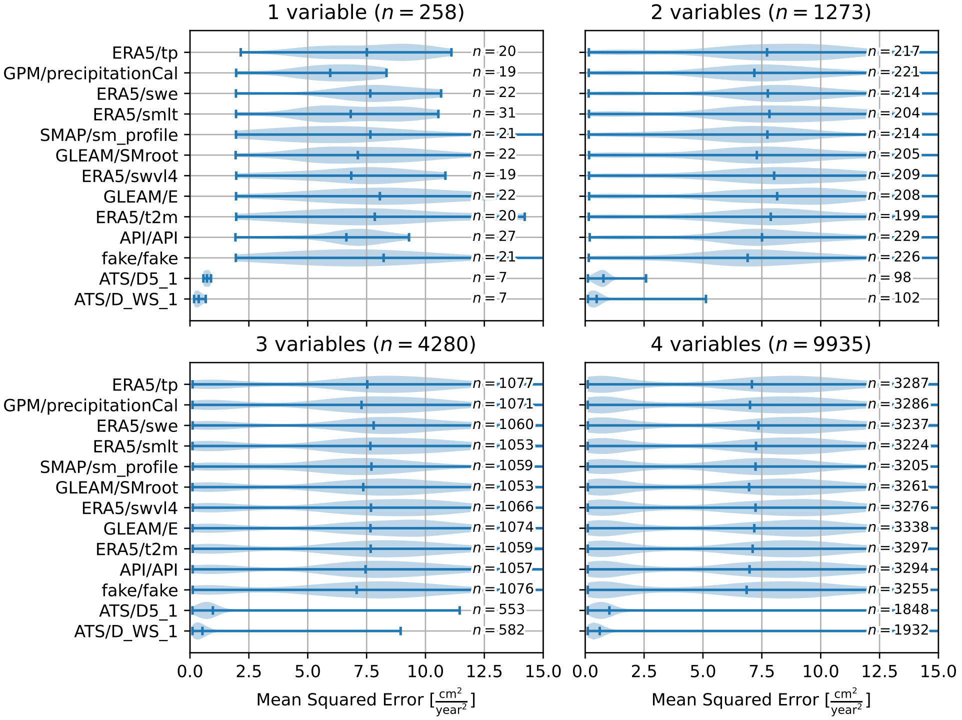

Figure 5.2: Violin plots of the mean squared error for model variations of the `lstm1-32` model (§4.6.1) with one to four variables, based on the variables listed in Table 4.1 complemented with the deformation time series `ATS/D5_1` and `ATS/D_WS_1`. Models based solely on or including the deformation history as forcing parameters to the model, outperform all other model combinations (compare Figure 4.9). Statistics for models with multiple variables are biased, as the number of experiments is unequal. An equal number of experiments, however, would only strengthen this conclusion.

with deformation rate r at time step t for n total time steps. This near-zero error is much smaller than the approximately 4 $\mathrm{cm}^2/\mathrm{year}^2$ obtained by the best model (§4.5), the mean deformation (1–7 $\mathrm{cm}^2/\mathrm{year}^2$, Figure 4.10), and even below the average of models including recent deformation observations (Figure 5.2). Similar values were obtained for a forecast 2–4 days ahead.

5.2 Data availability

The various satellite constellations orbiting our earth acquire terabytes of data every hour (Copernicus, 2018). After sensing and initial processing, this data is made available to potential users for further integration. However, large scale, free availability of imagery is a relatively new occurrence, that has benefited time series analysis (Zhu et al., 2019). For example, publication of the forty year long archive of Landsat data only started in 2008 (Wulder et al., 2016).

To be ‘available’, data has to be: findable, accessible, interoperable and re-usable. These requirements form the FAIR data principles for sharing research data and findings (Wilkinson et al., 2016). We consider data to be ‘readily available’ if this process may be completed without special permission, and proprietary or otherwise restrictive licenses.

In practice, the data distribution process is different for each satellite mission. This form of data handling is outdated to cope with the continuous data stream involved with contemporary satellite remote sensing. Furthermore, the adaptation of new sources is limited by the necessary change of working routines. The growing number of satellite missions (Belward and Skøien, 2015) introduces ever more different routines.

The heterogeneous data landscape complicates automated processing, and is a burden in the initial stages of research. As a consequence, many users will not get beyond the point of manual file selection and processing, and are unable to fully exploit the potential of repeat acquisitions by satellite remote sensing. Therefore, processing of large regions, or consistent processing of many small regions, is only within reach for a limited group of users and businesses. Meanwhile, vendors have demonstrated their ability to reduce the distribution time of Sentinel-1 satellite radar imagery from hours to within two minutes of sensing (Punsvik, 2022). Such developments highlight the requirement for a streamlined data distribution process.

The success of tools like Google Earth Engine (Gorelick et al., 2017) demonstrates the power of readily available data. Unlike the ‘traditional’ route of manual scene selection, downloading and pre-processing, such services have all data directly available to the user to work with. In addition, the data archive and computational facilities are conveniently co-located and taken care of. Revolutionary was this combination of: i) direct access to global, full time series of satellite remote sensing data; ii) co-location of data and computational resources; and, iii), fast large scale analysis, via an image pyramid.

However, the use of external tools is not always favourable. There could be legal constraints on the data or algorithms used and external tools may not support non-standard variables, such as complex radar imagery, local coordinate systems, or regional analysis at full resolution. These situations require a more traditional route of data processing. Recent developments, however, make the traditional route more convenient and level out many of those differences.

Here we will discuss this three stage process associated to data availability of open, freely available, satellite data products: how to find, access and interpret data in earth observation. Note that streamlining data availability is a rapidly developing field. Consequently, this discussion focuses on major trends and does not claim to be exhaustive.

5.2.1 Find data

A search for data will typically start from prior knowledge of the topic of interest, and relevant variables. Careful, expert selection of variables relevant to the process, and understanding of their limitations, has proven to be important (Meyer et al., 2018, 2019). The variable selection is then combined with expert knowledge of the operational satellite missions, their sensors, and available products.

Individual data providers must then be consulted on the products available for the period and region of interest. Data providers provide web interfaces, portals, that may be queried to find data products relevant to the region of interest. Often, products may be filtered based on other requirements as well, such as a maximum cloud coverage or temporal limitations. The specific portals encountered will vary by niche in the field.

Well known portals for raw satellite observations are USGS EarthExplorer[1] (USGS, 2022a), the Copernicus Open Access Hub[2] (Copernicus, 2022e), also known as Sci-Hub, and NASA Earth Data[3] (NASA, 2022b) as integration of NASA's various Distributed Active Archive Centers[4] (NASA, 2021), (Sudmanns et al., 2019). Their images often require further processing to provide the quantities desired for physical modelling.

Various preprocessed interpretations of those images are available as ready made products. Furthermore, there might be multiple providers of the same quantity (e.g. precipitation, see Table 2.2). A variety of portals for processed products exist, such as the topic specific Copernicus Land[5], Marine[6], Atmosphere[7], and Climate[8] data services (Copernicus, 2022c,d,a,b). Portals may also be product specific, such

---

[1] `https://earthexplorer.usgs.gov/`

[2] `https://scihub.copernicus.eu/`

[3] `https://search.earthdata.nasa.gov/`

[4] `https://www.earthdata.nasa.gov/eosdis/daacs`

[5] `https://land.copernicus.eu/`

[6] `https://data.marine.copernicus.eu/`

[7] `https://atmosphere.copernicus.eu`

[8] `https://climate.copernicus.eu/`

as for NASA's Global Precipitation Measurement[9] (GPM) (Hou et al., 2014; NASA, 2022a).

The portals typically have an Application Programming Interface (API), that enables automated queries to the system. Experienced users may develop tools to automate this process of data discovery, although this will be specific to each portal. These interfaces are typically based on XML or JSON responses to queries transmitted over HTTP, although object storage and FTP based archives, indexed as directories, are around as well. Note that where multiple portals provide the same or similar data, their index and access methods to the same data may be different.

Recent developments aim to unify this interface between data providers. While the Open Data Protocol[10], OData (2022), employed by Copernicus is a standardised protocol, it is not tailored to geospatial use. A dedicated geospatial standard, SpatioTemporal Asset Catalogs[11], STAC (2022), first launched at the end of 2022, is currently in use by NASA and Microsoft Planetary Computer. The STAC standard is less flexible than its predecessors, but more straightforward to query. It aims to align with upcoming standardisation by the Open Geospatial Consortium[12] (OGC, 2022), and provide an intuitive data index, that is both human readable and machine interpretable.

Although there is a trend to simplify and standardise data discovery, the process is driven by the operator's knowledge of the products available. Therefore, it will not replace the expert selection variables that are likely relevant to the process of interest. However, standardised data discovery will make it easier to automate the data discovery process and will therefore contribute to a more streamlined data availability.

5.2.2 Access data

Once the desired data products are identified, their contents have to be retrieved for further processing. All previously mentioned data portals offer their data for download as well. However, due to the limited bandwidth between data distributor and user, downloads may span multiple days to weeks, especially if large collections are fetched at the beginning of the project. Furthermore, offline data storage at the portals, in the form of tape, is still common for older, less frequently requested data. These products stored on tape are provided on request, and are not instantly available for download, although they will typically be available for download within the hour.

Third parties may also provide data archives, such as the twenty national mirrors[13] of the Copernicus program (Grazia Castriotta, 2022; ESA, 2022a). In a development accelerated by the Copernicus Data and Information Access Services (DIAS)

---

[9] `https://gpm.nasa.gov/data/directory`

[10] `https://www.odata.org/`

[11] `https://stacspec.org/en`

[12] `https://www.ogc.org/docs/is`

[13] `https://sentinel.esa.int/web/sentinel/missions/collaborative/existing-planned`

(Copernicus, 2018), multiple cloud providers collected similar archives of satellite data that are collocated with the computing services they offer. Although these services do not always offer the full archive, the collocation of the data and processing power accelerates the retrieval process due to the very high, local bandwidth between storage and computing facilities. Other examples, not bound to the DIAS development are the data archives in Google Earth Engine, on Amazon Web Services[14] (AWS, 2022), and on Microsoft Planetary Computer[15] (Gomes et al., 2020; Microsoft, 2022).

Regional to global analysis is possible thanks to the fast access to the archives provided by these services. A prime example of the capabilities when data and computational facilities are aligned is the global, Sentinel-1 radar coherence estimate by Kellndorfer et al. (2022). Use of these services, however, implies an implicit vendor lock-in, that might limit adoption, as not to make success dependent on the longevity of a specific cloud provider. Furthermore, due to the typically high cost of data transfer away from these vendors, these services are especially useful in data reduction operations where the output is limited in size.

As a consequence of this distributed data dissemination reality, data is replicated between multiple different service providers. To ensure reproducible research, original imagery is often kept by researchers as well, leading to further duplication. Especially in studies with aggregated results, this may lead to disproportional requirements on data storage. In practice, most users keep the full sequence of products, as the long-term availability of imagery is not guaranteed.

To reduce the storage requirements and to limit the download volume data providers may offer custom downloads of subsets of their data set. This is a trade-off between computing power at data distributor and the load on users, at the cost of introducing additional complexity for specific requests. In a recent trend, these systems are replaced by file formats that natively allow for partial downloads. One of such formats is the Cloud Optimized GeoTIFF[16], COG (2022), format for rasterized data (images), that is quickly gaining popularity due to its compatibility with existing tools.

The COG is an extension to the popular GeoTIFF format for rasterized data storage (Devys et al., 2019). Like traditional GeoTIFFs, the files are georeferenced, may contain multiple bands and various spatial resolutions. New is that any combination of spatial resolution and subset may be reconstructed ad-hoc from parts of the full file, without intervention from the data distributor. The effectiveness of this COG file format is demonstrated by the ability of standard web browsers (e.g., via GeoTIFF.js[17] (Schindler and Meißl, 2021)), even on mobile phones, to display complex geospatial data.

The USGS has committed itself to release Landsat data as COG (Bouchard, 2021)

---

[14] `https://registry.opendata.aws/tag/earth-observation/`

[15] `https://planetarycomputer.microsoft.com/`

[16] `https://www.cogeo.org/`

[17] `https://geotiffjs.github.io/`

and to provide a STAC index[18] of the collection (USGS, 2022b). The archive for automated access is hosted on Amazon Web Services, where the user is required to pay for data transfer. Free, manual downloads are still possible via USGS EarthExplorer[19], although at much slower speeds (USGS, 2022a). For some users, like academia, it will be cumbersome to pay these small fees, as the administrative load of payment will be much higher than the cost of the data itself.

There are many promising developments to simplify data retrieval for users. The quick adaptation of the Cloud Optimized GeoTIFF format will benefit many users. The open license of the data promotes competition between data distributors, shown by the different offerings available. However, the shift towards paid, high bandwidth data distribution is one to monitor.

5.2.3 Interpret data

Once the user has found and retrieved the data of interest, it is ready for use. There are various standardisation efforts by distributors to simplify interoperability between systems. Standardised naming of variables, such as proposed by Eaton et al. (2017), or other forms of descriptive metadata, may help this process. Other standards are governed by legal context, such as the European directive on Infrastructure for Spatial Information in the European Community: INSPIRE[20] (EU, 2007), or are initiated bottom-up, by stakeholders such as EuroGeographics[21] (EuroGeographics, 2022). However, as no satellite sensor is the same, some interpretation is expected.

For optical satellite imagery, atmospheric corrections may be necessary, for example. Data providers may provide a software package to simplify the process such as sen2cor[22] (Main-Knorn et al., 2017; ESA, 2022b) provided by ESA for atmospheric corrections on Sentinel-2 optical data, or by third parties such as FORCE[23] (Frantz, 2019; Frantz et al., 2022). Furthermore, the data might have to be aligned with other resources. This has led to a variety of workflows to Extract, Transform, and Load (ETL) data from their standardised formats into project requirements.

To limit the user interaction required, the concept of Analysis Ready Data (ARD) was launched. Analysis Ready Data ensures geometric and radiometric standardised reporting of the data, without artefacts and contains a proper error description (Dwyer et al., 2018). Remote sensing is the art of comparison, and ARD is meant to be comparable in space and time without further processing. As a consequence, users have to accept certain assumptions on usage imposed by the data provider. Therefore, the users should understand the limitations of the techniques silently applied for them.

Analysis ready data may come as a new data distribution, such as with the Landsat

---

[18] `https://www.usgs.gov/landsat-missions/landsat-commercial-cloud-data-access`

[19] `https://earthexplorer.usgs.gov/`

[20] `http://data.europa.eu/eli/dir/2007/2/2019-06-26`

[21] `https://eurogeographics.org/`

[22] `https://step.esa.int/main/snap-supported-plugins/sen2cor/`

[23] `https://github.com/davidfrantz/force`

(Dwyer et al., 2018) and Sentinel-2 (Louis et al., 2019) archives. An ARD product for Sentinel-1 is expected to be launched in 2023–2024[24] (ESA, 2022c). The predicate 'analysis ready' might be used for complex operations, such as the virtual constellation of Landsat and Sentinel-2 by Claverie et al. (2018), where the harmonized Landsat Sentinel-2 surface reflectance product[25] is intended to simulate an increased temporal resolution. Another example is the Copernicus Ground Motion Service[26] (Crosetto et al., 2020; Copernicus, 2022f), providing analysis ready InSAR time series.

Readily available data, that may be used as-is, carries the implicit risk that inexperienced users, unknowing of their limitations, will draw erroneous conclusions. The super-resolution algorithm available in the FORCE toolbox (Frantz, 2019), for example, is based on assumptions of spectral homogeneity between acquisitions. Is the user aware of the limitations of this method, and the consequences of this assumption? This is, however, applicable to any data interpretation, and a responsibility of the user. Furthermore, conclusions based upon the data are those of the user and not those of the data provider.

The benefits of readily available data and analysis ready data greatly outweigh these risks. The analysis of a deep-seated landslide by Kalia (2022) was made possible by the availability of analysis ready data, and so are the Landslide Hazard Assessment for Situational Awareness landslide hazard nowcast and forecast (Khan et al., 2022; Stanley et al., 2021; Kirschbaum and Stanley, 2018). Raw satellite data should remain available to expert users, in addition to analysis ready data that will accelerate the development of new applications.

5.3 Data agility

Satellite remote sensing is a dynamic field. Although the development of new satellite missions is a time consuming process, new missions and sensors are launched at an unprecedented rate (Belward and Skøien, 2015). At the same time, satellites come with an expiry date, and an uncertain future, demonstrated by the recent failure of the Sentinel-1B satellite (Potin et al., 2022). Users of satellite data have to adapt their processes to such changes, and should, in parallel, prepare for upcoming opportunities such as new sensors. This requires agility, the capability to quickly adapt models and methods to unexpected developments. This section focuses on the benefits of data agility, and provides suggestions on how a data agile design may improve data availability at project level.

Especially in time critical forecasting and nowcasting systems, continuous, timely data availability is a necessity. It is therefore recommended to design such time critical systems with a fallback in mind. This is stressed by recent threats on

---

[24] `https://sentinels.copernicus.eu/web/sentinel/sentinel-1-ard-normalised-radar-backscatter-nrb-product`

[25] `https://hls.gsfc.nasa.gov/`

[26] `https://land.copernicus.eu/pan-european/european-ground-motion-service`

satellite infrastructure (Roulette, 2022), and concerns on the vulnerability of the sub-sea infrastructure of satellite ground stations (Kirchner, 2020). Therefore, the data and modelling structures should be flexible, allow for temporary changes, and allow for rapid fine-tuning to changing conditions.

Rapid changes in data availability, including Analysis Ready Data (§5.2.3), and data processing strategies require data agility as well. Data science has become a field of its own, and remote sensing expertise may not be present with all users. Therefore, data consistency simplifies collaboration and accelerates algorithm development.

Machine learning has added flexibility, but also many new, ‘black box’, approaches to remote sensing data analysis. The desire to test multiple models for a single problem, stresses the need for a streamlined, computer centered, data organisation. The first step is the streamlined availability of the data (§5.2). Second ingredient is accessible data storage at project level.

In the desire for data-driven systems the power of local, in-situ, data should not be forgotten. Only local field measurements can be tailored to the variables of interest and other project requirements. With an experienced team, local, low-cost sensors may be designed, deployed, retrieved, and the data analysed in the time-span of a PhD project (e.g. den Ouden et al., 2021; den Ouden, 2022). However, new sensors are unlikely to produce enough information for a naive modelling approach in the time frame of a single project. Their role is in the synergy with satellite sensors and the data organisation should therefore be capable of handling both.

Here we reflect on the data organisation within projects, and how this could support data agility. One of our attempts at consistent data organisation, on national scale, is included for reference.

5.3.1 Project level data storage[27]

Data organisation is a hot topic in Remote Sensing. However, sessions on data organisation at scientific conferences are dominated by data distributors and commercial services that aim to facilitate and accelerate data retrieval. Fast and simple data access is desirable at project level as well, and could be achieved even by small groups to simplify their work. However, no generic data storage solution exists, and solutions will therefore always be sub-optimal to other users.

The setup of a unified data storage requires input from project members, and their expectations on the data usage patterns as well as the desired scale of the analysis. When focus is on performance, the bottleneck will be alternating between timely data availability and computing power: the balance between processing power (CPU/GPU), storage, and bandwidth. Storage optimizations may include projection of all data into a common reference frame, downsampling in space and/or time,

---

[27] Text adapted and extended from the author’s contribution to Tuomenvirta, H., Mäkelä, A., Spyrou, C., Apostolidou, E., Panga, D., Gonzalez-Ollauri, A., Corvaglia, P., 2019. Data requirements to assess and monitor OAL performance. Technical Report OPERANDUM D4.1, Finnish Meteorological Institute.

and other data curation tasks that would otherwise be repeated by different project members. Usage patterns, such as parallel processing, are application and platform specific, and no universal definition exists. However, if one is aware of the limitations of their platform, a trade-off can be made between development time, maintainability and performance.

Typically a distinction is made between vector and raster data. Vector data can be points, polylines or polygons in 2D or 3D of infinite location precision. Generally one or more data attributes are attached to those features. This data is assumed to be valid for the whole region described by the feature and may consist of single or multiple attributes, or even a complete time series, such as a population count, crop type, or deformation time series. Examples of such vector features are country borders (polygons), center lines of rivers and streams (lines, with a single river name) or measurements from weather stations (points, with time series attached).

Raster data are regular grids of data, typically in 2D, which carry one or more features in a regular pattern. Rasters are commonly used to store spatially continuous data, and could be output of earlier computational steps, such as orthorectification. There are no requirement on their contents, but decimal (floating point), complex and binary values are most common. While vectors are more suitable for visualization of data with high location accuracy requirements, rasters are often preferred for computational reasons.

The conversion from vector to raster is typically not possible without accuracy loss. Furthermore, rasterization should take into account the different binning characteristics required for the different data sources. Sightings of animals (points, observations in time) can be rasterized both on time and space as density (sightings/hour/km^2) or as cumulative count (sightings/km^2, sightings/hour), for example. And how should such data be spread over the bins or pixels, is interpolation desired and/or is extrapolation to neighbouring pixels justified?

Algorithms require data to be in an systematic, organized format that can be accessed at high speed. Furthermore, linking different variables together is only possible if the variables can be accessed simultaneously. Therefore, the data has to be stored in a common reference frame of space and time, that allows synchronized access between variables. The creation of such reference frame requires agreement on the rasterizing and resampling of the data, and choices on the interpolation/extrapolation/transformation of data from its original form to the new unified reference frame.

Technical challenges lie in the storage of large, high resolution, data sets (Goodchild, 2001). Large, spatially sparse data sets, may pose a problem as well, as many empty values will have to be stored to satisfy the uniform storage format. Compression and on-the-fly generation may limit the adverse effects of data duplication and large empty regions, but come at the cost of increased computational load.

Once operational, such unified reference frame will accelerate subsequent analyses, as after the initial set-up no time is necessary to match the individual parameters of different sensors, quantities and studies. Furthermore, the unified data structure will allow for easier browsing, and simplifies the creation of a 'data dashboard' for exploratory data analysis. Moreover, structured data storage could facilitate fast inter-organizational exchange when desired. An example of inter-organizational data distribution is the "COMET-LiCS Sentinel-1 InSAR portal"[28], that provides near-realtime processing of Sentinel-1 interferograms related to tectonic activity (Lazecký et al., 2020; COMET, 2021).

When usage patterns are varied and limited common ground can be found, the project level requirements on data distribution may resemble those of the initial distributors. However, as project resources are available, those may be allocated to offload part of the data preparation from individual users to an internal service. Such services, typically compliant to the OGC Web Coverage Service[29] standard for raster data (OGC, 2018) and the OGC Web Feature Service[30] standard for vector data (OGC, 2014), prepare the data on-the-fly based on the specific user requirements. Although not yet widely implemented, the OGC Web Processing Service[31] standard aims to offer computing services (comparable to Google Earth Engine) on demand (OGC, 2015).

Data cubes meet aforementioned requirements on data consistency and provide users with standardised access to vast amounts of data. Furthermore, they are well suited for the spatial-temporal properties of satellite remote sensing data and offer seamless access to the data in space and time (Giuliani et al., 2019a). Especially time series analysis is simplified, as the temporal dimension is typically divided over different data products at traditional data portals. However, pre-processing is required to generate a data cube from the individual products downloaded from a space agency, like ESA.

The ESA Earth System Data Lab (Brockmann Consult, 2018), now continued as the Deep Earth System Data Lab[32] (DeepESDL) (Brockmann Consult, 2022) as part of the Deep Cube[33] project (DeepCube, 2021), is an example of elaborate data pre-processing and reference frame unification. Their Earth System Data Cube (ESDC) contains 79 different variables with global coverage, all resampled to the same grid in both space and time (8 days, 0.25°). The cube can be sliced in any direction (location, time, variable). The cube adheres to the CF-1.7 naming convention for interoperability (Eaton et al., 2017) and is stored as a regular grid of Zarr[34] files (Alted et al., 2018).

Creation of a data cube has become a standard practice of some research group, such as the cubes of the eo2cube[35] project at the University of Würzburg (Thiel et al.,

---

[28] `https://comet.nerc.ac.uk/comet-lics-portal/`

[29] `https://www.ogc.org/standards/wcs`

[30] `https://www.ogc.org/standards/wfs`

[31] `https://www.ogc.org/standards/wps`

[32] `https://www.earthsystemdatalab.net/`

[33] `https://deepcube-h2020.eu/`

[34] `https://zarr.readthedocs.io/`

[35] `https://datacube.remote-sensing.org`

2022). Elsewhere data cubes have replaced data on demand services offered based the OPeNDAP protocol (Cornillon et al., 2003), that offers a generic interface to remote matrix-like storage, as method of data publication: NASA's A$\rho\rho$EEARS[36] system provides a data cube on demand of selected sources (NASA, 2015), as an alternative to USGS's deprecated OPeNDAP service[37] (USGS, 2015). A freely available example with a wide variety of variables is the GeoCubes Finland[38] data cube by Lehto et al. (2019); Geoportti (2022). More subject focused is AgroDataCube[39], that is specialised on the Dutch agro-food chain, and offers limited free access on the basis of fair-use (Janssen et al., 2018). For commercial services EuroDataCube[40] acts as a market place (EOX, 2022), while the global Sentinel-1 radar backscatter data cube by Wagner et al. (2021) is offered as a commercial service by EODC[41] (EODC, 2022).

There are various services available to cater an on-demand processing strategy. Rasdaman[42], for example, offers server software for internal data distribution (Baumann et al., 1998; Rasdaman, 2022). The DIAS services (§5.2.2), Google Earth Engine and Ellipsis Drive[43] offer on-demand data distribution strategies as commercial services (Ellipsis, 2022). OpenEO[44] strives for a unified interface between geoinformation services (Pebesma et al., 2016; openEO, 2022), like the C-SCALE project that enables federated data access between data providers (Backeberg et al., 2022). Moreover, EarthServer[45] provides a federation standard for interoperability between data cubes (Jacobs University and Rasdaman, 2020).

5.3.2 A Dutch data cube

We developed a simple, yet effective, data cube generation script for Sentinel-2 imagery, based on Python and the Zarr storage format. Generation of the data cube is a three step process. First, Sentinel-2 imagery over the Netherlands is downloaded in bulk. Second, atmospheric corrections are applied via 'sen2cor' (Main-Knorn et al., 2017). Third, the imagery is reprojected to the desired, national, coordinate reference system (Rijksdriehoekscoördinaten, Lesparre et al., 2019) and the cube is filled or updated.

Our data cube covers 300×340 km in up to 400 time steps per orbit at the time of writing, with new acquisitions added regularly. All bands are at full (10m) resolution and occupy around 4 TB of storage per orbit for the acquisitions 2015–2022. Furthermore, the cube contains a series of additional variables that may support

---

[36] `https://appeears.earthdatacloud.nasa.gov`

[37] `https://lpdaac.usgs.gov/resources/e-learning/lp-daac-data-access-through-opendap-and-web-services/`

[38] `https://vm0160.kaj.pouta.csc.fi/geocubes/`

[39] `https://agrodatacube.wur.nl/`

[40] `https://eurodatacube.com/`

[41] `https://eodc.eu/`

[42] `http://www.rasdaman.org/`

[43] `https://ellipsis-drive.com/`

[44] `https://openeo.org/`

[45] `https://www.earthserver.eu/`

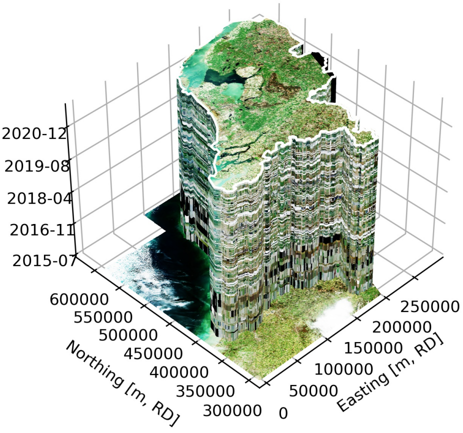

Figure 5.3: Visualisation of the Dutch Sentinel-2 data cube, two slices in time are shown at the top and bottom, while the data is sliced in space along the national border.

analysis and/or allow for quick prototyping of new ideas. The additional resources include: the municipal, provincial and national borders; the land-use[46] (2008, '10, '12, '15, and '17) (CBS, 2022); the farmers' crops per field[47] (2009–2021) (RVO and PDOK, 2022). Thanks to the standardised structure of the data cube, these may be queried in the same fashion as the spectral Sentinel-2 data.

Combinations of these variables with the Sentinel-2 data allows for aggregate statistics, as well as training of various sorts of algorithms. The use in bachelors level education demonstrated the easy of use of such solution. Based on a series of iPython Notebooks[48] in Google Colab[49] students explored the spectral properties of an area of their liking (van Natijne, 2019). A simple script enabled the exportation of manageable sections of the cube to custom GeoTIFF files for further analysis in the graphical environment of QGIS.

Thanks to support of the Netherlands Center for Geodesy and Geo-Informatics, the data cube is publicly available on GeoTiles.nl[50] (van Natijne, 2020). Due to the versatility of the Zarr format, the data cube may also be used offline as it fits on any larger external hard drive. We focused on usability under standard office conditions in educational or development settings, rather than on factors relevant to production systems such as efficient storage or bandwidth cost. These data cubes should fit into storage structures typically found in office environments, and should

---

[46] `https://www.cbs.nl/nl-nl/dossier/nederland-regionaal/geografische-data/natuur-en-milieu/bestand-bodemgebruik`

[47] `https://www.pdok.nl/introductie/-/article/basisregistratie-gewaspercelen-brp-`

[48] `https://weblog.fwrite.org/datacube/`

[49] `https://colab.research.google.com/`

[50] `https://geotiles.nl`

not require complex (cloud) computing infrastructure, but may still be published on any simple web server.

5.4 Conclusion

The complexity of the model formulation at the Vögelsberg illustrates the necessity of expert judgement in the design and evaluation of a study. Therefore, both natural hazard and remote sensing experts are required in these phases of the study, in conjunction with data scientists. Furthermore, a successful cooperation will reveal the magic of the 'black box' for all parties involved.

There are plenty, positive developments in the improvement of data availability, that open up earth observation resources to a broader audience. Analysis Ready Data (ARD), in combination with Cloud Optimized GeoTIFFs (COG) and SpatioTemporal Asset Catalogs (STAC) are developments that will likely shape the data landscape for the coming years. Their ease of interpretation and convenience may make data cubes as separate concept superfluous.

The performance of a new model should be compared to traditional, simple statistical methods (e.g., the mean) to verify their effectiveness. This should not be forgotten as data availability is streamlined and simplified, enabling more complex models.

Chapter 6

Conclusions and recommendations

Slow moving, deep-seated landslides cause extensive economic loss, and thorough understanding of their processes is required for the implementation of effective mitigation measures. In the light of the recent advances in machine learning and satellite remote sensing, short-term forecasting (nowcasting) of landslide deformation was deemed possible. Unlike fieldwork, computer algorithms and satellite observations are not tied to a specific slope, and are easier to scale to regional applications. To nowcast deformation, the conditions on the slope that could initiate or accelerate deformation have to be translated into a landslide deformation prediction by the empirical machine learning algorithm (Figure 1.5).

We set ourselves the goal “to create a system for nowcasting of landslide deformation at Vögelsberg based on readily available remote sensing data using machine learning techniques” (§1.3). A review of the state-of-the-art showed promising opportunities for such systems, with similar systems already implemented elsewhere (Tables 2.4 and 4.3). In this study, the Vögelsberg deep-seated landslide served as an example of how machine learning has the potential to accelerate landslide analyses compared to traditional, involved fieldwork based methods. The methodology developed for the Vögelsberg was expected to be more generally applicable, or at least provide a starting point for regional analysis of similar landslide phenomena.

Research by Pfeiffer et al. (2021, 2022) showed that the Vögelsberg landslide is characterised by complex deformation patterns. However, the availability of a high resolution deformation time series from the local automated total station provided an exceptional reference for the development of a machine learning model.

Here we present our major conclusions, as well as the detailed answers to the research questions governing the deformation behaviour. Furthermore, we summarize recommendations for future endeavours, including practical issues from the development phase of the model.

6.1 Conclusions

This thesis aimed to answer the question:

To what extent can
data-driven machine learning techniques
be used for landslide deformation nowcasting
at deep-seated landslides?

To test the capability of a data-driven machine learning algorithm to predict deformation of the Vögelsberg deep-seated landslide, multiple models were developed and evaluated. The models developed showed limited success in the prediction of the deformation of the Vögelsberg landslide, and rarely outperformed the mean deformation rate as a predictor. Although rooted in the landslide dynamics, even our best model was incapable of capturing the versatility of responses on the Vögelsberg, and did not convincingly predict the landslide deformation rate at the Vögelsberg four days ahead.

This research showed that an ideal landslide for deformation nowcasting is highly dynamic, with many displacement acceleration and deceleration events to train the system on. Moreover, such landslide has limited delay between forcing conditions (e.g. precipitation) and its deformation response, is well monitored and is not catastrophic.

Guiding in this research were the following sub-questions:

1. **What are the requirements for a deep-seated landslide deformation nowcasting system?**

Deep-seated landslides undergo continuous deformation, and possibly accelerate due to changes in the hydro-meteorological conditions. The system should be able to separate periods of relative stability, with minor deformation, from accelerated deformation phases. To assess potential damage to infrastructure such nowcasting system should predict the onset of acceleration, as well as the maximum deformation rate in this acceleration phase. Therefore, a binary predictor of accelerated deformation is insufficient, and the deformation nowcasting system should produce a dynamic (time dependant) quantitative (deformation rate) prediction.

On a day-to-day basis the deformation signal is of millimeter scale, and below the approximately 1 centimeter accuracy of the deformation measurements. As a consequence, it is challenging to detect the onset of acceleration in its early stages. Furthermore, the system should be robust against noisy deformation signals around or below instrument accuracy during the training and validation of the data-driven model.

The specifics of the processes at the Vögelsberg landslide were discussed in detail by Pfeiffer et al. (2021, 2022). The deformation of the Vögelsberg landslide is a complex response to the hydro-meteorological conditions in the catchment, in particular precipitation and (delayed) infiltration from snowmelt. Besides a constant deformation rate of 1.5 cm/year, accelerated deformation of up to 10 cm/year was triggered by snowmelt and/or rainfall. Acceleration and deceleration phases at the Vögelsberg span multiple days, and are delayed with respect to the hydro-meteorological triggers by up to sixty days. A deformation nowcasting system should take into account such a long lag time to unravel the current state of the slope.

2. **What data and model(s) may drive such a nowcasting system?**

   A deformation time series, as source of both the training and validation of the model, is the primary requirement. All explanatory data should be relevant to the forcing of the landslide dynamics. Careful selection of the model, as well as the variables, was expected to lead to a stable, robust, model with minimal parameters.

   The model should be capable to ingest time series of conditions, account for their delayed effects on the slope, and output a deformation forecast for the coming days. To limit the number of model parameters, the choice for the specific machine learning model should be inspired by landslide physics. We focused on Long Short-Term Memory (LSTM) based models, especially for its capability of retaining and integrating historic observations. Overall, the models (Figure 4.5) show resemblance to elementary water balances.

   - What conditions influence the landslide deformation, and are they observable from the surface?

     Reactivating, deep-seated, landslides are in a state of limit-equilibrium, and accelerate or decelerate when conditions change. The sliding behaviour is governed by the balance of forces within the landslide. Changes in hillslope hydrology shift the balance between the shear strength of the soil and the shear (sliding) force applied by the gravitational forces acting on the landmass. As the landslide is known to be there, the pre-disposing factors (e.g. slope) are assumed to be present. Therefore, infiltration of rain, or delayed infiltration due to snow melt, and the subsequent rise of the pore water pressure, are the primary conditions to monitor.

     A series of key variables, that facilitate or trigger acceleration at the Vögelsberg, were identified (Table 2.1). Especially precipitation (rainfall, snowfall) and soil moisture measurements were deemed relevant to the Vögelsberg landslide system. These processes and conditions visible on, or close to, the surface may be observed from space. The Wattenbach stream at the bottom of the Vögelsberg is narrow, as well as surrounded by steep slopes, and cannot be observed from space. However, even in the absence of information on the drainage, it is possible to formulate an elementary water balance.

   - What are the properties of the models used in the state-of-the-art?

     There is a great variety in models and optimization methods used in the state-of-the-art (Tables 2.4 and 4.3). However, many studies focus on GNSS deformation time series of a limited number of slopes around the Three Gorges Dam, China. Moreover, the case studies in literature typically rely on a single, dominant driver, such as reservoir level, and/or high quality measurements closely related to the process, such as the ground water level. Models based on Long Short-Term Memory (LSTM) and Support Vector Machine (SVM) are most popular. The model configurations are typically complex, and the number of parameters in the model is rarely reported.

3. **What satellite based landslide deformation observations are available?**

   Deformation observations are typically obtained from satellites by either image tracking or radar interferometry (e.g. InSAR). Image tracking techniques, unlike InSAR, are most suited for high deformation rates not commonly observed in deep-seated landslides. Due to the complexity of InSAR processing, it is beneficial to a-priori assess the potential of such exercise. InSAR deformation time series could be available from Sentinel-1 on 91% of the global slopes steeper than 5°, given the presence of a coherent scatterer (§3.5). A world map, based on the Copernicus DEM, was developed to indicate the sensitivity of Sentinel-1 radar acquisitions to downslope deformation (§3.4.1). Furthermore, a Google Earth Engine tool was developed for a fast, preliminary analysis of the availability of such coherent scatterers (§3.4.2).

4. **What remote sensing data sources are available?**

   Various remote sensing products are available related to the causal and triggering conditions of accelerated slope deformation. For the Vögelsberg nowcasting system a selection of ten variables and associated data products was made (Table 4.1). These variables covered precipitation, snow, soil moisture, evaporation, and air temperature, from both remote sensing and modelled sources.

   There are multiple sources on precipitation (Table 2.2) and sources of soil moisture estimates available, often with limited delay from sensing. Snow cover, as observed from space, is often a binary observation, with very limited information on the properties of the snow pack. More advanced sources on snow coverage suffer from complications of the mountainous acquisition geometry. As an alternative to currently not timely available remote sensing sources, re-analysis models, partially based on satellite data, were used.

   Rudimental modelling, in the form of expert driven combinations of variables, was expected to help replace variables that can not be observed from space. Simple physics and proxy indicators, such as the antecedent precipitation index (API, §4.4.2) were used to increase the information content in those variables. The API maps the high-frequency precipitation signal to the delayed effect on the slope hydrology.

5. **How to implement a machine learning based deep-seated landslide model?**

   Various, well documented, machine learning software packages exist. Our model is implemented in TensorFlow, as custom sequence of existing building blocks. The combination of various sources into a single, unified time series, was a more involved process. The machine learning framework, combined with the unified time series, allowed for quick prototyping of various model variations (Figure 4.10).

Deformation observations, taken by an automated total station, had to be smoothed by a 32-day moving average filter to reduce the noise in the deformation rate. Our experiments with existing satellite deformation observations (InSAR) at the Vögelsberg showed insufficient temporal resolution in relation to the accuracy to capture the slope dynamics (Zieher et al., 2021). The frequency of the nowcast should match that of the deformation measurements as well as the observations of the conditions of the slope. Given the delayed response of deep-seated landslides, this nowcasting frequency is typically daily or less.

- How to quantify the quality of the nowcasting solution?

  To assess the quality of the deformation nowcast both the deformation rate and the timing of the prediction are important to the user. However, in the absence of clear information on the true timing of the deformation events due to noise, the training and validation could not be focused on acceleration events. Smoothing of the deformation signal with a 32-day moving average filter further reduced the possibilities to quantify the timing of the acceleration nowcast. Therefore, the timing was ignored and the model was trained on the difference between measured and predicted deformation rate on a day-by-day basis only.

  The mean squared error was chosen to quantify the quality of the nowcast, and is defined as the average of the squared difference between the predicted and observed deformation. This error metric is sensitive to timing errors, and early as well as late predicted accelerations are quantified solely by their difference to the observed deformation rate. Long-term stability of the deformation estimate was ensured by the mean squared error, at the risk of settling with the average deformation rate as best predictor.

  To assess the effect of over-fitting on the system, an additional, ‘fake’, time series of ‘seasonal noise’ was introduced during model training. This randomly generated signal, based on Brownian motion with similar correlation properties to the temperature time series, should not contain any predictive power. Therefore, addition of this signal to the nowcast should not increase performance, as it was not related to the landslide deformation process. If, however, a performance increase is observed after addition of the random signal, this indicates that the model is insufficiently constrained by the training and/or validation time series of deformation data. Some of our best scoring models were achieved based solely on this fake signal (Figure 4.9), a strong indication of the lack of robustness of the final model.

- How to quantify the relative importance of the data sources to the result of the nowcasting system?

  The importance of the available time series and combinations thereof to the deformation nowcast was be determined by cross-validation between the models with different variable combinations. There are 2047 possible combinations of the variable selection (Table 4.1), including the seasonal noise. All model combinations were tested by trial-and-error, where variable combinations that drive the models with the lowest mean squared error were considered best.

- What are the major contributing variables to a landslide deformation nowcast?

  Thanks to the limited complexity of the model, and short time series of maximum eleven variables, the system only required minimal computer memory (<1 GB). This enabled us to determine the major contributors by trial-and-error by comparison of model variations. In total 147 984 model variations were trained and evaluated (§4.4.4).

  The quality of the resulting nowcasting systems was compared, to assess which variables are more likely to produce a high quality nowcast (Figure 4.9). Models including soil moisture information from SMAP are more likely to generate high quality nowcasts. Soil moisture might function as a proxy indicator for groundwater, and associated pore pressure on the slope. Models based on precipitation or snow melt scored slightly better as well, although this effect vanishes if more variables were included. The API, however, that was expected to serve as a proxy indicator of pore pressure, did not improve the performance of the model. Providing more than three to four variables, however, led to an insignificant improvement to the mean squared error of the nowcast.

- How many observations/events are necessary to develop the nowcasting system?

  The limited length of the Vögelsberg time series (1 482 daily time steps) did not allow for the empirical assessment of the number of observations needed. Given the model was complete, and capable of describing the slope dynamics, a single observation of each underlying process should theoretically have been sufficient. However, the noise in both the input variables and deformation time series masked such relationship, and a variety of events and triggering conditions was required to overcome this fuzzy relationship with deformation. Furthermore, training data should be balanced between accelerated and relatively stable periods, as not to bias the system towards either. Therefore, no fixed, universal minimum number of observations could be determined.

6. **What do the insights obtained at the Vögelsberg tell us on the general applicability of machine learning based landslide deformation nowcasting models?**

   Compared to typical machine learning applications, the application to landslide deformation nowcasting was data poor. Machine learning based landslide deformation nowcasting models could work for more dynamic landslides, that have a limited delay between forcing conditions (e.g. precipitation) and its deformation response. Dynamic slopes will exhibit their full palette of interaction between triggering factors and changes in the deformation rate over a relatively short monitoring period. Regional application will only add information to the system if the slopes either experience different conditions (e.g. differences in precipitation). For dynamic slopes, or collections of comparable slopes different circumstances, deformation nowcasting might work.

6.2 Recommendations

These initial results at Vögelsberg provide a starting point for experiments elsewhere, and a basis for the reconsideration of design decisions, including the exclusion of deformation data from the input of the model. Slopes with more direct feedback between precipitation and deformation, are the most likely candidates for successful application of machine learning based nowcasting systems. Alternatively, the system could be tested on a regional (InSAR derived) deformation data set, to assess the possibilities of harnessing the dissimilarities between slopes on a regional scale.

This project benefited from a local, high quality deformation time series. Future projects should invest in their data organisation, to take advantage from the local and remote variables available. Furthermore, simplified data access will enable fast prototyping of future models. Ideally such data system is capable of ingesting new observations as they become available, to simulate the challenges of an operational nowcasting solution.

References

Airbus Defence and Space, 2015. TerraSAR-X image product guide. `https://www.intelligence-airbusds.com/files/pmedia/public/r459_9_20171004_tsxx-airbusds-ma-0009_tsx-productguide_i2.01.pdf`, accessed on 2020-10-07. Technical report.

Alfieri, L., Salamon, P., Pappenberger, F., Wetterhall, F., Thielen, J., 2012. Operational early warning systems for water-related hazards in Europe. *Environmental Science & Policy*, 21, 35–49. `https://doi.org/https://doi.org/10.1016/j.envsci.2012.01.008`.

Alfieri, S. M., Foroughnia, F., Van Natijne, A., Mousivand, A., Lindenbergh, R., Porcu, F., Zieher, T., Pulvirulenti, B., Yang, J., Menenti, M., 2021. Documenting Impacts of Hydro-Meteorological Events Using Earth Observation. *2021 IEEE International Geoscience and Remote Sensing Symposium IGARSS*, IEEE, Brussels, Belgium, 934–937. `https://doi.org/10.1109/IGARSS47720.2021.9554905`.

Alted, F., Durant, M., Hoyer, S., Kirkham, J., Miles, A., Ratsimbazafy, M., Rocklin, M., Schut, V., Scopatz, A., Goel, P., 2018. Zarr documentation. `https://zarr.readthedocs.io/en/stable/`, accessed on 2022-04-12.

Anderson, C. C., Renaud, F. G., Hanscomb, S., Gonzalez-Ollauri, A., 2022. Green, hybrid, or grey disaster risk reduction measures: What shapes public preferences for nature-based solutions? *Journal of Environmental Management*, 310, 114727. `https://doi.org/10.1016/j.jenvman.2022.114727`.

Antonello, G., Casagli, N., Farina, P., Leva, D., Nico, G., Sieber, A. J., Tarchi, D., 2004. Ground-based SAR interferometry for monitoring mass movements. *Landslides*, 1(1), 21–28. `https://doi.org/10.1007/s10346-003-0009-6`.

Arnone, E., Francipane, A., Scarbaci, A., Puglisi, C., Noto, L., 2016. Effect of raster resolution and polygon-conversion algorithm on landslide susceptibility mapping. *Environmental Modelling & Software*, 84, 467–481. `https://doi.org/10.1016/j.envsoft.2016.07.016`.

Aslan, G., Foumelis, M., Raucoules, D., De Michele, M., Bernardie, S., Cakir, Z., 2020. Landslide mapping and monitoring using Persistent Scatterer Interferometry (PSI) technique in the French alps. *Remote Sensing*, 12(8), 1305. `https://doi.org/10.3390/rs12081305`.

AWS, 2022. Registery of open data on Amazon Web Services. `https://registry.opendata.aws/tag/earth-observation/`, accessed on 2022-11-30.

Baarda, W., 1968. *A testing procedure for use in geodetic networks*. Publications on geodesy, 5, 2 edn, Netherlands Geodetic Commission, Delft.

Backeberg, B., Šustr, Z., Fernández, E., Donchyts, G., Haag, A., Oonk, J. B. R., Venekamp, G., Schumacher, B., Reimond, S., Chatzikyriakou, C., 2022. An open compute and data federation as an alternative to monolithic infrastructures for big Earth data analytics. *Big Earth Data*, 1–19. `https://doi.org/10.1080/20964471.2022.2094953`.

Barrington-Leigh, C., Millard-Ball, A., 2017. The world's user-generated road map is more than 80% complete. *PLOS ONE*, 12(8), 1–20. `https://doi.org/10.1371/journal.pone.0180698`.

Baumann, P., Dehmel, A., Furtado, P., Ritsch, R., Widmann, N., 1998. The multidimensional database system RasDaMan. *Proceedings of the 1998 ACM SIGMOD international conference on Management of data - SIGMOD '98*, ACM Press, Seattle, Washington, United States, 575–577. `https://doi.org/10.1145/276304.276386`.

Beck, H. E., Pan, M., Roy, T., Weedon, G. P., Pappenberger, F., van Dijk, A. I. J. M., Huffman, G. J., Adler, R. F., Wood, E. F., 2019. Daily evaluation of 26 precipitation datasets using Stage-IV gauge-radar data for the CONUS. *Hydrology and Earth System Sciences*, 23(1), 207–224. `https://doi.org/10.5194/hess-23-207-2019`.

Beck, H. E., Vergopolan, N., Pan, M., Levizzani, V., van Dijk, A. I. J. M., Weedon, G. P., Brocca, L., Pappenberger, F., Huffman, G. J., Wood, E. F., 2017. Global-scale evaluation of 22 precipitation datasets using gauge observations and hydrological modeling. *Hydrology and Earth System Sciences*, 21(12), 6201–6217. `https://doi.org/10.5194/hess-21-6201-2017`.

Belward, A. S., Skøien, J. O., 2015. Who launched what, when and why; trends in global land-cover observation capacity from civilian earth observation satellites. *ISPRS Journal of Photogrammetry and Remote Sensing*, 103, 115–128. `https://doi.org/10.1016/j.isprsjprs.2014.03.009`.

Bengio, Y., Simard, P., Frasconi, P., 1994. Learning long-term dependencies with gradient descent is difficult. *IEEE Transactions on Neural Networks*, 5(2), 157–166. `https://doi.org/10.1109/72.279181`.

Benoit, L., Briole, P., Martin, O., Thom, C., Malet, J.-P., Ulrich, P., 2015. Monitoring landslide displacements with the Geocube wireless network of low-cost GPS. *Engineering Geology*, 195, 111–121. `https://doi.org/10.1016/j.enggeo.2015.05.020`.

Berardino, P., Costantini, M., Franceschetti, G., Iodice, A., Pietranera, L., Rizzo, V., 2003. Use of differential SAR interferometry in monitoring and modelling large slope instability at Maratea (Basilicata, Italy). *Engineering Geology*, 68(1-2), 31–51. `https://doi.org/10.1016/S0013-7952(02)00197-7`.

Bernardie, S., Desramaut, N., Malet, J.-P., Gourlay, M., Grandjean, G., 2015. Prediction of changes in landslide rates induced by rainfall. *Landslides*, 12(3), 481–494. `https://doi.org/10.1007/s10346-014-0495-8`.

Bianchini, S., Herrera, G., Mateos, R., Notti, D., Garcia, I., Mora, O., Moretti, S., 2013. Landslide activity maps generation by means of Persistent Scatterer Interferometry. *Remote Sensing*, 5(12), 6198–6222. `https://doi.org/10.3390/rs5126198`.

Bickel, V., Manconi, A., Amann, F., 2018. Quantitative assessment of digital image correlation methods to detect and monitor surface displacements of large slope instabilities. *Remote Sensing*, 10(6), 865. `https://doi.org/10.3390/rs10060865`.

Biniyaz, A., Azmoon, B., Sun, Y., Liu, Z., 2022. Long Short-Term Memory based subsurface drainage control for rainfall-induced landslide prevention. *Geosciences*, 12(2), 64. `https://doi.org/10.3390/geosciences12020064`.

Bogaard, T. A., Greco, R., 2015. Landslide hydrology: from hydrology to pore pressure. *Wiley Interdisciplinary Reviews: Water*, 3(3), 439–459. `https://doi.org/10.1002/wat2.1126`.

Bogaard, T. A., Greco, R., 2018. Invited perspectives: hydrological perspectives on precipitation intensity-duration thresholds for landslide initiation: proposing hydro-meteorological thresholds. *Natural Hazards and Earth System Sciences*, 18(1), 31–39. `https://doi.org/10.5194/nhess-18-31-2018`.

Bolch, T., Kamp, U., Olsenholler, J., Oluić, M., 2005. Using ASTER and SRTM DEMs for studying geomorphology and glaciation in high mountain areas. *Proceedings 24th EARSel Symposium on New Strategies for European Remote Sensing, Dubrovnik, Croatia, May 25 - 27, 2004*. `https://doi.org/10.5167/uzh-137249`.

Bonì, R., Bordoni, M., Vivaldi, V., Troisi, C., Tararbra, M., Lanteri, L., Zucca, F., Meisina, C., 2020. Assessment of the Sentinel-1 based ground motion data feasibility for large scale landslide monitoring. *Landslides*, 17(10), 2287–2299. `https://doi.org/10.1007/s10346-020-01433-3`.

Bossard, M., Feranec, J., Otahel, J., others, 2000. CORINE land cover technical guide: Addendum 2000. Technical Report 40/2000, European Environment Agency Copenhagen.

Bossi, G., Marcato, G., 2019. Planning landslide countermeasure works through long term monitoring and grey box modelling. *Geosciences*, 9(4), 185. `https://doi.org/10.3390/geosciences9040185`.

Bouchard, M., 2021. It's time to make the move to Landsat Collection 2. `https://ui.adsabs.harvard.edu/abs/2021AGUFM.B35D1459B`, accessed on 2022-11-09.

Brabb, E. E., Pampeyan, E. H., Bonilla, M. G., 1972. Landslide susceptibility in San Mateo County, California. Technical report, US Geological Survey.

Brenning, A., 2005. Spatial prediction models for landslide hazards: review, comparison and evaluation. *Natural Hazards and Earth System Sciences*, 5(6), 853–862. `https://doi.org/10.5194/nhess-5-853-2005`.

Brockmann Consult, 2018. Earth System Data Lab. `https://www.earthsystemdatalab.net/`, accessed on 2019-03-25.

Brockmann Consult, 2022. DeepESDL: Deep Earth System Data Lab. `https://www.earthsystemdatalab.net/`, accessed on 2022-11-15.

Brunetti, M., Melillo, M., Peruccacci, S., Ciabatta, L., Brocca, L., 2018. How far are we from the use of satellite rainfall products in landslide forecasting? *Remote Sensing of Environment*, 210, 65–75. `https://doi.org/10.1016/j.rse.2018.03.016`.

Budimir, M. E. A., Atkinson, P. M., Lewis, H. G., 2015. A systematic review of landslide probability mapping using logistic regression. *Landslides*, 12(3), 419–436. `https://doi.org/10.1007/s10346-014-0550-5`.

Büttner, G., 2014. CORINE Land Cover and Land Cover Change Products. I. Manakos, M. Braun (eds), *Land Use and Land Cover Mapping in Europe*, 18, Springer Netherlands, Dordrecht, 55–74. Series Title: Remote Sensing and Digital Image Processing.

Cai, Z., Xu, W., Meng, Y., Shi, C., Wang, R., 2016. Prediction of landslide displacement based on GA-LSSVM with multiple factors. *Bulletin of Engineering Geology and the Environment*, 75(2), 637–646. `https://doi.org/10.1007/s10064-015-0804-z`.

Calvet, J.-C., Black, E., Blyth, E., Hobbs, S., Lopez-Sanchez, J. M., Mattia, F., Quaife, T., Quast, R., Rees, G., Wagner, W., 2019. Potential of G-Class/Hydroterra for the assessment of severe hydrological conditions. Noordwijk, the Netherlands.

Cao, Y., Yin, K., Alexander, D. E., Zhou, C., 2016. Using an extreme learning machine to predict the displacement of step-like landslides in relation to controlling factors. *Landslides*, 13(4), 725–736. `https://doi.org/10.1007/s10346-015-0596-z`.

Capderou, M., 2005. *Satellites, orbits and missions*. Springer-Verlag, Paris.

Carlà, T., Intrieri, E., Di Traglia, F., Nolesini, T., Gigli, G., Casagli, N., 2017. Guidelines on the use of inverse velocity method as a tool for setting alarm thresholds and forecasting landslides and structure collapses. *Landslides*, 14(2), 517–534. `https://doi.org/10.1007/s10346-016-0731-5`.

Carlà, T., Intrieri, E., Raspini, F., Bardi, F., Farina, P., Ferretti, A., Colombo, D., Novali, F., Casagli, N., 2019a. Perspectives on the prediction of catastrophic slope failures from satellite InSAR. *Scientific Reports*, 9(1). `https://doi.org/10.1038/s41598-019-50792-y`.

Carlà, T., Tofani, V., Lombardi, L., Raspini, F., Bianchini, S., Bertolo, D., Thuegaz, P., Casagli, N., 2019b. Combination of GNSS, satellite InSAR, and GBInSAR remote sensing monitoring to improve the understanding of a large landslide in high alpine environment. *Geomorphology*, 335, 62–75. `https://doi.org/10.1016/j.geomorph.2019.03.014`.

Cascini, L., Fornaro, G., Peduto, D., 2009. Analysis at medium scale of low-resolution DInSAR data in slow-moving landslide-affected areas. *ISPRS Journal of Photogrammetry and Remote Sensing*, 64(6), 598–611. `https://doi.org/10.1016/j.isprsjprs.2009.05.003`.

Cascini, L., Fornaro, G., Peduto, D., 2010. Advanced low- and full-resolution DInSAR map generation for slow-moving landslide analysis at different scales. *Engineering Geology*, 112(1-4), 29–42. `https://doi.org/10.1016/j.enggeo.2010.01.003`.

Cascini, L., Peduto, D., Pisciotta, G., Arena, L., Ferlisi, S., Fornaro, G., 2013. The combination of DInSAR and facility damage data for the updating of slow-moving landslide inventory maps at medium scale. *Natural Hazards and Earth System Sciences*, 13(6), 1527–1549. `https://doi.org/10.5194/nhess-13-1527-2013`.

Castagnetti, C., Bertacchini, E., Corsini, A., Rivola, R., 2014. A reliable methodology for monitoring unstable slopes: the multi-platform and multi-sensor approach. Amsterdam, Netherlands, 92450J. `https://doi.org/10.1117/12.2067407`.

CBS, 2022. Centraal Bureau voor de Statistiek: bestand bodemgebruik. `https://www.cbs.nl/nl-nl/dossier/nederland-regionaal/geografische-data/natuur-en-milieu/bestand-bodemgebruik`, accessed on 2022-11-18.

Cerqueira, V., Torgo, L., Soares, C., 2019. Machine learning vs statistical methods for time series forecasting: size matters. `https://doi.org/10.48550/ARXIV.1909.13316`.

Chacón, J., Irigaray, C., Fernández, T., El Hamdouni, R., 2006. Engineering geology maps: landslides and geographical information systems. *Bulletin of Engineering Geology and the Environment*, 65(4), 341–411. `https://doi.org/10.1007/s10064-006-0064-z`.

Chae, B.-G., Park, H.-J., Catani, F., Simoni, A., Berti, M., 2017. Landslide prediction, monitoring and early warning: a concise review of state-of-the-art. *Geosciences Journal*, 21(6), 1033–1070. `https://doi.org/10.1007/s12303-017-0034-4`.

Chang, L., Dollevoet, R. P. B. J., Hanssen, R. F., 2018. Monitoring line-infrastructure with multisensor SAR interferometry: products and performance assessment metrics. *IEEE Journal of Selected Topics in Applied Earth Observations and Remote Sensing*, 11(5), 1593–1605. `https://doi.org/10.1109/JSTARS.2018.2803074`.

Chatfield, C., 1993. Neural networks: forecasting breakthrough or passing fad? *International Journal of Forecasting*, 9(1), 1–3. `https://doi.org/10.1016/0169-2070(93)90043-M`.

Chen, H., Zeng, Z., 2013. Deformation prediction of landslide based on improved back-propagation neural network. *Cognitive Computation*, 5(1), 56–62. `https://doi.org/10.1007/s12559-012-9148-1`.

Ciampalini, A., Raspini, F., Bianchini, S., Frodella, W., Bardi, F., Lagomarsino, D., Di Traglia, F., Moretti, S., Proietti, C., Pagliara, P., Onori, R., Corazza, A., Duro, A., Basile, G., Casagli, N., 2015. Remote sensing as tool for development of landslide databases: the case of the Messina Province (Italy) geodatabase. *Geomorphology*, 249, 103–118. `https://doi.org/10.1016/j.geomorph.2015.01.029`.

Ciampalini, A., Raspini, F., Frodella, W., Bardi, F., Bianchini, S., Moretti, S., 2016. The effectiveness of high-resolution LiDAR data combined with PSInSAR data in landslide study. *Landslides*, 13(2), 399–410. `https://doi.org/10.1007/s10346-015-0663-5`.

Cigna, F., Bateson, L. B., Jordan, C. J., Dashwood, C., 2012. Feasibility of InSAR technologies for nationwide monitoring of geohazards in Great Britain. *Proceedings of the Remotesensing and Photogrammetry Society Conference 2012*, RSPSoc, University of Greenwich, London.

Cigna, F., Bateson, L., Colm, J., Dashwood, C., 2013. Nationwide monitoring of geohazards in Great Britain with InSAR: feasibility mapping based on ERS-1/2 and ENVISAT imagery. *2013 IEEE International Geoscience and Remote Sensing Symposium - IGARSS*, IEEE, Melbourne, Australia, 672–675. `https://doi.org/10.1109/IGARSS.2013.6721246`.

Claverie, M., Ju, J., Masek, J. G., Dungan, J. L., Vermote, E. F., Roger, J.-C., Skakun, S. V., Justice, C., 2018. The harmonized Landsat and Sentinel-2 surface reflectance data set. *Remote Sensing of Environment*, 219, 145–161. `https://doi.org/10.1016/j.rse.2018.09.002`.

COG, 2022. COG: Cloud Optimized GeoTIFF. `https://www.cogeo.org/`, accessed on 2022-11-09.

Colesanti, C., Ferretti, A., Prati, C., Rocca, F., 2003. Monitoring landslides and tectonic motions with the Permanent Scatterers technique. *Engineering Geology*, 68(1-2), 3–14. `https://doi.org/10.1016/S0013-7952(02)00195-3`.

Colesanti, C., Wasowski, J., 2006. Investigating landslides with space-borne Synthetic Aperture Radar (SAR) interferometry. *Engineering Geology*, 88(3-4), 173–199. https://doi.org/10.1016/j.enggeo.2006.09.013.

COMET, 2021. COMET-LiCS-portal. https://comet.nerc.ac.uk/comet-lics-portal/, accessed on 2022-11-16.

Connor, J., Martin, R., Atlas, L., 1994. Recurrent neural networks and robust time series prediction. *IEEE Transactions on Neural Networks*, 5(2), 240–254. https://doi.org/10.1109/72.279188.

Copernicus, 2018. The DIAS: user-friendly access to copernicus data and information. https://www.copernicus.eu/sites/default/files/Copernicus_DIAS_Factsheet_June2018.pdf, accessed on 2022-11-08.

Copernicus, 2022a. Copernicus atmosphere monitoring service. https://atmosphere.copernicus.eu/, accessed on 2022-11-08.

Copernicus, 2022b. Copernicus climate change service. https://climate.copernicus.eu/, accessed on 2022-11-08.

Copernicus, 2022c. Copernicus land monitoring service. https://land.copernicus.eu/, accessed on 2022-11-08.

Copernicus, 2022d. Copernicus marine service. https://marine.copernicus.eu/, accessed on 2022-11-08.

Copernicus, 2022e. Copernicus open access hub. https://scihub.copernicus.eu/, accessed on 2022-11-25.

Copernicus, 2022f. EGMS: European Ground Motion Service. https://land.copernicus.eu/pan-european/european-ground-motion-service, accessed on 2022-11-08.

Copernicus Climate Change Service, 2019. ERA5-Land hourly data from 2001 to present. https://cds.climate.copernicus.eu/doi/10.24381/cds.e2161bac, accessed on 2022-01-31. Dataset.

Copernicus Space Component Mission Management Team, 2019. Sentinel High Level Operations Plan (HLOP). https://sentinels.copernicus.eu/documents/247904/685154/Sentinel_High_Level_Operations_Plan, accessed on 2020-09-29. Technical report.

Cornillon, P., Gallagher, J., Sgouros, T., 2003. OPeNDAP: accessing data in a distributed, heterogeneous environment. *Data Science Journal*, 2, 164–174. https://doi.org/10.2481/dsj.2.164.

Corominas, J., Moya, J., Ledesma, A., Lloret, A., Gili, J. A., 2005. Prediction of ground displacements and velocities from groundwater level changes at the Vallcebre landslide (Eastern Pyrenees, Spain). *Landslides*, 2(2), 83–96. https://doi.org/10.1007/s10346-005-0049-1.

Corominas, J., van Westen, C., Frattini, P., Cascini, L., Malet, J.-P., Fotopoulou, S., Catani, F., Van Den Eeckhaut, M., Mavrouli, O., Agliardi, F., Pitilakis, K., Winter, M. G., Pastor, M., Ferlisi, S., Tofani, V., Hervás, J., Smith, J. T., 2013. Recommendations for the quantitative analysis of landslide risk. *Bulletin of Engineering Geology and the Environment.* `https://doi.org/10.1007/s10064-013-0538-8`.

Corsini, A., Castagnetti, C., Bertacchini, E., Rivola, R., Ronchetti, F., Capra, A., 2013. Integrating airborne and multi-temporal long-range terrestrial laser scanning with total station measurements for mapping and monitoring a compound slow moving rock slide: monitoring rock slides by multi-temporal terrestrial laser scanning. *Earth Surface Processes and Landforms*, 38(11), 1330–1338. `https://doi.org/10.1002/esp.3445`.

Corsini, A., Farina, P., Antonello, G., Barbieri, M., Casagli, N., Coren, F., Guerri, L., Ronchetti, F., Sterzai, P., Tarchi, D., 2006. Space-borne and ground-based SAR interferometry as tools for landslide hazard management in civil protection. *International Journal of Remote Sensing*, 27(12), 2351–2369. `https://doi.org/10.1080/01431160600554405`.

Crippen, R., Buckley, S., Agram, P., Belz, E., Gurrola, E., Hensley, S., Kobrick, M., Lavalle, M., Martin, J., Neumann, M., Nguyen, Q., Rosen, P., Shimada, J., Simard, M., Tung, W., 2016. NASADEM Global Elevation Model: Methods and Progress. *ISPRS - International Archives of the Photogrammetry, Remote Sensing and Spatial Information Sciences*, XLI-B4, 125–128. `https://doi.org/10.5194/isprsarchives-XLI-B4-125-2016`.

Crosetto, M., Solari, L., Mróz, M., Balasis-Levinsen, J., Casagli, N., Frei, M., Oyen, A., Moldestad, D. A., Bateson, L., Guerrieri, L., Comerci, V., Andersen, H. S., 2020. The evolution of wide-area DInSAR: from regional and national services to the European ground motion service. *Remote Sensing*, 12(12), 2043. `https://doi.org/10.3390/rs12122043`.

Crosta, G. B., di Prisco, C., Frattini, P., Frigerio, G., Castellanza, R., Agliardi, F., 2014. Chasing a complete understanding of the triggering mechanisms of a large rapidly evolving rockslide. *Landslides*, 11(5), 747–764. `https://doi.org/10.1007/s10346-013-0433-1`.

Crosta, G., Frattini, P., Agliardi, F., 2013. Deep seated gravitational slope deformations in the European Alps. *Tectonophysics*, 605, 13–33. `https://doi.org/10.1016/j.tecto.2013.04.028`.

Cruden, D. M., 1991. A simple definition of a landslide. *Bulletin of the International Association of Engineering Geology*, 43(1), 27–29. `https://doi.org/10.1007/BF02590167`.

Czikhardt, R., Papco, J., Bakon, M., Liscak, P., Ondrejka, P., Zlocha, M., 2017. Ground stability monitoring of undermined and landslide prone areas by means of Sentinel-1 multi-temporal InSAR, case study from Slovakia. *Geosciences*, 7(3), 87. `https://doi.org/10.3390/geosciences7030087`.

Damen, M., Micu, M., Zumpano, V., van Westen, C. J., Sijmons, K., Balteanu, D., 2014. Landslide mapping and interpretation: implications for landslide susceptibility analysis in discontinuous data environment. *Proceedings of the International Conference on Analysis and Management of Changing Risks for Natural Hazards*, Padua, Italy.

de Ferranti, J., 2014. Viewfinder panoramas. `http://viewfinderpanoramas.org/dem3.html`, accessed on 2019-05-29.

DeepCube, 2021. DeepCube H2020. `https://deepcube-h2020.eu/`, accessed on 2022-11-16.

Del Soldato, M., Solari, L., Novellino, A., Monserrat, O., Raspini, F., 2021. A new set of tools for the generation of InSAR visibility maps over wide areas. *Geosciences*, 11(6), 229. `https://doi.org/10.3390/geosciences11060229`.

Delacourt, C., Allemand, P., Berthier, E., Raucoules, D., Casson, B., Grandjean, P., Pambrun, C., Varel, E., 2007. Remote-sensing techniques for analysing landslide kinematics: a review. *Bulletin de la Societe Geologique de France*, 178(2), 89–100. `https://doi.org/10.2113/gssgfbull.178.2.89`.

Delgado, J., Vicente, F., García-Tortosa, F., Alfaro, P., Estévez, A., Lopez-Sanchez, J., Tomás, R., Mallorquí, J., 2011. A deep seated compound rotational rock slide and rock spread in SE Spain: structural control and DInSAR monitoring. *Geomorphology*, 129(3-4), 252–262. `https://doi.org/10.1016/j.geomorph.2011.02.019`.

den Ouden, O., 2022. A bird's-eye view on infrasound: High-resolution methods to unravel the ambient microbarom wavefield. PhD thesis, Delft University of Technology.

den Ouden, O. F. C., Assink, J. D., Oudshoorn, C. D., Filippi, D., Evers, L. G., 2021. The INFRA-EAR: a low-cost mobile multidisciplinary measurement platform for monitoring geophysical parameters. *Atmospheric Measurement Techniques*, 14(5), 3301–3317. `https://doi.org/10.5194/amt-14-3301-2021`.

Deng, L., Smith, A., Dixon, N., Yuan, H., 2021. Machine learning prediction of landslide deformation behaviour using acoustic emission and rainfall measurements. *Engineering Geology*, 293, 106315. `https://doi.org/10.1016/j.enggeo.2021.106315`.

Devys, E., Habermann, T., Heazel, C., Lott, R., Rouault, E., 2019. OGC GeoTIFF standard. `http://docs.opengeospatial.org/is/19-008r4/19-008r4.html`, accessed on 2022-11-09.

Dewitte, O., Jasselette, J.-C., Cornet, Y., Van Den Eeckhaut, M., Collignon, A., Poesen, J., Demoulin, A., 2008. Tracking landslide displacements by multi-temporal DTMs: a combined aerial stereophotogrammetric and LiDAR approach in western Belgium. *Engineering Geology*, 99(1-2), 11–22. `https://doi.org/10.1016/j.enggeo.2008.02.006`.

Di Sabatino, S., others, 2017. Horizon 2020 Proposal: "*Op*en-ai*r* labor*a*tories for *n*ature-base*d* sol*u*tions to *m*anage hydro-meteo risks" (acronym: OPERANDUM).

Dobrovolny, E., 1971. Landslide susceptibility in and near anchorage as interpreted from topographic and geologic maps, in the great Alaska earthquake of 1964. Technical Report 1603, US Geological Survey.

Donchyts, G., Baart, F., Winsemius, H., Gorelick, N., Kwadijk, J., van de Giesen, N., 2016. Earth's surface water change over the past 30 years. *Nature Climate Change*, 6(9), 810–813. `https://doi.org/10.1038/nclimate3111`.

Dong, J., Zhang, L., Tang, M., Liao, M., Xu, Q., Gong, J., Ao, M., 2018. Mapping landslide surface displacements with time series SAR interferometry by combining persistent and distributed scatterers: a case study of Jiaju landslide in Danba, China. *Remote Sensing of Environment*, 205, 180–198. `https://doi.org/10.1016/j.rse.2017.11.022`.

Du, J., Yin, K., Lacasse, S., 2013. Displacement prediction in colluvial landslides, Three Gorges Reservoir, China. *Landslides*, 10(2), 203–218. `https://doi.org/10.1007/s10346-012-0326-8`.

Duscher, K., Günther, A., Richts, A., Clos, P., Philipp, U., Struckmeier, W., 2015. The GIS layers of the "International Hydrogeological Map of Europe 1:1,500,000" in a vector format. *Hydrogeology Journal*, 23(8), 1867–1875. `https://doi.org/10.1007/s10040-015-1296-4`.

Dwyer, J. L., Roy, D. P., Sauer, B., Jenkerson, C. B., Zhang, H. K., Lymburner, L., 2018. Analysis Ready Data: enabling analysis of the Landsat archive. *Remote Sensing*, 10(9), 1363. `https://doi.org/10.3390/rs10091363`.

Eaton, B., Gregory, J., Drach, B., Taylor, K., Hankin, S., Blower, J., Caron, J., Signell, R., Bentley, P., Rappa, G., Höck, H., Pamment, A., Juckes, M., Raspaud, M., 2017. NetCDF Climate and Forecast (CF) metadata conventions. Technical report.

Ellipsis, 2022. Ellipsis Drive. `https://ellipsis-drive.com/`, accessed on 2022-11-16.

Elvidge, C., Baugh, K., Kihn, E., Kroehl, H., Davis, E., 1997. Mapping city lights with nighttime data from the DMSP Operational Linescan System. *Photogrammetric Engineering and Remote Sensing*, 63(6), 727–734.

Elvidge, C. D., Baugh, K. E., Dietz, J. B., Bland, T., Sutton, P. C., Kroehl, H. W., 1999. Radiance calibration of DMSP-OLS low-light imaging data of human settlements. *Remote Sensing of Environment*, 68(1), 77–88. `https://doi.org/10.1016/S0034-4257(98)00098-4`.

Entekhabi, D., Njoku, E. G., O'Neill, P. E., Kellogg, K. H., Crow, W. T., Edelstein, W. N., Entin, J. K., Goodman, S. D., Jackson, T. J., Johnson, J., Kimball, J., Piepmeier, J. R., Koster, R. D., Martin, N., McDonald, K. C., Moghaddam, M., Moran, S., Reichle, R., Shi, J. C., Spencer, M. W., Thurman, S. W., Tsang, L., Van Zyl, J., 2010. The Soil Moisture Active Passive (SMAP) mission. *Proceedings of the IEEE*, 98(5), 704–716. `https://doi.org/10.1109/JPROC.2010.2043918`.

EODC, 2022. EODC: Earth Observation Data Centre for water resources monitoring. `https://eodc.eu/`, accessed on 2022-11-17.

EOX, 2022. Euro data cube. `https://eurodatacube.com/`, accessed on 2022-11-30.

Erskine, R. H., Green, T. R., Ramirez, J. A., MacDonald, L. H., 2007. Digital elevation accuracy and grid cell size: effects on estimated terrain attributes. *Soil Science Society of America Journal*, 71(4), 1371–1380. `https://doi.org/10.2136/sssaj2005.0142`.

ESA, 2022a. Existing/planned collaborative ground segment. `https://sentinel.esa.int/web/sentinel/missions/collaborative/existing-planned`, accessed on 2022-11-09.

ESA, 2022b. Sen2Cor. `https://step.esa.int/main/snap-supported-plugins/sen2cor/`, accessed on 2022-11-09.

ESA, 2022c. Sentinel-1 ARD Normalised Radar Backscatter (NRB) product. `https://sentinels.copernicus.eu/web/sentinel/sentinel-1-ard-normalised-radar-backscatter-nrb-product`, accessed on 2022-09-16.

EU, 2007. Directive 2007/2/EC of the European Parliament and of the Council of 14 March 2007 establishing an Infrastructure for Spatial Information in the European Community (INSPIRE). `https://eur-lex.europa.eu/eli/dir/2007/2/2019-06-26`, accessed on 2022-11-30.

EuroGeographics, 2022. EuroGeographics. `https://eurogeographics.org/`, accessed on 2022-11-09.

Fahrland, E., 2020. Copernicus digital elevation model. `https://spacedata.copernicus.eu/documents/20126/0/GEO1988-CopernicusDEM-SPE-002_ProductHandbook_I1.00(1).pdf`, accessed on 2021-01-29. Product handbook.

Farr, T. G., Rosen, P. A., Caro, E., Crippen, R., Duren, R., Hensley, S., Kobrick, M., Paller, M., Rodriguez, E., Roth, L., Seal, D., Shaffer, S., Shimada, J., Umland, J., Werner, M., Oskin, M., Burbank, D., Alsdorf, D., 2007. The Shuttle radar topography mission. *Reviews of Geophysics*, 45(2). `https://doi.org/10.1029/2005RG000183`.

Fell, R., Corominas, J., Bonnard, C., Cascini, L., Leroi, E., Savage, W. Z., 2008. Guidelines for landslide susceptibility, hazard and risk zoning for land-use planning. *Engineering Geology*, 102(3-4), 99–111. `https://doi.org/10.1016/j.enggeo.2008.03.014`.

Ferretti, A., Prati, C., Rocca, F., 2001. Permanent scatterers in SAR interferometry. *IEEE Transactions on Geoscience and Remote Sensing*, 39(1), 8–20. `https://doi.org/10.1109/36.898661`.

Frantz, D., 2019. FORCE—Landsat + Sentinel-2 analysis ready data and beyond. *Remote Sensing*, 11(9), 1124. `https://doi.org/10.3390/rs11091124`.

Frantz, D., Janz, A., Stefan Ernst, 2022. FORCE: Framework for Operational Radiometric Correction for Environmental monitoring. `https://github.com/davidfrantz/force`, accessed on 2022-11-09.

Frattini, P., Crosta, G. B., Rossini, M., Allievi, J., 2018. Activity and kinematic behaviour of deep-seated landslides from PS-InSAR displacement rate measurements. *Landslides*, 15(6), 1053–1070. `https://doi.org/10.1007/s10346-017-0940-6`.

Frey, H., Paul, F., 2012. On the suitability of the SRTM DEM and ASTER GDEM for the compilation of topographic parameters in glacier inventories. *International Journal of Applied Earth Observation and Geoinformation*, 18, 480–490. `https://doi.org/10.1016/j.jag.2011.09.020`.

Froude, M. J., Petley, D. N., 2018. Global fatal landslide occurrence from 2004 to 2016. *Natural Hazards and Earth System Sciences*, 18(8), 2161–2181. `https://doi.org/10.5194/nhess-18-2161-2018`.

GDAL/OGR contributors, 2020. GDAL/OGR Geospatial Data Abstraction software Library. `https://gdal.org`. Software package.

Geoportti, 2022. GeoCubes Finland. `https://vm0160.kaj.pouta.csc.fi/geocubes/`, accessed on 2022-11-17.

Gholamy, A., Kreinovich, V., Kosheleva, O., 2018. Why 70/30 or 80/20 relation between training and testing sets: a pedagogical explanation. *Departmental Technical Reports (CS)*.

Gillies, S., others, 2013. Rasterio: geospatial raster I/O for Python programmers. `https://github.com/mapbox/rasterio`. Software package.

Giuliani, G., Camara, G., Killough, B., Minchin, S., 2019a. Earth observation open science: enhancing reproducible science using data cubes. *Data*, 4(4), 147. `https://doi.org/10.3390/data4040147`.

Giuliani, G., Chatenoux, B., Piller, T., Moser, F., Lacroix, P., 2020. Data Cube On Demand (DCOD): generating an earth observation data cube anywhere in the world. *International Journal of Applied Earth Observation and Geoinformation*, 87, 102035. `https://doi.org/10.1016/j.jag.2019.102035`.

Giuliani, G., Masó, J., Mazzetti, P., Nativi, S., Zabala, A., 2019b. Paving the Way to Increased Interoperability of Earth Observations Data Cubes. *Data*, 4(3), 113. `https://doi.org/10.3390/data4030113`.

Glade, T., 2000. Modelling landslide-triggering rainfalls in different regions of New Zealand - the soil water status model. *Zeitschrift für Geomorphologie. Supplementband*, 63–84.

Godt, J. W., Baum, R. L., Chleborad, A. F., 2006. Rainfall characteristics for shallow landsliding in Seattle, Washington, USA. *Earth Surface Processes and Landforms*, 31(1), 97–110. `https://doi.org/10.1002/esp.1237`.

Gomes, V., Queiroz, G., Ferreira, K., 2020. An overview of platforms for big earth observation data management and analysis. *Remote Sensing*, 12(8), 1253. `https://doi.org/10.3390/rs12081253`.

Goodchild, M. F., 2001. Metrics of scale in remote sensing and GIS. *International Journal of Applied Earth Observation and Geoinformation*, 3(2), 114–120. `https://doi.org/10.1016/S0303-2434(01)85002-9`.

Google, 2021a. Google Earth Engine, ee.Algorithms.Terrain. `https://developers.google.com/earth-engine/apidocs/ee-algorithms-terrain`, accessed on 2021-03-30.

Google, 2021b. Sentinel-1 algorithms. `https://developers.google.com/earth-engine/guides/sentinel1`, accessed on 2021-03-30.

Gorelick, N., Hancher, M., Dixon, M., Ilyushchenko, S., Thau, D., Moore, R., 2017. Google Earth Engine: Planetary-scale geospatial analysis for everyone. *Remote Sensing of Environment*, 202, 18–27. `https://doi.org/10.1016/j.rse.2017.06.031`.

Grazia Castriotta, A., 2022. 2021 Copernicus Sentinel data access annual report. `https://scihub.copernicus.eu/twiki/pub/SciHubWebPortal/AnnualReport2021/COPE-SERCO-RP-22-1312_-_Sentinel_Data_Access_Annual_Report_Y2021_merged_v1.1.pdf`, accessed on 2022-11-09.

Grohmann, C. H., 2015. Effects of spatial resolution on slope and aspect derivation for regional-scale analysis. *Computers & Geosciences*, 77, 111–117. `https://doi.org/10.1016/j.cageo.2015.02.003`.

Grohmann, C. H., 2018. Evaluation of TanDEM-X DEMs on selected Brazilian sites: comparison with SRTM, ASTER GDEM and ALOS AW3D30. *Remote Sensing of Environment*, 212, 121–133. `https://doi.org/10.1016/j.rse.2018.04.043`.

Guzzetti, F., Carrara, A., Cardinali, M., Reichenbach, P., 1999. Landslide hazard evaluation: a review of current techniques and their application in a multi-scale study, Central Italy. *Geomorphology*, 31(1), 181–216.

Guzzetti, F., Gariano, S. L., Peruccacci, S., Brunetti, M. T., Marchesini, I., Rossi, M., Melillo, M., 2020. Geographical landslide early warning systems. *Earth-Science Reviews*, 200, 102973. `https://doi.org/10.1016/j.earscirev.2019.102973`.

Günther, A., van den Eeckhaut, M., Malet, J.-P., Reichenbach, P., Hervás, J., 2014. Climate-physiographically differentiated pan-European landslide susceptibility assessment using spatial multi-criteria evaluation and transnational landslide information. *Geomorphology*, 224, 69–85. `https://doi.org/10.1016/j.geomorph.2014.07.011`.

Hansen, M. C., Loveland, T. R., 2012. A review of large area monitoring of land cover change using Landsat data. *Remote Sensing of Environment*, 122, 66–74. `https://doi.org/10.1016/j.rse.2011.08.024`.

Hansen, M. C., Potapov, P. V., Moore, R., Hancher, M., Turubanova, S. A., Tyukavina, A., Thau, D., Stehman, S. V., Goetz, S. J., Loveland, T. R., Kommareddy, A., Egorov, A., Chini, L., Justice, C. O., Townshend, J. R. G., 2013. High-resolution global maps of 21st-century forest cover change. *Science*, 342(6160), 850–853. `https://doi.org/10.1126/science.1244693`.

Hanssen, R. F., 2001. *Radar interferometry: data interpretation and error analysis*. Remote Sensing and Digital Image Processing, 2, Springer Netherlands, Dordrecht.

Haque, U., Blum, P., da Silva, P. F., Andersen, P., Pilz, J., Chalov, S. R., Malet, J.-P., Auflič, M. J., Andres, N., Poyiadji, E., Lamas, P. C., Zhang, W., Peshevski, I., Pétursson, H. G., Kurt, T., Dobrev, N., García-Davalillo, J. C., Halkia, M., Ferri, S., Gaprindashvili, G., Engström, J., Keellings, D., 2016. Fatal landslides in Europe. *Landslides*, 13(6), 1545–1554. `https://doi.org/10.1007/s10346-016-0689-3`.

Harris, C. R., Millman, K. J., van der Walt, S. J., Gommers, R., Virtanen, P., Cournapeau, D., Wieser, E., Taylor, J., Berg, S., Smith, N. J., Kern, R., Picus, M., Hoyer, S., van Kerkwijk, M. H., Brett, M., Haldane, A., del Río, J. F., Wiebe, M., Peterson, P., Gérard-Marchant, P., Sheppard, K., Reddy, T., Weckesser, W., Abbasi, H., Gohlke, C., Oliphant, T. E., 2020. Array programming with NumPy. *Nature*, 585(7825), 357–362. `https://doi.org/10.1038/s41586-020-2649-2`.

Hartke, S. H., Wright, D. B., Kirschbaum, D. B., Stanley, T. A., Li, Z., 2020. Incorporation of satellite precipitation uncertainty in a landslide hazard nowcasting system. *Journal of Hydrometeorology*, 21(8), 1741–1759. `https://doi.org/10.1175/JHM-D-19-0295.1`.

Hayakawa, Y. S., Oguchi, T., Lin, Z., 2008. Comparison of new and existing global digital elevation models: ASTER G-DEM and SRTM-3. *Geophysical Research Letters*, 35(17). `https://doi.org/10.1029/2008GL035036`.

Heggen, R. J., 2001. Normalized antecedent precipitation index. *Journal of Hydrologic Engineering*, 6(5), 377–381. `https://doi.org/10.1061/(ASCE)1084-0699(2001)6:5(377)`.

Herrera, G., Gutiérrez, F., García-Davalillo, J., Guerrero, J., Notti, D., Galve, J., Fernández-Merodo, J., Cooksley, G., 2013. Multi-sensor advanced DInSAR monitoring of very slow landslides: the Tena Valley case study (Central Spanish Pyrenees). *Remote Sensing of Environment*, 128, 31–43. `https://doi.org/10.1016/j.rse.2012.09.020`.

Herrera, G., Mateos, R. M., García-Davalillo, J. C., Grandjean, G., Poyiadji, E., Maftei, R., Filipciuc, T.-C., Jemec Auflič, M., Jež, J., Podolszki, L., Trigila, A., Iadanza, C., Raetzo, H., Kociu, A., Przyłucka, M., Kułak, M., Sheehy, M., Pellicer, X. M., McKeown, C., Ryan, G., Kopačková, V., Frei, M., Kuhn, D., Hermanns, R. L., Koulermou, N., Smith, C. A., Engdahl, M., Buxó, P., Gonzalez, M., Dashwood, C., Reeves, H., Cigna, F., Liščák, P., Pauditš, P., Mikulėnas, V., Demir, V., Raha, M., Quental, L., Sandić, C., Fusi, B., Jensen, O. A., 2018. Landslide databases in the geological surveys of Europe. *Landslides*, 15(2), 359–379. `https://doi.org/10.1007/s10346-017-0902-z`.

Hill, T., Marquez, L., O'Connor, M., Remus, W., 1994. Artificial neural network models for forecasting and decision making. *International Journal of Forecasting*, 10(1), 5–15. `https://doi.org/10.1016/0169-2070(94)90045-0`.

Hilley, G. E., Bürgmann, R., Ferretti, A., Novali, F., Rocca, F., 2004. Dynamics of slow-moving landslides from permanent scatterer analysis. *Science*, 304(5679), 1952–1955. `https://doi.org/10.1126/science.1098821`.

Hirt, C., Filmer, M. S., Featherstone, W. E., 2010. Comparison and validation of the recent freely available ASTER-GDEM ver1, SRTM ver4.1 and GEODATA DEM-9S ver3 digital elevation models over Australia. *Australian Journal of Earth Sciences*, 57(3), 337–347. `https://doi.org/10.1080/08120091003677553`.

Hochreiter, S., 1998. The vanishing gradient problem during learning recurrent neural nets and problem solutions. *International Journal of Uncertainty, Fuzziness and Knowledge-Based Systems*, 06(02), 107–116. `https://doi.org/10.1142/S0218488598000094`.

Hochreiter, S., Schmidhuber, J., 1997. Long short-term memory. *Neural Computation*, 9(8), 1735–1780. `https://doi.org/10.1162/neco.1997.9.8.1735`.

Hooper, A., 2008. A multi-temporal InSAR method incorporating both persistent scatterer and small baseline approaches. *Geophysical Research Letters*, 35(16). `https://doi.org/https://doi.org/10.1029/2008GL034654`.

Horn, B., 1981. Hill shading and the reflectance map. *Proceedings of the IEEE*, 69(1), 14–47. `https://doi.org/10.1109/PROC.1981.11918`.

Hornik, K., Stinchcombe, M., White, H., 1989. Multilayer feedforward networks are universal approximators. *Neural Networks*, 2(5), 359–366. `https://doi.org/10.1016/0893-6080(89)90020-8`.

Hou, A. Y., Kakar, R. K., Neeck, S., Azarbarzin, A. A., Kummerow, C. D., Kojima, M., Oki, R., Nakamura, K., Iguchi, T., 2014. The Global Precipitation Measurement mission. *Bulletin of the American Meteorological Society*, 95(5), 701–722. `https://doi.org/10.1175/BAMS-D-13-00164.1`.

Huabin, W., Gangjun, L., Weiya, X., Gonghui, W., 2005. GIS-based landslide hazard assessment: an overview. *Progress in Physical Geography: Earth and Environment*, 29(4), 548–567. `https://doi.org/10.1191/0309133305pp462ra`.

Huang, F., Huang, J., Jiang, S., Zhou, C., 2017. Landslide displacement prediction based on multivariate chaotic model and extreme learning machine. *Engineering Geology*, 218, 173–186. `https://doi.org/10.1016/j.enggeo.2017.01.016`.

Huang, R., Jiang, L., Shen, X., Dong, Z., Zhou, Q., Yang, B., Wang, H., 2019. An efficient method of monitoring slow-moving landslides with long-range terrestrial laser scanning: a case study of the Dashu landslide in the Three Gorges Reservoir Region, China. *Landslides*, 16(4), 839–855. `https://doi.org/10.1007/s10346-018-1118-6`.

Huffman, G., Stocker, E., Bolvin, D., Nelkin, E., Jackson, T., 2019. GPM IMERG final precipitation L3 Half Hourly 0.1 degree x 0.1 degree V05. `https://doi.org/10.5067/GPM/IMERG/3B-HH/06`, accessed on 2022-01-26. Dataset.

Hungr, O., Leroueil, S., Picarelli, L., 2014. The Varnes classification of landslide types, an update. *Landslides*, 11(2), 167–194. `https://doi.org/10.1007/s10346-013-0436-y`.

Hunter, J. D., 2007. Matplotlib: a 2D graphics environment. *Computing in Science & Engineering*, 9(3), 90–95. `https://doi.org/10.1109/MCSE.2007.55`.

Husár, L., Švaral, P., Janák, J., 2017. About the geometry of the Earth geodetic reference surfaces. *Journal of Geometry and Physics*, 120, 192–207. `https://doi.org/10.1016/j.geomphys.2017.05.016`.

International Consortium on Landslides, 2019. Kyoto 2020 commitment for global promotion of understanding and reducing landslide disaster risk. `https://wlf5.iplhq.org/concept-of-kyoto-2020-commitment/`.

Intrieri, E., Carlà, T., Gigli, G., 2019. Forecasting the time of failure of landslides at slope-scale: a literature review. *Earth-Science Reviews*, 193, 333–349. `https://doi.org/10.1016/j.earscirev.2019.03.019`.

Intrieri, E., Frodella, W., Raspini, F., Bardi, F., Tofani, V., 2020. Using satellite interferometry to infer landslide sliding surface depth and geometry. *Remote Sensing*, 12(9), 1462. `https://doi.org/10.3390/rs12091462`.

Intrieri, E., Gigli, G., Casagli, N., Nadim, F., 2013. Brief communication "landslide early warning system: toolbox and general concepts". *Natural Hazards and Earth System Sciences*, 13(1), 85–90. `https://doi.org/10.5194/nhess-13-85-2013`.

Intrieri, E., Raspini, F., Fumagalli, A., Lu, P., Del Conte, S., Farina, P., Allievi, J., Ferretti, A., Casagli, N., 2018. The Maoxian landslide as seen from space: detecting precursors of failure with Sentinel-1 data. *Landslides*, 15(1), 123–133. `https://doi.org/10.1007/s10346-017-0915-7`.

Jaboyedoff, M., Oppikofer, T., Abellán, A., Derron, M.-H., Loye, A., Metzger, R., Pedrazzini, A., 2012. Use of LiDAR in landslide investigations: a review. *Natural Hazards*, 61(1), 5–28. `https://doi.org/10.1007/s11069-010-9634-2`.

Jacobs University, Rasdaman, 2020. EarthServer. `https://www.earthserver.eu/`, accessed on 2022-11-15.

Jain, A., Jianchang Mao, Mohiuddin, K., 1996. Artificial neural networks: a tutorial. *Computer*, 29(3), 31–44. `https://doi.org/10.1109/2.485891`.

Jamalinia, E., Tehrani, F. S., Steele-Dunne, S. C., Vardon, P. J., 2021. A data-driven surrogate approach for the temporal stability forecasting of vegetation covered dikes. *Water*, 13(1), 107. `https://doi.org/10.3390/w13010107`.

Janssen, H., Janssen, S., Knapen, M., Meijninger, W., van Randen, Y., la Riviere, I., Roerink, G., 2018. AgroDataCube: a big open data collection for agri-food applications. Technical report, Wageningen Environmental Research. Dataset.

Japan Aerospace Exploration Agency, Earth Observation Research Center, 2019. ALOS Global Digital Surface Model (DSM) product description. Technical report, Japan Aerospace Exploration Agency (JAXA).

Jia, X., Karpatne, A., Willard, J., Steinbach, M., Read, J., Hanson, P. C., Dugan, H. A., Kumar, V., 2018. Physics guided recurrent neural networks for modeling dynamical systems: application to monitoring water temperature and quality in lakes. *arXiv:1810.02880 [cs, stat]*. arXiv: 1810.02880.

Jiang, P., Chen, J., 2016. Displacement prediction of landslide based on generalized regression neural networks with k-fold cross-validation. *Neurocomputing*, 198, 40–47. `https://doi.org/10.1016/j.neucom.2015.08.118`.

Jordahl, K., van den Bossche, J., Fleischmann, M., Wasserman, J., McBride, J., Gerard, J., Tratner, J., Perry, M., Garcia Badaracco, A., Farmer, C., Geir Arne Hjelle, Snow, A. D., Cochran, M., Gillies, S., Culbertson, L., Bartos, M., Eubank, N., maxalbert, Bilogur, A., Rey, S., Ren, C., Arribas-Bel, D., Wasser, L., Wolf, L. J., Journois, M., Wilson, J., Greenhall, A., Holdgraf, C., Filipe, Leblanc, F., 2020. GeoPandas. `https://doi.org/10.5281/zenodo.2585848`, accessed on 2020-11-17. Software package.

Kalia, A. C., 2022. Landslide activity detection based on Sentinel-1 PSI datasets of the Ground Motion Service Germany—the Trittenheim case study. *Landslides*. `https://doi.org/10.1007/s10346-022-01958-9`.

Kalman, R. E., 1960. A new approach to linear filtering and prediction problems. *Journal of Basic Engineering*, 82(1), 35–45. `https://doi.org/10.1115/1.3662552`.

Kanungo, D., Arora, M., Sarkar, S., Gupta, R., 2009. Landslide Susceptibility Zonation (LSZ) mapping – a review. *Journal of South Asia Disaster Studies*, 2(1), 81–105.

Karpatne, A., Watkins, W., Read, J., Kumar, V., 2017. Physics-Guided Neural Networks (PGNN): an application in lake temperature modeling. *arXiv:1710.11431 [physics, stat]*. arXiv: 1710.11431.

Kathmann, H. S., van Natijne, A. L., Lindenbergh, R. C., 2022. Probabilistic vegetation transitions in dunes by combining spectral and LiDAR data. *The International Archives of the Photogrammetry, Remote Sensing and Spatial Information Sciences*, XLIII-B2-2022, 1033–1040. `https://doi.org/10.5194/isprs-archives-XLIII-B2-2022-1033-2022`.

Keefer, D. K., 1984. Landslides caused by earthquakes. *GSA Bulletin*, 95(4), 406–421.

Kellndorfer, J., Cartus, O., Lavalle, M., Magnard, C., Milillo, P., Oveisgharan, S., Osmanoglu, B., Rosen, P. A., Wegmüller, U., 2022. Global seasonal Sentinel-1 interferometric coherence and backscatter data set. *Scientific Data*, 9(1), 73. `https://doi.org/10.1038/s41597-022-01189-6`.

Khan, S., Kirschbaum, D. B., Stanley, T. A., Amatya, P. M., Emberson, R. A., 2022. Global landslide forecasting system for hazard assessment and situational awareness. *Frontiers in Earth Science*, 10, 878996. `https://doi.org/10.3389/feart.2022.878996`.

Killough, B., 2018. Overview of the open data cube initiative. *IGARSS 2018 - 2018 IEEE International Geoscience and Remote Sensing Symposium*, IEEE, Valencia, 8629–8632. `https://doi.org/10.1109/IGARSS.2018.8517694`.

Kingma, D. P., Ba, J., 2017. Adam: a method for stochastic optimization. arXiv, San Diego, United States of America. `https://doi.org/https://doi.org/10.48550/arXiv.1412.6980`.

Kirchner, J. W., 2006. Getting the right answers for the right reasons: linking measurements, analyses, and models to advance the science of hydrology. *Water Resources Research*, 42(3). `https://doi.org/10.1029/2005WR004362`.

Kirchner, S., 2020. Interference with subsea cables: an arctic perspective. *Cybersecurity and Resilience in the Arctic*, 190–199. `https://doi.org/10.3233/NICSP200048`.

Kirschbaum, D. B., Adler, R., Hong, Y., Hill, S., Lerner-Lam, A., 2010. A global landslide catalog for hazard applications: method, results, and limitations. *Natural Hazards*, 52(3), 561–575. `https://doi.org/10.1007/s11069-009-9401-4`.

Kirschbaum, D., Stanley, T., 2018. Satellite-based assessment of rainfall-triggered landslide hazard for situational awareness. *Earth's Future*, 6(3), 505–523. `https://doi.org/10.1002/2017EF000715`.

Kirschbaum, D., Stanley, T., Zhou, Y., 2015. Spatial and temporal analysis of a global landslide catalog. *Geomorphology*, 249, 4–15. `https://doi.org/10.1016/j.geomorph.2015.03.016`.

Kohler, M. A., Linsley, R. K., 1951. *Predicting the runoff from storm rainfall.* 30, US Department of Commerce, Weather Bureau.

Komac, M., Holley, R., Mahapatra, P., van der Marel, H., Bavec, M., 2015. Coupling of GPS/GNSS and radar interferometric data for a 3D surface displacement monitoring of landslides. *Landslides*, 12(2), 241–257. `https://doi.org/10.1007/s10346-014-0482-0`.

Krkač, M., Bernat Gazibara, S., Arbanas, Z., Sečanj, M., Mihalić Arbanas, S., 2020. A comparative study of random forests and multiple linear regression in the prediction of landslide velocity. *Landslides*, 17(11), 2515–2531. `https://doi.org/10.1007/s10346-020-01476-6`.

Krkač, M., Špoljarić, D., Bernat, S., Arbanas, S. M., 2017. Method for prediction of landslide movements based on random forests. *Landslides*, 14(3), 947–960. `https://doi.org/10.1007/s10346-016-0761-z`.

Lacroix, P., Bièvre, G., Pathier, E., Kniess, U., Jongmans, D., 2018. Use of Sentinel-2 images for the detection of precursory motions before landslide failures. *Remote Sensing of Environment*, 215, 507–516. `https://doi.org/10.1016/j.rse.2018.03.042`.

Lam, S. K., Pitrou, A., Seibert, S., 2015. Numba: a LLVM-based Python JIT compiler. *Proceedings of the Second Workshop on the LLVM Compiler Infrastructure in HPC*, LLVM '15, Association for Computing Machinery, Austin, Texas, 1–6. `https://doi.org/10.1145/2833157.2833162`.

Lauknes, T., Piyush Shanker, A., Dehls, J., Zebker, H., Henderson, I., Larsen, Y., 2010. Detailed rockslide mapping in northern Norway with small baseline and persistent scatterer interferometric SAR time series methods. *Remote Sensing of Environment*, 114(9), 2097–2109. `https://doi.org/10.1016/j.rse.2010.04.015`.

Lazecký, M., Spaans, K., González, P. J., Maghsoudi, Y., Morishita, Y., Albino, F., Elliott, J., Greenall, N., Hatton, E., Hooper, A., Juncu, D., McDougall, A., Walters, R. J., Watson, C. S., Weiss, J. R., Wright, T. J., 2020. LiCSAR: an automatic InSAR tool for measuring and monitoring tectonic and volcanic activity. *Remote Sensing*, 12(15), 2430. `https://doi.org/10.3390/rs12152430`.

Le, T. T. T., Kawagoe, S., 2018. Impact of the landslide for a relationship between rainfall condition and land cover in North Vietnam. *Journal of Geological Resource and Engineering*, 6(6). `https://doi.org/10.17265/2328-2193/2018.06.002`.

Lehto, L., Kähkönen, J., Oksanen, J., Sarjakoski, T., 2019. Flexible access to a harmonised multi-resolution raster geodata storage in the cloud. *GEOProcessing 2019: International Conference on Advanced Geographic Information Systems, Applications, and Services*, International Conference on Advanced Geographic Information Systems, Applications, and Services, IARIA, 26–28.

Lesparre, J., Huisman, L., Alberts, B., 2019. RDNAPTRANS™2018: coordinate transformation to and from Stelsel van de Rijksdriehoeksmeting and Normaal Amsterdams Peil. `https://www.nsgi.nl/rdnaptrans`, accessed on 2021-06-21.

Leva, D., Nico, G., Tarchi, D., Fortuny-Guasch, J., Sieber, A., 2003. Temporal analysis of a landslide by means of a ground-based SAR interferometer. *IEEE Transactions on Geoscience and Remote Sensing*, 41(4), 745–752. `https://doi.org/10.1109/TGRS.2003.808902`.

Lewis, A., Lymburner, L., Purss, M. B. J., Brooke, B., Evans, B., Ip, A., Dekker, A. G., Irons, J. R., Minchin, S., Mueller, N., Oliver, S., Roberts, D., Ryan, B., Thankappan, M., Woodcock, R., Wyborn, L., 2016. Rapid, high-resolution detection of environmental change over continental scales from satellite data – the Earth Observation Data Cube. *International Journal of Digital Earth*, 9(1), 106–111. `https://doi.org/10.1080/17538947.2015.1111952`.

Li, C., Criss, R. E., Fu, Z., Long, J., Tan, Q., 2021. Evolution characteristics and displacement forecasting model of landslides with stair-step sliding surface along the Xiangxi River, three Gorges Reservoir region, China. *Engineering Geology*, 283, 105961. `https://doi.org/10.1016/j.enggeo.2020.105961`.

Li, H., Xu, Q., He, Y., Deng, J., 2018. Prediction of landslide displacement with an ensemble-based extreme learning machine and copula models. *Landslides*, 15(10), 2047–2059. `https://doi.org/10.1007/s10346-018-1020-2`.

Li, H., Xu, Q., He, Y., Fan, X., Li, S., 2019. Modeling and predicting reservoir landslide displacement with deep belief network and EWMA control charts: a case study in Three Gorges Reservoir. *Landslides*. `https://doi.org/10.1007/s10346-019-01312-6`.

Lian, C., Zeng, Z., Yao, W., Tang, H., 2013. Displacement prediction model of landslide based on a modified ensemble empirical mode decomposition and extreme learning machine. *Natural Hazards*, 66(2), 759–771. `https://doi.org/10.1007/s11069-012-0517-6`.

Lian, C., Zeng, Z., Yao, W., Tang, H., 2015. Multiple neural networks switched prediction for landslide displacement. *Engineering Geology*, 186, 91–99. `https://doi.org/10.1016/j.enggeo.2014.11.014`.

Lins, H. F., 2012. USGS hydro-climatic data network 2009 (HCDN-2009). Fact Sheet 2012-3047, USGS.

Liu, Y., Qiu, H., Yang, D., Liu, Z., Ma, S., Pei, Y., Zhang, J., Tang, B., 2021. Deformation responses of landslides to seasonal rainfall based on InSAR and wavelet analysis. *Landslides*. `https://doi.org/10.1007/s10346-021-01785-4`.

Liu, Z.-q., Guo, D., Lacasse, S., Li, J.-h., Yang, B.-b., Choi, J.-c., 2020. Algorithms for intelligent prediction of landslide displacements. *Journal of Zhejiang University-Science A*, 21(6), 412–429. `https://doi.org/10.1631/jzus.A2000005`.

Liu, Z., Shao, J., Xu, W., Chen, H., Shi, C., 2014. Comparison on landslide nonlinear displacement analysis and prediction with computational intelligence approaches. *Landslides*, 11(5), 889–896. `https://doi.org/10.1007/s10346-013-0443-z`.

Logar, J., Turk, G., Marsden, P., Ambrožič, T., 2017. Prediction of rainfall induced landslide movements by artificial neural networks. *Natural Hazards and Earth System Sciences Discussions*, 1–18. `https://doi.org/10.5194/nhess-2017-253`.

Louis, J., Pflug, B., Main-Knorn, M., Debaecker, V., Mueller-Wilm, U., Iannone, R. Q., Giuseppe Cadau, E., Boccia, V., Gascon, F., 2019. Sentinel-2 global surface reflectance level-2a product generated with Sen2Cor. *IGARSS 2019 - 2019 IEEE International Geoscience and Remote Sensing Symposium*, IEEE, Yokohama, Japan, 8522–8525. `https://doi.org/10.1109/IGARSS.2019.8898540`.

Ma, J., Tang, H., Liu, X., Hu, X., Sun, M., Song, Y., 2017. Establishment of a deformation forecasting model for a step-like landslide based on decision tree C5.0 and two-step cluster algorithms: a case study in the Three Gorges Reservoir area, China. *Landslides*, 14(3), 1275–1281. `https://doi.org/10.1007/s10346-017-0804-0`.

Main-Knorn, M., Pflug, B., Louis, J., Debaecker, V., Müller-Wilm, U., Gascon, F., 2017. Sen2Cor for Sentinel-2. L. Bruzzone, F. Bovolo, J. A. Benediktsson (eds), *Image and Signal Processing for Remote Sensing XXIII*, SPIE, Warsaw, Poland, 3. `https://doi.org/10.1117/12.2278218`.

Makridakis, S., Spiliotis, E., Assimakopoulos, V., 2018. Statistical and machine learning forecasting methods: concerns and ways forward. *PLOS ONE*, 13(3), e0194889. `https://doi.org/10.1371/journal.pone.0194889`.

Malet, J.-P., van Asch, T., van Beek, R., Maquaire, O., 2005. Forecasting the behaviour of complex landslides with a spatially distributed hydrological model. *Natural Hazards and Earth System Sciences*, 5(1), 71–85.

Mansour, M. F., Morgenstern, N. R., Martin, C. D., 2011. Expected damage from displacement of slow-moving slides. *Landslides*, 8(1), 117–131. `https://doi.org/10.1007/s10346-010-0227-7`.

Marino, P., Peres, D. J., Cancelliere, A., Greco, R., Bogaard, T. A., 2020. Soil moisture information can improve shallow landslide forecasting using the hydrometeorological threshold approach. *Landslides*, 17(9), 2041–2054. `https://doi.org/10.1007/s10346-020-01420-8`.

Martens, B., Miralles, D. G., Lievens, H., van der Schalie, R., de Jeu, R. A. M., Fernández-Prieto, D., Beck, H. E., Dorigo, W. A., Verhoest, N. E. C., 2017. GLEAM v3: satellite-based land evaporation and root-zone soil moisture. *Geoscientific Model Development*, 10(5), 1903–1925. `https://doi.org/10.5194/gmd-10-1903-2017`.

Massey, C., Petley, D., McSaveney, M., 2013. Patterns of movement in reactivated landslides. *Engineering Geology*, 159, 1–19. `https://doi.org/10.1016/j.enggeo.2013.03.011`.

Meyer, H., Pebesma, E., 2021. Predicting into unknown space? Estimating the area of applicability of spatial prediction models. *Methods in Ecology and Evolution*, 12(9), 1620–1633. `https://doi.org/10.1111/2041-210X.13650`.

Meyer, H., Reudenbach, C., Hengl, T., Katurji, M., Nauss, T., 2018. Improving performance of spatio-temporal machine learning models using forward feature selection and target-oriented validation. *Environmental Modelling & Software*, 101, 1–9. `https://doi.org/10.1016/j.envsoft.2017.12.001`.

Meyer, H., Reudenbach, C., Wöllauer, S., Nauss, T., 2019. Importance of spatial predictor variable selection in machine learning applications – moving from data reproduction to spatial prediction. *Ecological Modelling*, 411, 108815. `https://doi.org/10.1016/j.ecolmodel.2019.108815`.

Miao, F., Wu, Y., Xie, Y., Li, Y., 2018. Prediction of landslide displacement with step-like behavior based on multialgorithm optimization and a support vector regression model. *Landslides*, 15(3), 475–488. `https://doi.org/10.1007/s10346-017-0883-y`.

Miao, F., Xie, X., Wu, Y., Zhao, F., 2022. Data mining and deep learning for predicting the displacement of “step-like” landslides. *Sensors*, 22(2), 481. `https://doi.org/10.3390/s22020481`.

Microsoft, 2022. Microsoft planetary computer. `https://planetarycomputer.microsoft.com/`, accessed on 2022-11-17.

Miralles, D. G., Holmes, T. R. H., De Jeu, R. A. M., Gash, J. H., Meesters, A. G. C. A., Dolman, A. J., 2011. Global land-surface evaporation estimated from satellite-based observations. *Hydrology and Earth System Sciences*, 15(2), 453–469. `https://doi.org/10.5194/hess-15-453-2011`.

Mirus, B. B., Becker, R. E., Baum, R. L., Smith, J. B., 2018. Integrating real-time subsurface hydrologic monitoring with empirical rainfall thresholds to improve landslide early warning. *Landslides*, 15(10), 1909–1919. `https://doi.org/10.1007/s10346-018-0995-z`.

Mondini, A., Santangelo, M., Rocchetti, M., Rossetto, E., Manconi, A., Monserrat, O., 2019. Sentinel-1 SAR amplitude imagery for rapid landslide detection. *Remote Sensing*, 11(7), 760. `https://doi.org/10.3390/rs11070760`.

Nadim, F., Kjekstad, O., Peduzzi, P., Herold, C., Jaedicke, C., 2006. Global landslide and avalanche hotspots. *Landslides*, 3(2), 159–173. `https://doi.org/10.1007/s10346-006-0036-1`.

NASA, 2015. AppEEARS. `https://appeears.earthdatacloud.nasa.gov/`, accessed on 2022-11-20.

NASA, 2021. EOSDIS Distributed Active Archive Centers (DAAC). `http://www.earthdata.nasa.gov/eosdis/daacs`, accessed on 2022-11-08.

NASA, 2022a. GPM precipitation data directory. `https://gpm.nasa.gov/data/directory`, accessed on 2022-11-08.

NASA, 2022b. NASA Earth data. `https://search.earthdata.nasa.gov/`, accessed on 2022-11-08.

Nascetti, A., Di Rita, M., Ravanelli, R., Amicuzi, M., Esposito, S., Crespi, M., 2017. Free global DSM assessment on large scale areas exploiting the potentialities of the innovative Google Earth Engine platform. *ISPRS - International Archives of the Photogrammetry, Remote Sensing and Spatial Information Sciences*, XLII-1/W1, 627–633. `https://doi.org/10.5194/isprs-archives-XLII-1-W1-627-2017`.

Neaupane, K., Achet, S., 2004. Use of backpropagation neural network for landslide monitoring: a case study in the higher Himalaya. *Engineering Geology*, 74(3-4), 213–226. `https://doi.org/10.1016/j.enggeo.2004.03.010`.

Nesshöver, C., Assmuth, T., Irvine, K. N., Rusch, G. M., Waylen, K. A., Delbaere, B., Haase, D., Jones-Walters, L., Keune, H., Kovacs, E., Krauze, K., Külvik, M., Rey, F., van Dijk, J., Vistad, O. I., Wilkinson, M. E., Wittmer, H., 2017. The science, policy and practice of nature-based solutions: An interdisciplinary perspective. *Science of The Total Environment*, 579, 1215–1227. `https://doi.org/10.1016/j.scitotenv.2016.11.106`.

Nie, W., Krautblatter, M., Leith, K., Thuro, K., Festl, J., 2017. A modified tank model including snowmelt and infiltration time lags for deep-seated landslides in alpine environments (Aggenalm, Germany). *Natural Hazards and Earth System Sciences*, 17(9), 1595–1610. `https://doi.org/10.5194/nhess-17-1595-2017`.

Notti, D., Davalillo, J. C., Herrera, G., Mora, O., 2010. Assessment of the performance of X-band satellite radar data for landslide mapping and monitoring: Upper Tena Valley case study. *Natural Hazards and Earth System Sciences*, 10(9), 1865–1875. `https://doi.org/10.5194/nhess-10-1865-2010`.

Notti, D., Herrera, G., Bianchini, S., Meisina, C., García-Davalillo, J. C., Zucca, F., 2014. A methodology for improving landslide PSI data analysis. *International Journal of Remote Sensing*, 35(6), 2186–2214. `https://doi.org/10.1080/01431161.2014.889864`.

Notti, D., Meisina, C., Zucca, F., Colombo, A., 2011. Models to predict persistent scatterers data distribution and their capacity to register movement along the slope. *Fringe Workshop 2011.*

Novellino, A., Cesarano, M., Cappelletti, P., Di Martire, D., Di Napoli, M., Ramondini, M., Sowter, A., Calcaterra, D., 2021. Slow-moving landslide risk assessment combining machine learning and InSAR techniques. *CATENA*, 203, 105317. `https://doi.org/10.1016/j.catena.2021.105317`.

Novellino, A., Cigna, F., Brahmi, M., Sowter, A., Bateson, L., Marsh, S., 2017. Assessing the feasibility of a national InSAR ground deformation map of Great Britain with Sentinel-1. *Geosciences*, 7(2), 19. `https://doi.org/10.3390/geosciences7020019`.

Novák, V., 2012. Methods of evapotranspiration estimation. V. Novák (ed.), *Evapotranspiration in the Soil-Plant-Atmosphere System*, Springer Netherlands, Dordrecht, 165–215.

OData, 2022. OData: the best way to REST. `https://www.odata.org/`, accessed on 2022-11-08.

OGC, 2014. WFS: Web Feature Service. `https://www.ogc.org/standards/wfs`, accessed on 2022-11-16.

OGC, 2015. WPS: Web Processing Service. `https://www.ogc.org/standards/wps`, accessed on 2022-11-16.

OGC, 2018. WCS: Web Coverage Service. `https://www.ogc.org/standards/wcs`, accessed on 2022-11-16.

OGC, 2022. OGC standards. `https://www.ogc.org/docs/is`, accessed on 2022-11-15.

Open-ended intergovernmental expert working group on indicators and terminology relating to disaster risk reduction, 2016. Report of the open-ended intergovernmental expert working group on indicators and terminology relating to disaster risk reduction. Technical report, United Nations General Assembly.

openEO, 2022. openEO. `https://openeo.org/`, accessed on 2022-11-22.

Parajka, J., Kohnová, S., Merz, R., Szolgay, J., Hlavčová, K., Blöschl, G., 2009. Comparative analysis of the seasonality of hydrological characteristics in Slovakia and Austria. *Hydrological Sciences Journal*, 54(3), 456–473. `https://doi.org/10.1623/hysj.54.3.456`.

Pebesma, E., Wagner, W., Verbesselt, J., Goor, E., Briese, C., Neteler, M., 2016. OpenEO: a GDAL for earth observation analytics. `https://r-spatial.org/2016/11/29/openeo.html`, accessed on 2022-11-30.

Petley, D., Dunning, S., Rosser, N., Hungr, O., 2005. The analysis of global landslide risk through the creation of a database of worldwide landslide fatalities. *Landslide risk management. Balkema, Amsterdam*, 367–374.

Peyret, M., Djamour, Y., Rizza, M., Ritz, J.-F., Hurtrez, J.-E., Goudarzi, M., Nankali, H., Chéry, J., Le Dortz, K., Uri, F., 2008. Monitoring of the large slow Kahrod landslide in Alborz mountain range (Iran) by GPS and SAR interferometry. *Engineering Geology*, 100(3-4), 131–141. `https://doi.org/10.1016/j.enggeo.2008.02.013`.

Pfeiffer, J., Zieher, T., Bremer, M., Wichmann, V., Rutzinger, M., 2018. Derivation of three-dimensional displacement vectors from multi-temporal long-range terrestrial laser scanning at the Reissenschuh landslide (Tyrol, Austria). *Remote Sensing*, 10(11), 1688. `https://doi.org/10.3390/rs10111688`.

Pfeiffer, J., Zieher, T., Rutzinger, M., Bremer, M., Wichmann, V., 2019. Comparison and time series analysis of landslide displacement mapped by airborne, terrestrial and unmanned aerial vehicle based platforms. *ISPRS Annals of the Photogrammetry, Remote Sensing and Spatial Information Sciences*, IV-2/W5, 421–428. `https://doi.org/10.5194/isprs-annals-IV-2-W5-421-2019`.

Pfeiffer, J., Zieher, T., Schmieder, J., Bogaard, T., Rutzinger, M., Spötl, C., 2022. Spatial assessment of probable recharge areas – investigating the hydrogeological controls of an active deep-seated gravitational slope deformation. *Natural Hazards and Earth System Sciences*, 22(7), 2219–2237. `https://doi.org/10.5194/nhess-22-2219-2022`.

Pfeiffer, J., Zieher, T., Schmieder, J., Rutzinger, M., Strasser, U., 2021. Spatio-temporal assessment of the hydrological drivers of an active deep-seated gravitational slope deformation: the Vögelsberg landslide in Tyrol (Austria). *Earth Surface Processes and Landforms*, 1–17. `https://doi.org/10.1002/esp.5129`.

Pinel, V., Poland, M., Hooper, A., 2014. Volcanology: lessons learned from synthetic aperture radar imagery. *Journal of Volcanology and Geothermal Research*, 289, 81–113. `https://doi.org/10.1016/j.jvolgeores.2014.10.010`.

Plank, S., Singer, J., Minet, C., Thuro, K., 2012. Pre-survey suitability evaluation of the differential synthetic aperture radar interferometry method for landslide monitoring. *International Journal of Remote Sensing*, 33(20), 6623–6637. `https://doi.org/10.1080/01431161.2012.693646`.

Plank, S., Singer, J., Thuro, K., Minet, C., 2010. The suitability of the differential radar interferometry method for deformation monitoring of landslides—a new GIS based evaluation tool. *Geologically Active*, Taylor & Francis Group, Auckland, New Zealand, 2345–2352.

Ponziani, F., Pandolfo, C., Stelluti, M., Berni, N., Brocca, L., Moramarco, T., 2012. Assessment of rainfall thresholds and soil moisture modeling for operational hydrogeological risk prevention in the Umbria region (central Italy). *Landslides*, 9(2), 229–237. `https://doi.org/10.1007/s10346-011-0287-3`.

Posner, A., Georgakakos, K., 2016. An early warning system for landslide danger. *Eos*. `https://doi.org/10.1029/2016EO062323`.

Potin, P., Colin, O., Pinheiro, M., Rosich, B., O'Connell, A., Ormston, T., Gratadour, J.-B., Torres, R., 2022. Status and evolution of the Sentinel-1 mission. *IGARSS 2022 - 2022 IEEE International Geoscience and Remote Sensing Symposium*, IEEE, Kuala Lumpur, Malaysia, 4707–4710. `https://doi.org/10.1109/IGARSS46834.2022.9884753`.

Prokop, A., Panholzer, H., 2009. Assessing the capability of terrestrial laser scanning for monitoring slow moving landslides. *Natural Hazards and Earth System Sciences*, 9(6), 1921–1928. `https://doi.org/10.5194/nhess-9-1921-2009`.

Punsvik, B., 2022. Sensor data from space, on ground - now. `https://www.eoport.com/wp-content/uploads/2022/07/LPS2022-EOPORT-demonstration-small.pdf`, accessed on 2022-10-04.

Radbruch, D. H., Crowther, K. C., 1970. Map showing relative amounts of landslides in California. Open-File Report 70-270, US Geological Survey.

Rasdaman, 2022. Rasdaman: raster data manager. `http://www.rasdaman.org/wiki`, accessed on 2022-11-17.

Raspini, F., Bianchini, S., Ciampalini, A., Del Soldato, M., Solari, L., Novali, F., Del Conte, S., Rucci, A., Ferretti, A., Casagli, N., 2018. Continuous, semi-automatic monitoring of ground deformation using Sentinel-1 satellites. *Scientific Reports*, 8(1). `https://doi.org/10.1038/s41598-018-25369-w`.

Reichenbach, P., Rossi, M., Malamud, B. D., Mihir, M., Guzzetti, F., 2018. A review of statistically-based landslide susceptibility models. *Earth-Science Reviews*, 180, 60–91. `https://doi.org/10.1016/j.earscirev.2018.03.001`.

Reichle, R., De Lannoy, G., Koster, R., Crow, W., Kimball, J., Liu, Q., 2022. SMAP L4 global 3-hourly 9 km EASE-grid surface and root zone soil moisture. Geophysical data, version 6. `https://nsidc.org/data/spl4smgp/versions/6`, accessed on 2022-01-31. Type: dataset.

Ren, F., Wu, X., Zhang, K., Niu, R., 2015. Application of wavelet analysis and a particle swarm-optimized support vector machine to predict the displacement of the Shuping landslide in the Three Gorges, China. *Environmental Earth Sciences*, 73(8), 4791–4804. `https://doi.org/10.1007/s12665-014-3764-x`.

Riedmann, M., Bindrich, M., Damen, M. C., Van Westen, C. J., Micu, M., 2014. Generating a landslide inventory map using stero photo interpretation and radar interferometry techniques - a case study from the Buzău Mountains area, Romenia. *Proceedings of the International Conference on Analysis and Management of Changing Risks for Natural Hazards*, Padua, Italy, 571–577.

Righini, G., Pancioli, V., Casagli, N., 2012. Updating landslide inventory maps using Persistent Scatterer Interferometry (PSI). *International Journal of Remote Sensing*, 33(7), 2068–2096. `https://doi.org/10.1080/01431161.2011.605087`.

Rizzoli, P., Martone, M., Gonzalez, C., Wecklich, C., Borla Tridon, D., Bräutigam, B., Bachmann, M., Schulze, D., Fritz, T., Huber, M., Wessel, B., Krieger, G., Zink, M., Moreira, A., 2017. Generation and performance assessment of the global TanDEM-X digital elevation model. *ISPRS Journal of Photogrammetry and Remote Sensing*, 132, 119–139. `https://doi.org/10.1016/j.isprsjprs.2017.08.008`.

Robinson, N., Regetz, J., Guralnick, R. P., 2014. EarthEnv-DEM90: A nearly-global, void-free, multi-scale smoothed, 90m digital elevation model from fused ASTER and SRTM data. *ISPRS Journal of Photogrammetry and Remote Sensing*, 87, 57–67. `https://doi.org/10.1016/j.isprsjprs.2013.11.002`.

Rodríguez, C., Bommer, J., Chandler, R., 1999. Earthquake-induced landslides: 1980–1997. *Soil Dynamics and Earthquake Engineering*, 18(5), 325–346. `https://doi.org/https://doi.org/10.1016/S0267-7261(99)00012-3`.

Rosi, A., Tofani, V., Tanteri, L., Tacconi Stefanelli, C., Agostini, A., Catani, F., Casagli, N., 2018. The new landslide inventory of Tuscany (Italy) updated with PS-InSAR: geomorphological features and landslide distribution. *Landslides*, 15(1), 5–19. `https://doi.org/10.1007/s10346-017-0861-4`.

Roulette, J., 2022. Russia's anti-satellite threat tests laws of war in space. *Reuters*.

RVO, PDOK, 2022. BRP: Basisregistratie Gewaspercelen. `https://www.pdok.nl/introductie/-/article/basisregistratie-gewaspercelen-brp-`, accessed on 2022-11-16.

Sanchez, P. A., Ahamed, S., Carré, F., Hartemink, A. E., Hempel, J., Huising, J., Lagacherie, P., McBratney, A. B., McKenzie, N. J., Mendonça-Santos, M. d. L., Minasny, B., Montanarella, L., Okoth, P., Palm, C. A., Sachs, J. D., Shepherd, K. D., Vågen, T.-G., Vanlauwe, B., Walsh, M. G., Winowiecki, L. A., Zhang, G.-L., 2009. Digital soil map of the world. *Science*, 325(5941), 680–681. `https://doi.org/10.1126/science.1175084`.

Sassa, K., 2019. The Kyoto landslide commitment 2020: first signatories. *Landslides*, 16(11), 2053–2057. `https://doi.org/10.1007/s10346-019-01295-4`.

Satgé, F., Defrance, D., Sultan, B., Bonnet, M.-P., Seyler, F., Rouché, N., Pierron, F., Paturel, J.-E., 2020. Evaluation of 23 gridded precipitation datasets across West Africa. *Journal of Hydrology*, 581, 124412. `https://doi.org/10.1016/j.jhydrol.2019.124412`.

Schindler, F., Meißl, S., 2021. geotiff.js. `https://geotiffjs.github.io/`, accessed on 2022-10-31.

Schlögel, R., Doubre, C., Malet, J.-P., Masson, F., 2015. Landslide deformation monitoring with ALOS/PALSAR imagery: a D-InSAR geomorphological interpretation method. *Geomorphology*, 231, 314–330. `https://doi.org/10.1016/j.geomorph.2014.11.031`.

Schlögel, R., Thiebes, B., Toschi, I., Zieher, T., Darvishi, M., Kofler, C., 2017. Sensor data integration for landslide monitoring—The LEMONADE concept. *Workshop on World Landslide Forum*, 71–78.

Scholes, R., Brown de Colstoun, E., Hall, F., Collatz, G., Meeson, B., Los, S., Landis, D., 2011. ISLSCP II Global Gridded Soil Characteristics. `https://doi.org/10.3334/ORNLDAAC/1004`.

Schubert, A., Small, D., 2016. Sentinel-1A radiometric consistency between TOPS SLC and GRD products. Technical Report UZH-S1-TOPS-RADIOMETRY-TN05, University of Zurich.

Segalini, A., Carri, A., Valletta, A., Martino, M., 2019. Innovative monitoring tools and early warning systems for risk management: a case study. *Geosciences*, 9(2), 62. `https://doi.org/10.3390/geosciences9020062`.

Shimada, M., Itoh, T., Motooka, T., Watanabe, M., Shiraishi, T., Thapa, R., Lucas, R., 2014. New global forest/non-forest maps from ALOS PALSAR data (2007–2010). *Remote Sensing of Environment*, 155, 13–31. `https://doi.org/10.1016/j.rse.2014.04.014`.

Shirzadi, A., Solaimani, K., Roshan, M. H., Kavian, A., Chapi, K., Shahabi, H., Keesstra, S., Ahmad, B. B., Bui, D. T., 2019. Uncertainties of prediction accuracy in shallow landslide modeling: Sample size and raster resolution. *CATENA*, 178, 172–188. `https://doi.org/10.1016/j.catena.2019.03.017`.

Singleton, A., Li, Z., Hoey, T., Muller, J.-P., 2014. Evaluating sub-pixel offset techniques as an alternative to D-InSAR for monitoring episodic landslide movements in vegetated terrain. *Remote Sensing of Environment*, 147, 133–144. `https://doi.org/10.1016/j.rse.2014.03.003`.

STAC, 2022. STAC: SpatioTemporal Asset Catalogs. `https://stacspec.org/en/`, accessed on 2022-11-23.

Stanley, T. A., Kirschbaum, D. B., Benz, G., Emberson, R. A., Amatya, P. M., Medwedeff, W., Clark, M. K., 2021. Data-driven landslide nowcasting at the global scale. *Frontiers in Earth Science*, 9, 378. `https://doi.org/10.3389/feart.2021.640043`.

Stanley, T., Kirschbaum, D. B., 2017. A heuristic approach to global landslide susceptibility mapping. *Natural Hazards*, 87(1), 145–164. `https://doi.org/10.1007/s11069-017-2757-y`.

Stumpf, A., Malet, J.-P., Delacourt, C., 2017. Correlation of satellite image time-series for the detection and monitoring of slow-moving landslides. *Remote Sensing of Environment*, 189, 40–55. `https://doi.org/10.1016/j.rse.2016.11.007`.

Sudmanns, M., Tiede, D., Lang, S., Bergstedt, H., Trost, G., Augustin, H., Baraldi, A., Blaschke, T., 2019. Big Earth data: disruptive changes in Earth observation data management and analysis? *International Journal of Digital Earth*, 1–19. `https://doi.org/10.1080/17538947.2019.1585976`.

Sun, Q., Zhang, L., Ding, X., Hu, J., Li, Z., Zhu, J., 2015. Slope deformation prior to Zhouqu, China landslide from InSAR time series analysis. *Remote Sensing of Environment*, 156, 45–57. `https://doi.org/10.1016/j.rse.2014.09.029`.

Sundermeyer, M., Schülter, R., Ney, H., 2012. LSTM neural networks for language modeling. *Interspeech 2012*, ISCA, Portland, Oregon, USA, 4.

Suwandana, E., Kawamura, K., Sakuno, Y., Kustiyanto, E., Raharjo, B., 2012. Evaluation of ASTER GDEM2 in comparison with GDEM1, SRTM DEM and topographic-map-derived DEM using inundation area analysis and RTK-dGPS data. *Remote Sensing*, 4(8), 2419–2431. `https://doi.org/10.3390/rs4082419`.

Szabó, G., Singh, S. K., Szabó, S., 2015. Slope angle and aspect as influencing factors on the accuracy of the SRTM and the ASTER GDEM databases. *Physics and Chemistry of the Earth, Parts A/B/C*, 83-84, 137–145. `https://doi.org/10.1016/j.pce.2015.06.003`.

Tachikawa, T., Kaku, M., Iwasaki, A., Gesch, D. B., Oimoen, M. J., Zhang, Z., Danielson, J. J., Krieger, T., Curtis, B., Haase, J., others, 2011. ASTER global digital elevation model version 2 – summary of validation results. Technical report, NASA.

Tadono, T., Ishida, H., Oda, F., Naito, S., Minakawa, K., Iwamoto, H., 2014. Precise global DEM generation by ALOS PRISM. *ISPRS Annals of Photogrammetry, Remote Sensing and Spatial Information Sciences*, II-4, 71–76. `https://doi.org/10.5194/isprsannals-II-4-71-2014`.

TensorFlow Developers, 2022. TensorFlow. `https://zenodo.org/record/4724125`, accessed on 2022-02-28.

Terzaghi, K., 1943. *Theoretical soil mechanics.* John Wiley & Sons, Inc., Hoboken, NJ, USA.

Teunissen, P. J. G., 2006. *Testing theory: an introduction.* Series on Mathematical Geodesy and Positioning, 2nd edn, Delft University Press, Delft.

Thiel, M., Otte, I., Hill, S.,Förtsch, S., Sebold, S., Löw, J., 2022. eo2cube: Earth observation data cubes of the University of Würzburg. `https://datacube.remote-sensing.org/`, accessed on 2022-11-15.

Thomas, M. A., Collins, B. D., Mirus, B. B., 2019. Assessing the feasibility of satellite-based thresholds for hydrologically driven landsliding. *Water Resources Research*. `https://doi.org/10.1029/2019WR025577`.

Thompson, J. A., Bell, J. C., Butler, C. A., 2001. Digital elevation model resolution: effects on terrain attribute calculation and quantitative soil-landscape modeling. *Geoderma*, 100(1-2), 67–89. `https://doi.org/10.1016/S0016-7061(00)00081-1`.

Tofani, V., Raspini, F., Catani, F., Casagli, N., 2013a. Persistent Scatterer Interferometry (PSI) technique for landslide characterization and monitoring. *Remote Sensing*, 5(3), 1045–1065. `https://doi.org/10.3390/rs5031045`.

Tofani, V., Segoni, S., Agostini, A., Catani, F., Casagli, N., 2013b. Technical Note: use of remote sensing for landslide studies in Europe. *Natural Hazards and Earth System Sciences*, 13(2), 299–309. `https://doi.org/https://doi.org/10.5194/nhess-13-299-2013`.

Tuomenvirta, H., Mäkelä, A., Spyrou, C., Apostolidou, E., Panga, D., Gonzalez-Ollauri, A., Corvaglia, P., 2019. Data requirements to assess and monitor OAL performance. Technical Report OPERANDUM D4.1, Finnish Meteorological Institute.

USGS, 2015. LP DAAC data access through OPeNDAP and web services. `https://lpdaac.usgs.gov/resources/e-learning/lp-daac-data-access-through-opendap-and-web-services/`, accessed on 2022-11-17.

USGS, 2022a. EarthExplorer. `https://earthexplorer.usgs.gov/`, accessed on 2022-11-11.

USGS, 2022b. Landsat commercial cloud data access. `https://www.usgs.gov/landsat-missions/landsat-commercial-cloud-data-access`, accessed on 2022-11-09.

van Asch, T., Buma, J., van Beek, L., 1999. A view on some hydrological triggering systems in landslides. *Geomorphology*, 30(1-2), 25–32. `https://doi.org/10.1016/S0169-555X(99)00042-2`.

van Asch, T., van Beek, L., Bogaard, T., 2007. Problems in predicting the mobility of slow-moving landslides. *Engineering Geology*, 91(1), 46–55. `https://doi.org/10.1016/j.enggeo.2006.12.012`.

van Leijen, F. J., 2014. Persistent scatterer interferometry based on geodetic estimation theory. PhD thesis, Delft University of Technology. ISBN: 9789461862990 OCLC: 905870982.

van Natijne, A., 2019. Sentinel-2 data cube. `https://weblog.fwrite.org/datacube/`, accessed on 2022-11-23.

van Natijne, A., 2020. GeoTiles.nl: readymade geodata with a focus on the Netherlands. `https://geotiles.nl/`, accessed on 2022-11-28.

van Natijne, A., Bogaard, T., van Leijen, F., Hanssen, R., Lindenbergh, R., 2022a. World-wide InSAR sensitivity index for landslide deformation tracking. *International Journal of Applied Earth Observation and Geoinformation*, 111, 102829. `https://doi.org/10.1016/j.jag.2022.102829`.

van Natijne, A. L., Bogaard, T. A., van Leijen, F. J., Hanssen, R. F., Lindenbergh, R. C., 2022b. World-wide InSAR sensitivity index data set for landslide deformation tracking. `https://doi.org/10.4121/14095777`. Data set.

van Natijne, A. L., Bogaard, T. A., Zieher, T., Pfeiffer, J., Lindenbergh, R. C., 2022c. Machine learning nowcasting of the Vögelsberg deep-seated landslide: why predicting slow deformation is not so easy. `https://egusphere.copernicus.org/preprints/2022/egusphere-2022-950/`, accessed on 2022-10-04.

van Natijne, A. L., Lindenbergh, R. C., Bogaard, T. A., 2020. Machine Learning: new potential for local and regional deep-seated landslide nowcasting. *Sensors*, 20(5), 1425. `https://doi.org/10.3390/s20051425`.

van Rossum, G., Python contributors, 2008. Python programming language. `https://www.python.org`. Software package.

van Westen, C. J., Castellanos, E., Kuriakose, S. L., 2008. Spatial data for landslide susceptibility, hazard, and vulnerability assessment: An overview. *Engineering Geology*, 102(3-4), 112–131. `https://doi.org/10.1016/j.enggeo.2008.03.010`.

Villamil Lopez, C., Stilla, U., 2021. Monitoring of oil tank filling with spaceborne SAR using coherent scatterers. *IEEE Journal of Selected Topics in Applied Earth Observations and Remote Sensing*, 14, 5638–5655. `https://doi.org/10.1109/JSTARS.2021.3082181`.

Wagner, W., Bauer-Marschallinger, B., Navacchi, C., Reuß, F., Cao, S., Reimer, C., Schramm, M., Briese, C., 2021. A Sentinel-1 backscatter datacube for global land monitoring applications. *Remote Sensing*, 13(22), 4622. `https://doi.org/10.3390/rs13224622`.

Wang, Y., Tang, H., Wen, T., Ma, J., Zou, Z., Xiong, C., 2019. Point and interval predictions for Tanjiahe landslide displacement in the Three Gorges reservoir area, China. *Geofluids*, 2019, 1–14. `https://doi.org/10.1155/2019/8985325`.

Wei, Z.-l., Lü, Q., Sun, H.-y., Shang, Y.-q., 2019. Estimating the rainfall threshold of a deep-seated landslide by integrating models for predicting the groundwater level and stability analysis of the slope. *Engineering Geology*, 253, 14–26. `https://doi.org/10.1016/j.enggeo.2019.02.026`.

Wen, T., Tang, H., Wang, Y., Lin, C., Xiong, C., 2017. Landslide displacement prediction using the GA-LSSVM model and time series analysis: a case study of Three Gorges Reservoir, China. *Natural Hazards and Earth System Sciences*, 17(12), 2181–2198. `https://doi.org/10.5194/nhess-17-2181-2017`.

Wilde, M., Günther, A., Reichenbach, P., Malet, J.-P., Hervás, J., 2018. Pan-European landslide susceptibility mapping: ELSUS version 2. *Journal of Maps*, 14(2), 97–104. `https://doi.org/10.1080/17445647.2018.1432511`.

Wilkinson, M. D., Dumontier, M., Aalbersberg, I. J., Appleton, G., Axton, M., Baak, A., Blomberg, N., Boiten, J.-W., da Silva Santos, L. B., Bourne, P. E., Bouwman, J., Brookes, A. J., Clark, T., Crosas, M., Dillo, I., Dumon, O., Edmunds, S., Evelo, C. T., Finkers, R., Gonzalez-Beltran, A., Gray, A. J., Groth, P., Goble, C., Grethe, J. S., Heringa, J., 't Hoen, P. A., Hooft, R., Kuhn, T., Kok, R., Kok, J., Lusher, S. J., Martone, M. E., Mons, A., Packer, A. L., Persson, B., Rocca-Serra, P., Roos, M., van Schaik, R., Sansone, S.-A., Schultes, E., Sengstag, T., Slater, T., Strawn, G., Swertz, M. A., Thompson, M., van der Lei, J., van Mulligen, E., Velterop, J., Waagmeester, A., Wittenburg, P., Wolstencroft, K., Zhao, J., Mons, B., 2016. The FAIR guiding principles for scientific data management and stewardship. *Scientific Data*, 3(1), 160018. `https://doi.org/10.1038/sdata.2016.18`.

World Meteorological Organization (WMO), 2021. WMO atlas of mortality and economic losses from weather, climate and water extremes (1970–2019) (WMO-no. 1267). Technical Report 1267, WMO, Geneva.

Wulder, M. A., White, J. C., Loveland, T. R., Woodcock, C. E., Belward, A. S., Cohen, W. B., Fosnight, E. A., Shaw, J., Masek, J. G., Roy, D. P., 2016. The global Landsat archive: status, consolidation, and direction. *Remote Sensing of Environment*, 185, 271–283. `https://doi.org/10.1016/j.rse.2015.11.032`.

Xie, P., Zhou, A., Chai, B., 2019. The application of Long Short-Term Memory (LSTM) method on displacement prediction of multifactor-induced landslides. *IEEE Access*, 7, 54305–54311. `https://doi.org/10.1109/ACCESS.2019.2912419`.

Yamazaki, D., Ikeshima, D., Tawatari, R., Yamaguchi, T., O'Loughlin, F., Neal, J. C., Sampson, C. C., Kanae, S., Bates, P. D., 2017. A high-accuracy map of global terrain elevations: accurate global terrain elevation map. *Geophysical Research Letters*, 44(11), 5844–5853. `https://doi.org/10.1002/2017GL072874`.

Yang, B., Yin, K., Lacasse, S., Liu, Z., 2019. Time series analysis and long short-term memory neural network to predict landslide displacement. *Landslides*. `https://doi.org/10.1007/s10346-018-01127-x`.

Yin, Y., Zheng, W., Liu, Y., Zhang, J., Li, X., 2010. Integration of GPS with InSAR to monitoring of the Jiaju landslide in Sichuan, China. *Landslides*, 7(3), 359–365. `https://doi.org/10.1007/s10346-010-0225-9`.

Zhang, W., Xiao, R., Shi, B., Zhu, H.-h., Sun, Y.-j., 2019. Forecasting slope deformation field using correlated grey model updated with time correction factor and background value optimization. *Engineering Geology*, 260, 105215. `https://doi.org/10.1016/j.enggeo.2019.105215`.

Zhang, X., Zhu, C., He, M., Dong, M., Zhang, G., Zhang, F., 2021. Failure mechanism and long short-term memory neural network model for landslide risk prediction. *Remote Sensing*, 14(1), 166. `https://doi.org/10.3390/rs14010166`.

Zhou, C., Yin, K., Cao, Y., Ahmed, B., 2016. Application of time series analysis and PSO–SVM model in predicting the Bazimen landslide in the Three Gorges Reservoir, China. *Engineering Geology*, 204, 108–120. `https://doi.org/10.1016/j.enggeo.2016.02.009`.

Zhou, Q., Liu, X., 2004. Analysis of errors of derived slope and aspect related to DEM data properties. *Computers & Geosciences*, 30(4), 369–378. `https://doi.org/10.1016/j.cageo.2003.07.005`.

Zhou, X., Li, Z., Li, C., Xing, C., 2019. The research of unstable slope monitoring in complex working environment using GB-SAR. *IOP Conference Series: Earth and Environmental Science*, 227, 062033. `https://doi.org/10.1088/1755-1315/227/6/062033`.

Zhu, X., Xu, Q., Tang, M., Nie, W., Ma, S., Xu, Z., 2017. Comparison of two optimized machine learning models for predicting displacement of rainfall-induced landslide: A case study in Sichuan Province, China. *Engineering Geology*, 218, 213–222. `https://doi.org/10.1016/j.enggeo.2017.01.022`.

Zhu, Z., Wulder, M. A., Roy, D. P., Woodcock, C. E., Hansen, M. C., Radeloff, V. C., Healey, S. P., Schaaf, C., Hostert, P., Strobl, P., Pekel, J.-F., Lymburner, L., Pahlevan, N., Scambos, T. A., 2019. Benefits of the free and open Landsat data policy. *Remote Sensing of Environment*, 224, 382–385. `https://doi.org/10.1016/j.rse.2019.02.016`.

Zieher, T., Bremer, M., Rutzinger, M., Pfeiffer, J., Fritzmann, P., Wichmann, V., 2019. Assessment of landslide-induced displacement and deformation of above-ground objects using UAV-borne and airborne laser scanning data. *ISPRS Annals of Photogrammetry, Remote Sensing and Spatial Information Sciences*, IV-2/W5, 461–467. `https://doi.org/10.5194/isprs-annals-IV-2-W5-461-2019`.

Zieher, T., Pfeiffer, J., van Natijne, A., Lindenbergh, R., 2021. Integrated monitoring of a slowly moving landslide based on total station measurements, multi-temporal terrestrial laser scanning and space-borne interferometric synthetic aperture radar. *2021 IEEE International Geoscience and Remote Sensing Symposium IGARSS*, IEEE, Brussels, Belgium, 942–945. `https://doi.org/10.1109/IGARSS47720.2021.9553324`. ISSN: 2153-7003.

About the author

TU Delft/Frank Auperlé

Adriaan van Natijne (Rotterdam, 1991) studied at the Delft University of Technology. He received his Bachelor of Science in 2015, and graduated cum laude as Master of Science in the Applied Earth Sciences, track Geoscience & Remote Sensing, in 2018. From 2013 to 2018 he was active as assistant in both bachelors and masters level courses on geostatistics and laser scanning. In 2018 he started his PhD project at the department of Geoscience & Remote Sensing of the Delft University of Technology.

Covid pandemic permitting, he presented his work at various national and international conferences, including EGU, ESA Living Planet Symposiums, and the 5th World Landslide Forum.

He has an interest in the optimization of processing of topographic and satellite data. On GeoTiles.nl[1] he publishes readymade geodata with a focus on the Netherlands for a broader audience. Moreover, he maintains a 10+ year archive of public transport departure times[2] for statistical analysis and the development of big data processing methods. He considers cycling as a method of getting somewhere.

---

[1] `https://geotiles.nl`

[2] `https://trein.fwrite.org`

List of publications

Selected publications, relevant to this thesis:

- van Natijne, A. L., Bogaard, T. A., Zieher, T., Pfeiffer, J., Lindenbergh, R. C., 2022c. Machine learning nowcasting of the Vögelsberg deep-seated landslide: why predicting slow deformation is not so easy. `https://egusphere.copernicus.org/preprints/2022/egusphere-2022-950/`, accessed on 2022-10-04 *(Chapter 4)*

- van Natijne, A., Bogaard, T., van Leijen, F., Hanssen, R., Lindenbergh, R., 2022a. World-wide InSAR sensitivity index for landslide deformation tracking. *International Journal of Applied Earth Observation and Geoinformation*, 111, 102829. `https://doi.org/10.1016/j.jag.2022.102829` *(Chapter 3)*
  - van Natijne, A. L., Bogaard, T. A., van Leijen, F. J., Hanssen, R. F., Lindenbergh, R. C., 2022b. World-wide InSAR sensitivity index data set for landslide deformation tracking. `https://doi.org/10.4121/14095777`. Data set

- Zieher, T., Pfeiffer, J., van Natijne, A., Lindenbergh, R., 2021. Integrated monitoring of a slowly moving landslide based on total station measurements, multi-temporal terrestrial laser scanning and space-borne interferometric synthetic aperture radar. *2021 IEEE International Geoscience and Remote Sensing Symposium IGARSS*, IEEE, Brussels, Belgium, 942–945. `https://doi.org/10.1109/IGARSS47720.2021.9553324`. ISSN: 2153-7003

- Alfieri, S. M., Foroughnia, F., Van Natijne, A., Mousivand, A., Lindenbergh, R., Porcu, F., Zieher, T., Pulvirulenti, B., Yang, J., Menenti, M., 2021. Documenting Impacts of Hydro-Meteorological Events Using Earth Observation. *2021 IEEE International Geoscience and Remote Sensing Symposium IGARSS*, IEEE, Brussels, Belgium, 934–937. `https://doi.org/10.1109/IGARSS47720.2021.9554905`

- van Natijne, A. L., Lindenbergh, R. C., Bogaard, T. A., 2020. Machine Learning: new potential for local and regional deep-seated landslide nowcasting. *Sensors*, 20(5), 1425. `https://doi.org/10.3390/s20051425` *(Chapter 2)*

This research was featured in popular science magazine KIJK in May 2022 as “Onderwater ondervraagt: verschuivingen voorzien”[3], and as TU Delft Story of Science “the landslide forecast coming to you from space”[4] in December 2021.

---

[3] `https://www.kijkmagazine.nl/tech/onderwater-ondervraagt-adriaan-van-natijne/`

[4] `https://www.tudelft.nl/en/ceg/research/stories-of-science/the-landslide-forecast-coming-to-you-from-space`